Quantum localisation and multifractality in chains with strongly correlated disorder

Alexander James Duthie

Christ Church
University of Oxford

A thesis submitted for the degree of
Doctor of Philosophy

Hilary 2022

Abstract

Systems with strongly-correlated disorder exhibit rich localisation phenomena in one dimension. These include mobility edges, eigenstate multifractality and mixed phases of localised and extended states. In this thesis, two classes of correlated systems are studied: quasiperiodic models, for which the potential is deterministic and infinite-range correlated, and maximally-correlated random chains.

A framework for localisation in quasiperiodic chains is developed, based on the convergence of local propagators. Using the fact that the associated self energy is an order parameter for localisation, we analyse its convergence in continued fraction (CF) form and thereby infer localisation or its absence, yielding the mobility edges of arbitrary models. Approximate theories can be implemented at any order in the CF by self-consistently determining the self energy. The fate of these theories as their order is taken to infinity is shown to be controlled by the convergence of the underlying CF. In the limit of infinite order, both methods generate exact results. The first-order theory is particularly useful, as it can be implemented analytically, and captures the key properties of the localised and delocalised phases. Results are in excellent agreement with the exact results of three diverse models.

Maximally correlated random chains are then studied, for which any two sites separated by a finite distance necessarily have the same energy in the thermodynamic limit. These systems are shown to host robust eigenstate multifractality at strong disorder, in contrast to uncorrelated models. Furthermore, these eigenstates exhibit an anomalous 'tabletop' structure, imprints of which are seen in the system's dynamical properties. For small disorder, delocalised states are present, and separating these two phases is a mixed region. For a given energy, some disorder realisations in the mixed region host extended states and some multifractal; the disorder-averaged spectrum therefore consists of a mixture of the two with no energy resolution between them. Numerical analysis is used to distinguish the three phases, and their phenomenology is connected to the underlying correlations by means of statistical analysis.

Quantum localisation and multifractality in chains with strongly correlated disorder



Alexander James Duthie

Christ Church

University of Oxford

A thesis submitted for the degree of

Doctor of Philosophy

Hilary 2022

Acknowledgements

First and foremost, I would like to thank my supervisor, Prof. David Logan, for his guidance and support over the last four years. It has been a pleasure to work with and learn from him, and our many discussions have been a highlight of my time at Oxford.

I also owe my sincere thanks to Dr Shitadhi Roy for his excellent supervision and collaboration. I am particularly grateful for his support during my postdoc applications.

I am very grateful to the other group members, Stash and Izzy. My thanks also go to Dr Rob Penfold for the opportunity to teach, and to Dr Michael O'Neill for helping me to become a better teacher.

My time as a DPhil student would not have been nearly as enjoyable without all the friends I have made. In particular, I am grateful to Tom, Harry, Tristan, Mike, and Ava, as well as Tim, Alida, Bea, Louie, Holly, and Dan.

Finally, thank you to my family, and to Lea.

Abstract

Systems with strongly-correlated disorder exhibit rich localisation phenomena in one dimension. These include mobility edges, eigenstate multifractality and mixed phases of localised and extended states. In this thesis, two classes of correlated systems are studied: quasiperiodic models, for which the potential is deterministic and infinite-range correlated, and maximally-correlated random chains.

A framework for localisation in quasiperiodic chains is developed, based on the convergence of local propagators. Using the fact that the associated self energy is an order parameter for localisation, we analyse its convergence in continued fraction (CF) form and thereby infer localisation or its absence, yielding the mobility edges of arbitrary models. Approximate theories can be implemented at any order in the CF by self-consistently determining the self energy. The fate of these theories as their order is taken to infinity is shown to be controlled by the convergence of the underlying CF. In the limit of infinite order, both methods generate exact results. The first-order theory is particularly useful, as it can be implemented analytically, and captures the key properties of the localised and delocalised phases. Results are in excellent agreement with the exact results of three diverse models.

Maximally correlated random chains are then studied, for which any two sites separated by a finite distance necessarily have the same energy in the thermodynamic limit. These systems are shown to host robust eigenstate multifractality at strong disorder, in contrast to uncorrelated models. Furthermore, these eigenstates exhibit an anomalous 'tabletop' structure, imprints of which are seen in the system's dynamical properties. For small disorder, delocalised states are present, and separating these two phases is a mixed region. For a given energy, some disorder realisations in the mixed region host extended states and some multifractal; the disorder-averaged spectrum therefore consists of a mixture of the two with no energy resolution between them. Numerical analysis is used to distinguish the three phases, and their phenomenology is connected to the underlying correlations by means of statistical analysis.

List of Publications

Chapter 4

Reference [1]: A. Duthie, S. Roy, and D. E. Logan,"Self-consistent theory of mobility edges in quasiperiodic chains", Phys. Rev. B **103**, L060201 (2021)

Chapter 5

Reference [2]: A. Duthie, S. Roy, and D. E. Logan, "Localization in quasiperiodic chains: a theory based on convergence of local propagators", Phys. Rev. B **104**, 064201 (2021).

Chapter 6

Reference [3]: A. Duthie, S. Roy, and D. E. Logan, "Anomalous multifractality in quantum chains with strongly correlated disorder", Phys. Rev. B **106**, L020201 (2022).

Contents

1 Introduction **1**

1.1 Anderson localisation . . . 2
1.2 Localisation without disorder: Quasiperiodic models . . . 6
1.3 Many-body localisation . . . 7
1.4 Correlated Anderson problems . . . 9
1.5 Overview . . . 11

2 Background theory **17**

2.1 Local propagators . . . 18
2.1.1 Propagators in the time domain . . . 18
2.1.2 Propagators in the energy domain . . . 20
2.1.3 The operator Dyson equation . . . 21
2.1.4 Introducing the self energy . . . 22
2.1.5 Renormalised perturbation expansion . . . 23
2.1.6 Bethe lattices . . . 27
2.2 The self energy . . . 30
2.2.1 The behaviour of Δ in localised and delocalised phases . . . 30
2.2.2 Two order parameters and their distributions . . . 33
2.2.3 Δ_{typ} and y_{typ} . . . 34
2.2.4 Relating y to the localisation length of states . . . 34
2.2.5 The end-site self energy and approximate theories . . . 35

3 Quasiperiodic models **37**

3.1 The beginning: the Aubry-André-Harper model . . . 38
3.2 Post-Aubry-André-Harper models . . . 40
3.3 Summary of models and localisation phase diagrams . . . 42
3.3.1 The Aubry-André-Harper model . . . 43
3.3.2 The β model . . . 43
3.3.3 The mosaic models . . . 44
3.3.4 Computation of spectra . . . 45

4 Leading-order self-consistent theory **47**
4.1 Introduction . . . 48
4.2 The self energy . . . 49
4.2.1 Numerical computation . . . 51
4.3 First-order self-consistent theory . . . 52
4.3.1 Localised phase . . . 53
4.3.2 Delocalised phase . . . 54
4.3.3 Mobility edge condition . . . 54
4.3.4 Distributions of Δ and y . . . 55
4.3.5 Band edges and density of states . . . 56
4.4 First-order phase diagrams . . . 58
4.4.1 Aubry-André-Harper model . . . 58
4.4.2 β model . . . 60
4.4.3 Mosaic model . . . 63
4.4.4 Numerical solutions to mean-field equations . . . 66
4.4.5 Comparison to exact results . . . 66
4.5 Distributions at first-order . . . 68
4.5.1 Aubry-André-Harper model . . . 69
4.5.2 β and Mosaic models . . . 72
4.5.3 Comparison to numerical results . . . 73
4.6 Conclusion . . . 76

5 Higher-order theories and the continued fraction **78**
5.1 Introduction . . . 79
5.2 The continued fraction . . . 80
5.2.1 Localised phase . . . 82
5.3 Convergence of the continued fraction . . . 83
5.4 Self-consistent theory at arbitrary order . . . 86
5.4.1 Self-consistent equations . . . 87
5.4.2 Convergence of self-consistent theories . . . 88
5.5 Self energy distributions . . . 91
5.5.1 End-site spectra . . . 94
5.6 Discussion . . . 94

6 The maximally-correlated chain **98**
6.1 Introduction . . . 98
6.2 Maximally correlated chain . . . 101
6.2.1 Statistics of the maximally correlated chain . . . 105
6.3 Extended, multifractal and mixed phases . . . 107
6.3.1 Distribution of tabletop lengths . . . 108

6.3.2 Generalised inverse participation ratios 113
6.3.3 The transfer matrix 114
6.4 Dynamics of the maximally correlated chain 116
6.4.1 A heuristic picture 119
6.5 Discussion 120

7 Conclusion **122**

Appendices

A Statistics of the maximally-correlated chain **133**
A.1 Multivariate Gaussian distribution of site energies 133
A.2 Pair distributions and correlated random walks 135
A.3 Distribution of average eigenvalue 136
A.4 Fluctuations in higher moments of the spectrum 138

References **141**

1 Introduction

"Localization was a different matter: very few believed it at the time, and even fewer saw its importance; among those who failed to fully understand it at first was certainly its author. It has yet to receive adequate mathematical treatment, and one has to resort to the indignity of numerical simulations to settle even the simplest questions about it."

— P. W. Anderson, Nobel Prize lecture, 1977

The phenomenon of Anderson localisation - in which the presence of disorder inhibits the diffusion of non-interacting quantum particles - is ubiquitous in nature. It bears the name of its discoverer, Philip W. Anderson, who in 1958 demonstrated that electron transport may be absent in solids if they are sufficiently disordered [4]. Today, localisation is known to occur both in single [5] and many-particle systems [6–8], and has been observed in classical systems of sound [9, 10], light [11], and microwave radiation [12, 13]. Furthermore, it is understood that localisation can occur in systems that are not truly disordered [14–27].

In this thesis, we explore the localisation properties of two classes of one-dimensional system. Both classes share the property that the energies of their sites are strongly correlated. The first, quasiperiodic models, has been studied since the 1980s [28], and is characterised by infinite-range correlations and a lack of quenched disorder. Instead, the site energies are drawn from a periodic potential that is

incommensurate with the underlying lattice, ensuring that no two sites have the same energy. These models are well known to host a variety of interesting localisation phenomena [14–27], which we seek to understand within a theoretical framework.

The second class, constituting random chains in which the site energies are *maximally* correlated [29, 30], has not as far as we are aware been studied in one dimension. The correlations in these models are system size dependent, and ensure that any two sites separated by a finite distance are completely correlated in the thermodynamic limit, such that their site energies are forced to take the same value. Our aim here is to demonstrate and explain the unusual localisation properties of these models, which include a robust phase of multifractal eigenstates and a 'mixed' phase comprising both multifractal and delocalised states.

In this Chapter, we introduce the field of localisation, beginning with Anderson's work [4]. We then trace the discovery of localisation in quasiperiodic models and, after a brief interlude to discuss many-body localisation, introduce the maximally correlated model. We end with an overview of the thesis in Sec. 1.5.

1.1 Anderson localisation

In his 1958 paper "*Absence of diffusion in certain random lattices*" Anderson explored the quantum mechanical effects of disorder in a single-particle system [4]. Specifically, his aim was to describe transport (of spins or electrons, for example) in a disordered lattice in which diffusion takes place via quantum jumps between localised sites. He constructed the simplest physical model he could think of to capture the physics: a tight-binding model, with the site energies E_j drawn independently from a probability distribution $P(E)$. This distribution has a width, W, and pairs of sites j and k have between them a hopping matrix element J_{jk} which decays with the distance r_{jk} between them. Mathematically, this model can be represented as an equation of motion for the amplitude a_j of the wavefunction on site j,

$$i\frac{\partial a_j}{\partial t} = E_j a_j + \sum_{k\neq j} J_{jk} a_k. \tag{1.1}$$

Anderson considers a particle initially placed on site j at time $t = 0$ (such that $a_j = 1$), and studies the behaviour of the wavefunction as $t \to \infty$. The essential result is that, provided $J_{jk}(r_{jk})$ falls off sufficiently rapidly with distance, for strong disorder there is no transport at all. In the infinite-time limit, the amplitude of the wavefunction falls off rapidly from site j, and a_j remains finite; in other words, the particle is localised. The eigenstates $|\alpha\rangle$ are *exponentially localised*, and can be written as

$$\langle k|\alpha\rangle \sim e^{-|k-k_0|/\xi}, \tag{1.2}$$

where ξ is the 'localisation length' of the state, and k_0 the site of peak amplitude.

The mathematics of the paper, rightly called "fairly complicated" by its author, essentially boils down to analysing the convergence properties of the renormalised perturbation series (RPS) for the self energy [31–33] in the energy domain. The self energy - in particular its imaginary part - is an order parameter for localisation: it is finite in the delocalised phase, and vanishingly small in the localised phase. Physically, the RPS corresponds to a sum over all the possible paths the particle can take out from site j and back again; convergence of the series corresponds to localisation of the particle [4, 34].

In the limit of very strong disorder, it is easy to see (in retrospect, at least) why localisation should take place. A zeroth-order description of the Hamiltonian is that each eigenstate corresponds to an 'orbital' bound to a single site by the large fluctuations in the potential. We then imagine perturbatively turning on the hopping elements J_{jk} to allow these orbitals to mix. An extended state would arise as a linear combination of infinitely many local orbitals; a localised state just a few. The reason that localisation takes place for strong disorder is that the elements $J_{jk}(r_{jk})$ are only large for orbitals close by in space. However, the probability that two nearby orbitals have a similar energy is very small when W is very large, leading to a suppression of mixing by a large energy denominator. States that are resonant, on the other hand, will typically be very far apart in space, where the hopping element is small [35].

That this result would bring about something of a paradigm shift and spawn what is now a large field of physics was not realised at the time, as Anderson stated in his Nobel Prize lecture [36]. The prize, which he received in 1977 alongside N. F. Mott and J. H. van Vleck, was "for their fundamental theoretical investigations of the electronic structure of magnetic and disordered systems" [36]. Though the original work was cited a mere thirty times in the first ten years [13], at the time of writing the number is about nine thousand[1].

One of the first major discoveries in the years following Anderson's work was that in one dimension, all eigenstates are localised for any strength W of uncorrelated disorder. This discovery is usually attributed to Mott and Twose in 1961 [37], but was only proved rigorously in 1977 by Kunz and Souillard [38]. This result also holds in two dimensions, though in three or more dimensions a *localisation transition* occurs between spatially extended states at weak disorder, and localised states at strong disorder. This strong dimensional dependence is captured by the seminal "scaling theory of localisation" [39], which we will return to shortly. Where localisation transitions are present, they depend generically on energy, leading to so-called *mobility edges*: loci of points in the energy-disorder strength plane separating localised and delocalised states. The concept was also introduced by Mott, in 1967 [40].

The presence of localisation in one dimension is significantly easier to establish than in higher dimensions, with the two-dimensional model being the subject of debate for many years [35]. The reason for this is that the RPS is relatively easy to analyse in $1d$, but in higher dimensions the presence of closed loops in the lattices makes the mathematics much more difficult. Anderson was not able to treat these loops adequately in 1958, and in the following fifteen years some inconsistencies between the predictions of his paper and numerical evidence arose, particularly in relation to uncertainty in the critical disorder strength W_c [41–45]. However, in 1973 Anderson published another influential paper, along with Abou-Chacra and Thouless, entitled "*A selfconsistent theory of localization*" [34]. Therein, the

[1] According to the Web of Science, *Absence of diffusion in certain random lattices* has been cited 9,018 times as of 06/01/2022.

authors took a different approach to the original 1958 work. Instead of summing the perturbation series to infinity, they expanded it only to second order, but the renormalised denominator - the self energy - was evaluated self consistently. Importantly, the simplification is exact on a Bethe lattice[2]. This milestone achievement both constituted the first demonstration of Anderson localisation outside of one-dimensional systems, and also confirmed Anderson's conjecture that loops are not necessary for localisation.

We do not intend to review comprehensively Anderson localisation (see Refs. [5, 35, 46] for reviews), and conclude by returning to one of the most significant works from the early years of the field. In 1979, the "gang of four" - Anderson, Abrahams, Licciardello, and Ramakrishnan - published "*Scaling Theory of Localization: Absence of Quantum Diffusion in Two Dimensions*" [39]. A radically different approach, the scaling theory parametrises the problem through the dimensionless conductance g, which is assumed to have a scaling relation $g \sim L^{\beta(g)}$, where L is the linear size of a d-dimensional sample (such that the 'volume' of the sample $\sim L^d$). By considering the asymptotic behaviour of β in the strong and weak disorder regimes, where localised and metallic behaviour are expected respectively, the *qualitative* behaviour of β can be described for all g. The results are striking. For $d = 1, 2$, $\beta < 0$ and hence g always decreases as L is increased. All states are therefore localised by even infinitesimal disorder. For $d = 3$, on the other hand, β crosses over from positive to negative as g is varied, such that a localisation transition occurs at a critical value of g. This very simple argument therefore establishes the lower critical dimension as $d = 2$ for the Anderson transition.

Wavefunctions at the Anderson transition

To close this brief introduction to Anderson localisation, we ask the following question: If the eigenstates above an Anderson transition are exponentially localised, and the eigenstates below the transition delocalised, what form do the eigenstates take precisely *at* the transition? By the early 1990s, this question began to receive

[2] A Bethe lattice is an infinite graph defined by a fixed coordination number Z and the absence of closed loops. See Sec. 2.1.6 for further details.

attention, and it was found that the states are neither localised nor delocalised, but rather characterised by *multifractal* statistics of their amplitudes [47–50]. (See also reviews in Refs. [51, 52].) Multifractal states are beautifully complex, and are characterised by the presence of both rare peaks of wavefunction amplitude and long polynomial tails; these properties often result in anomalous transport properties [53, 54]. These strange wavefunctions are sometimes called 'non-ergodic extended', as they have support on a diverging number of sites, but a vanishing fraction of the total number in the thermodynamic limit.

1.2 Localisation without disorder: Quasiperiodic models

In all of the works we have discussed so far in this introduction, localisation is present as a consequence of quenched disorder. However, in 1980 Aubry and André published a remarkable paper, titled "*Analyticity breaking and Anderson localization in incommensurate lattices*" [28]. Therein, they studied the simple physical setting of a cosine wave *incommensurate* with an underlying chain, and found that the model hosts not only a localised phase, but also a localisation transition as the amplitude of the potential is varied. Due to prior work by Harper [55], this model is often called the Aubry-André-Harper (AAH) model.

The AAH model is the simplest *quasiperiodic* model, with incommensurability brought about by the potential function's irrational wavelength. This gives rise to a 'quasi randomness': the model is deterministic, but no two sites have the same energy and hence translational invariance is lost. In other, more complicated models, mobility edges are generically found, alongside other interesting phenomena such as multifractality, mixed phases of extended and localised eigenstates, anomalous transport and robust critical phases [14–27]. Not only is the localisation phenomenology arguably richer in quasiperiodic systems than in their disordered counterparts, but they have also proved to be especially fruitful for the experimental realisation of localisation in both single and many-particle contexts [21, 56–68].

Quasiperiodic models are challenging to study theoretically. As the site energies are drawn from a deterministic function, the potential must be taken into account at all points in space simultaneously. This is in contrast to disordered systems, in which the on-site disorder can be averaged over for each site independently (assuming the most common case of independent and identically distributed site energies). Most results pertaining to quasiperiodic systems are for specific models, and a general theory is arguably lacking. In the first part of this thesis, we will develop a model-independent framework to understand localisation in quasiperiodic chains. In doing so, we will draw on many of the physical ideas presented in this introduction.

So far, the reader will note that we have ignored an important facet of localisation: the effect of particle interactions. In the next section, we provide a brief review of so-called *many-body localisation*, with a particular focus on its representation as a tight-binding problem on a complex graph [69–81].

1.3 Many-body localisation

Real systems include interactions between particles. In the early 1960s, there was concern that when these interactions are accounted for, localisation could be destroyed [13]. In 1969, Mott showed that phonons are capable of providing electrons with the necessary energy to hop to far away resonant sites [82], and the concern was that electron interactions themselves could be sufficient to act as a heat bath to enable this so-called "variable-range hopping" [83–86]. The problem remained open until 1980, until Fleishman and Anderson provided evidence against this hypothesis. The authors found that at low temperatures, short-ranged interactions are not enough to destroy localisation [87].

A great deal of work was done in subsequent decades, primarily on the ground states of disordered interacting systems [88–90]. More recently, attention has shifted to highly-excited quantum states, and the existence of localised phases at finite energy densities above the ground state. This dynamical phase of matter, occurring at a finite energy density above the ground state, is known as *many-body localisation* (MBL). Though challenging to study, both numerically and analytically [91], a rich

understanding of the phenomenon has emerged in recent years. (See reviews in Refs. [6–8].)

The stability of Anderson localisation to interactions is not only an interesting academic question. The reason that the problem has attracted so much attention is that MBL is a robust mechanism by which isolated quantum systems may fail to thermalise under their own unitary dynamics, thus positioning themselves outside the framework of conventional statistical mechanics [6]. This is often framed as a failure of MBL systems to satisfy the eigenstate thermalisation hypothesis (ETH) - essentially an application of ensemble equivalence in the limit in which the microcanonical ensemble contains a single eigenstate [92]. ETH explains the emergence of equilibrium statistical mechanics in closed quantum systems by positing that the many-body eigenstates of the Hamiltonian behave like thermal states at a temperature controlled by their energy [93, 94]. MBL systems violate the ETH as they admit an extensive set of quasi-locally conserved quantities called local integrals of motion (LIOM), leading to the indefinite preservation of information pertaining to the initial state, an absence of transport, and logarithmic spreading of entanglement [95–102]. This is in contrast to ergodic systems, for which only global quantities (particle number, energy, spin, etc.) are conserved. A particular highlight of the LIOM picture is its use in an existence proof of the MBL phase in a particular spin chain by Imbrie [103]. It took nearly twenty years for the first rigorous proof of Anderson localisation to emerge [38], and the fact that Imbrie's proof is the only one of its kind is testament to the theoretical challenge MBL presents.

Given that the problem is many-body in nature, it could be argued that the most natural place to study it is not in real space, but in the Fock space of many-body states, in which the Hamiltonian takes the form of a non-interacting tight-binding model [69–81]. However, the problem is far from trivial, as Fock space is a highly complicated network. Each node in the Fock-space graph represents an interacting many-body state, and the number of such nodes is typically exponential in the length L of the real-space chain. This is easy to see, for example, in the case of N_e spinless Fermions on a chain of length L. The dimension $N_{\mathcal{H}} = \binom{L}{N_e}$ of Fock

space is in this case equal to the number of ways of arranging N_e Fermions on L sites [72, 104]. Nodes which are separated by the hopping of a single Fermion are connected in Fock space, such that the mean coordination number of Fock space is extensive. Furthermore, given that the Hamiltonian typically contains only an $\sim \mathcal{O}(L)$ number of random variables, the energies of the nodes in Fock space must be highly correlated - a feature which distinguishes the problem from that of Anderson localisation on high-dimensional graphs. Far from being a simple oddity of Fock space, these correlations are in fact crucial to the stability of the MBL phase, and explain how localisation can survive on a graph whose average coordination number is divergent [29, 72, 104].

The Fock space approach has led to a number of important theoretical results [70, 71, 74, 76, 79, 81, 105–113]. In particular, we highlight the 2019 development of a mean-field theory for MBL in a chain of spinless Fermions by Logan and Welsh [72]. The theory correctly predicts the presence of an MBL transiton, and was later extended to a spin chain with long-ranged interactions [73]. Fock space was also the setting for a classical percolation analogue of MBL [77, 78], and more recent work has put on firmer ground the criteria that the Fock space correlations must satisfy to stabilise MBL. These correlations, far from simply being 'strong' in a loose sense, are in fact *maximal* [29, 30] - as will be defined precisely in the next section.

In this thesis, we do not venture into the field of interacting models. However, one of the systems we do study is very much conceptually connected to MBL: a $1d$ chain whose site energies are maximally-correlated in precisely the same way as the sites of an MBL problem in Fock space [29, 30]. In the next section, we briefly review the literature of correlated Anderson models before providing motivation for the study of this unusual system.

1.4 Correlated Anderson problems

Starting from a one-dimensional Anderson chain, for which all eigenstates are exponentially localised, there are several ways to effect qualitative change in the localisation behaviour. One obvious way to do this is to change the dimensionality

of the problem. Anderson localisation is strongly dependent on the dimension of the lattice, and if the lattice dimensionality were increased to three, weak disorder would no longer be sufficient to induce localisation, and a delocalised phase (along with a localisation transition) would appear. Another way to modify the localisation physics is to introduce correlations between the site energies. Though the presence of short-ranged correlations between site energies does not change the qualitative behaviour in $1d$[3], it has been shown that long-ranged correlations can lead to delocalisation and the presence of mobility edges [115–118].

In light of the extensive coordination number of Fock space, and the correlations present between its energies, an appealing model of MBL is an Anderson problem on a high-dimensional correlated lattice. However, recall that the correlations in Fock space are not just "long ranged"; Fock space is *maximally* correlated: after a suitable rescaling, the energies of any two sites separated by a finite distance have a statistical correlation of one in the thermodynamic limit, meaning that they necessarily take the same value. This behaviour could be modelled by a Cayley tree with maximal correlations, for which the connectivity K (defined in terms of the coordination number Z as $K = Z - 1$) is taken to infinity. In 2020, Roy and Logan studied localisation on Cayley trees and random regular graphs with maximally-correlated disorder [30], and found that an Anderson transition is present. Though results are primarily presented for $K = 2$, the authors also present a mean-field theory, which demonstrates that this transition occurs at a finite critical disorder strength even in the $K \to \infty$ limit. This is in stark contrast to the uncorrelated case. The work thereby probes the importance of the interplay between correlations and lattice dimensionality in supporting a stable MBL phase.

The Hausdorff dimension of a Bethe lattice for any connectivity greater than 1 is infinity. A $K = 1$ tree, however, is just a $1d$ chain, and hence the Hausdorff and Euclidean dimensions are both one. Given the strong dependence of Anderson

[3]See section 6.2, in which exponential localisation is found for $1d$ models with correlations of the form $\langle \epsilon_x \epsilon_{x+r} \rangle = a^r$, where $0 < a < 1$. See also Ref. [114], in which the presence of short-ranged correlations in three dimensions does not change the qualitative behaviour of the localisation transition.

localisation on dimensionality, a natural question to ask is: what happens to the maximally correlated model in $1d$? This question is the starting place for the second topic in this thesis. Despite its innocuous origin, the question does not have a simple answer. The maximally correlated chain displays rich and unusual localisation physics, including a robust phase of multifractal states, a delocalised phase, and between the two a mixed phase in which some disorder realisations are multifractal and some extended. Explaining the presence of these unusual phases will require a thorough analysis of the effect the maximal correlations have on the eigenspectrum of the model.

In the next section, we provide an overview of the results presented in this thesis.

1.5 Overview

We begin the thesis by laying the necessary theoretical groundwork in Chapter 2. Our fundamental object of study is the local propagator $G_j(t)$, which is the probability amplitude that a particle will be found on a site j at time t, given that it was placed there at time $t = 0$. The local propagator is sensitive to the localisation properties of the system's eigenstates, and we focus specifically on its associated self energy, which has long been appreciated as a useful probe of localisation transitions [4, 34]. A particularly helpful way to calculate the self energy is through the renormalised perturbation series (RPS) [33], which is attributed to Feenberg and Watson [31, 32], and which we derive in Sec. 2.1. Used in many of the works presented in this introduction, the RPS allows one to express propagators and self energies as sums over all of the non-repeating 'paths' that a particle can take between sites on the lattice. On Bethe lattices (and one-dimensional chains), which have no closed loops, the RPS therefore takes a particularly simple form.

Focussing on the imaginary part Δ of the self energy, we explain its utility as a probabilistic order parameter for localisation transitions. Δ is finite with probability one in the delocalised phase, and vanishingly small in the localised phase, specifically as $\Delta \propto \eta \to 0$, where η is the regulator (see Sec. 2.2 for details). This allows us to define a conjugate order parameter $y \equiv \Delta/\eta$, which by contrast is

finite in the localised phase and divergent in the delocalised phase. By studying suitably defined distributions of Δ and y, therefore, one can map out localisation phase diagrams and locate mobility edges. Due to the long tails present in these distributions, they are most aptly characterised by their geometric means, or *typical values*, Δ_{typ} and y_{typ} respectively.

Within the framework of the RPS, we also explain in how self-consistent theories (such as those in Refs. [30, 34, 72, 73]) for Δ and y may be implemented at arbitrary order, and how the self energy can be represented as a continued fraction (CF). These ideas form the basis of the analysis carried out in Chapters. 4 and 5, in which we develop a theoretical framework to understand localisation in quasiperiodic chains.

Before doing so, however, we devote Chapter 3 to an overview of quasiperiodic models. After a brief historical introduction to the field, we turn our attention to three particular models which will be used as test cases for the theory developed in subsequent chapters. We begin with the simplest model, the Aubry-André-Harper (AAH) model [28], which hosts an energy-independent localisation transition [28]. We then examine two modifications of the AAH potential that result in qualitatively different behaviour. The first, called the β model by us, is a distortion of the AAH model in which energy symmetry is lost and a single mobility edge appears [21]. The second is part of a family of so-called *mosaic models*, in which the quasiperiodic potential is interrupted by regular blocks of sites with zero potential energy [22]. As a representative of this set, we focus on the model in which every other site energy is set to zero, and two mobility edges are present alongside a central band of delocalised states.

Not only are the three models different in terms of their definitions and localisation behaviour, but exact expressions for their mobility edges (among other things) are known; this will allow us to compare our theoretical predictions to known results. By computing the localisation phase diagrams of all three models, we are able to give the reader a clear picture of where localised and delocalised states exist, and where the mobility edges intersect the bands. (For a summary figure, see Fig. 3.4.)

In Chapter 4, we construct a leading-order theory for localisation in quasiperiodic chains. Based on the ideas introduced in Chapter 2, the theory is centred around the self-consistent determination of the self energy distributions. After recapping the central equations for the self energy in Sec. 4.2, we provide numerical evidence for the scaling of Δ_{typ} in both phases, thus confirming its use as an order parameter. In Sec. 4.3, we then derive analytic (and model-independent) equations for the distributions of Δ and y, the locations of mobility edges, and of spectral band edges. Subsequently, in Secs. 4.4 and 4.5, we apply our results to the three models introduced in Chapter 3. Despite the theory's simplicity, the AAH model's energy-independent transition is exactly captured, as are the two mobility edges in the mosaic model. For the β model, the mobility edge is approximately (but rather well) captured. The distributions of Δ and y, as well as the shapes of the spectral bands, are in very good agreement with numerically obtained exact results. We conclude in Sec. 4.6 by summarising our results, and noting the areas in which the first-order theory missed certain higher-order processes, such as the presence of spectral bandgaps.

This discussion motivates the analysis in Chapter 5, in which the RPS is studied at arbitrary order. Prompted by the shortcomings of the first-order theory in capturing detail that results from long-ranged correlations in the potential, we ask whether these features are recovered as the order of theory increases. In answering this question, we also investigate the convergence properties of the continued fraction representation of the self energy.

We begin in Sec. 5.2 by setting up the basic formalism for the self energy that underpins this chapter. Exploiting the recursive structure of the RPS, we write the local propagator and its self energy in CF form. Series representations for Δ and y are then derived, with the latter taking on a particularly simple form. In Sec. 5.3, we analyse the convergence properties of these representations. In particular, we show that the series for y converges rapidly in the localised phase, yielding a finite typical value y_{typ}; in the delocalised phase by contrast, the series fails to converge and y_{typ} is divergent in the thermodynamic limit. This constitutes

the first result of this chapter: from the convergence properties of the self energy, localisation phase diagrams can be mapped out.

Self-consistent theories at arbitrary order are then presented in Sec. 5.4. These are obtained by truncating the CF and replacing the terminal self energy with a typical imaginary part. As in Sec. 5.3, the self-consistent y_{typ} is respectively finite and divergent in the localised and delocalised phases. The complementary order parameter $\Delta_{\text{typ}} \equiv \eta y_{\text{typ}}$ is by contrast finite in the delocalised phase and vanishingly small in the localised phase. Importantly, the convergence of y_{typ} is governed by the convergence of the underlying CF for y. As such, convergence of y at any point in the phase diagram implies directly the convergence of the self-consistent y_{typ} with increasing order of theory. In the thermodynamic limit, the two methods therefore give the same result, which is exact. These results place the first-order theory of Chapter 4 within a broader framework, encompassing arbitrary-order self-consistent theories and the convergence properties of the self energy. This is the second main result.

Finally, we turn in Sec. 5.5 to the distributions of Δ and y, obtained both self-consistently and directly from the CF. The two methods show excellent mutual agreement, as well as with results obtained numerically via exact diagonalisation. As with y_{typ}, the distribution $P_y(y)$ converges rapidly in the localised phase, and both methods give the exact result. In the delocalised phase, results for the distribution $P_\Delta(\Delta)$ are shown to be equivalent to distributions obtained by exact diagonalisation. In Sec. 5.6, we close with a brief discussion and directions for future work.

In Chapter 6 we introduce a new model: a one-dimensional random chain with maximally correlated disorder. We begin in Sec. 6.1 by discussing multifractal wavefunctions in physics, with an emphasis on their usually being associated with fine-tuned critical points or long-ranged models. We then introduce the maximally correlated chain, and give an overview of its unusual localisation physics. One might expect strong correlations to suppress Anderson localisation in $1d$, and indeed our first result is the presence of a delocalised phase for weak disorder strength. More surprising, and not *a priori* obvious, is the presence of a robust regime of

multifractal states for all disorder strengths greater than a critical value. These multifractal states are rather unusual in structure, bearing little resemblance to the multifractal states found at the critical points of Anderson transitions. Instead, they are roughly constant over a continuous segment of the lattice that scales non-trivially with the system size; we dub such states "tabletops".

Between the extended and multifractal phases is a mixed regime. For a given energy, some disorder realisations therein host extended states and some multifractal. Averaging over disorder in this region therefore results a spectrum in which extended and multifractal states coexist with no energy resolution between them. The presence of this regime is attributed to the strong inter-sample fluctuations in the density of states caused by the presence of maximal correlations.

The model is properly defined in Sec. 6.2, and we give there an explicit form for the maximal correlations. In particular, we focus on how the strong correlations between site energies induce realisation-to-realisation fluctuations in the eigenspectrum of the model. We present statistics relating to the correlations in the chain, and show that the strong fluctuations necessitate recentring the Hamiltonain of each model before averaging over disorder. In Sec. 6.3, we then provide numerical evidence for the three phases present in the model.

We begin by defining a useful physical quantity that lies at the centre of our analysis: the tabletop length ℓ of the eigenstates. In the extended phase, every eigenstate satisfies $\ell = L$, where L is the length of the chain. In the multifractal phase, by contrast, the tabletops are sub-extensive, and we find that their lengths scale as $\ell \sim L^{\alpha}$, where $0 < \alpha < 1$. The mixed regime is naturally described by a mixture (on a realisation-by-realisation basis) of these two types of scaling. An analysis of the distributions $P_{\ell}(\ell)$ of the tabletop lengths - and in particular how they change with system size - therefore reveals the presence of three phases. This is followed up with a scaling analysis of the mean and typical tabletop lengths.

The multifractal nature of the tabletops is probed in Sec. 6.3.2 using a standard tool: the generalised inverse participation ratio (IPR) [5]. Scaling analysis of the mean and typical IPRs reveals the presence of an extended phase for weak disorder,

as well as the multifractal nature of the sub-extensive states which appear at stronger disorder. Lastly, we probe the conductance properties of the system through a transfer matrix calculation [119–123]. We extract the distributions of transmittances, which distinguish clearly the presence of extended and multifractal states (or both).

Standard multifractal states are often associated with slow, sub-diffusive transport [54, 124, 125]. An important question therefore is: what is the imprint of our anomalous multifractal states on the dynamical properties of the system? In Sec. 6.4 we analyse the spreading of an initially localised wavepacket, and find initial ballistic transport followed by saturation. We provide a heuristic explanation for this behaviour by approximating the tabletop states as delocalised over a length ℓ of the chain. Finally, we extend the heuristic argument to explain how the tabletop states might come about as a consequence of the martingale nature [126] of the correlated potential. We close in Sec. 6.5 with a discussion of results.

The thesis is brought to a close in Chapter 7 with a summary of key results and an outline of potential future directions.

2
Background theory

Contents

2.1 Local propagators 18
2.1.1 Propagators in the time domain 18
2.1.2 Propagators in the energy domain 20
2.1.3 The operator Dyson equation 21
2.1.4 Introducing the self energy 22
2.1.5 Renormalised perturbation expansion 23
2.1.6 Bethe lattices 27
2.2 The self energy 30
2.2.1 The behaviour of Δ in localised and delocalised phases . 30
2.2.2 Two order parameters and their distributions 33
2.2.3 Δ_{typ} and y_{typ} 34
2.2.4 Relating y to the localisation length of states 34
2.2.5 The end-site self energy and approximate theories . . . 35

In this chapter, we introduce non-interacting local propagators in nearest-neighbour tight-binding models, with a particular focus on the associated self energy. In specifying the probability amplitude that a particle will be found on a particular site at time t, given that it was placed there at $t = 0$, local propagators have long been appreciated as natural probes of localisation, both in single-particle [4, 30, 34, 127–131] and many-particle settings [29, 72, 104, 132].

We begin in Sec. 2.1 with definitions of local propagators and the self energy, before constructing a renormalised perturbation series (RPS) for both [31–33]. We

then briefly discuss Bethe lattices, on which the RPS takes a simple form and admits representation as a continued fraction.

In Sec. 2.2, we turn to a detailed analysis of the self energy. We focus in particular on the imaginary part Δ of the self energy, which is a probabilistic order parameter for localisation transitions. After explaining the behaviour of the self energy in both localised and delocalised phases, we close this chapter by looking forward to Chapters 4 and 5. There, the results derived in this chapter will be used extensively in the implementation of a theoretical framework to understand localisation in quasiperiodic chains.

2.1 Local propagators

In this section, following Ref. [133], we start quite generally with a lattice described by a tight-binding Hamiltonian,

$$\hat{H} = \underbrace{\sum_j \epsilon_j |j\rangle\langle j|}_{\hat{H}_0} + \underbrace{\sum_{k\neq l} J_{kl}|k\rangle\langle l|}_{\hat{H}_1}. \tag{2.1}$$

$\{|j\rangle\}$ is a set of orthonormal basis states, obeying $\langle j|k\rangle = \delta_{jk}$, which we will label with Latin letters. On each site is an energy ϵ_j, which we do not need to specify for the time being. The hopping terms $J_{kl}|k\rangle\langle l|$ connect sites k and l with a strength given by J_{kl}. We use Greek letters to denote the eigenstates of $\hat{H}$, i.e., $\hat{H}|\alpha\rangle = E_\alpha|\alpha\rangle$, where E_α is the energy eigenvalue. The 'atomic limit' we shall call the trivial case of $J_{kl} = 0\ \forall k, l$. In this case, the eigenstates of the Hamiltonian are the eigenstates of $\hat{H}_0$: the basis states $\{|j\rangle\}$.

For the meantime, we will not specify the lattice dimensionality or connectivity, such that our results are as general as possible.

2.1.1 Propagators in the time domain

The non-interacting local propagator can be written in the time domain as

$$G_{kj}(t) = -i\theta(t)\langle k|e^{-i\hat{H}t}|j\rangle, \tag{2.2}$$

where $\theta(t)$ is a step function that imposes $t \geq 0$. This propagator is the probability amplitude that a particle initialised on site j will be found on site k a time t later. As such, we already expect local propagators to be sensitive to the localisation properties of the underlying states.

The diagonal propagator $G_{jj}(t)$ gives the return probability amplitude for a site j after time t. Expanding $|j\rangle$ in the eigenbasis of the Hamiltonian

$$|j\rangle = \sum_{\alpha} a_{\alpha j}|\alpha\rangle \quad \text{where} \quad a_{\alpha j} = \langle\alpha|j\rangle, \tag{2.3}$$

we have

$$G_{jj}(t) = -i\theta(t)\sum_{\alpha} e^{-iE_{\alpha}t}|a_{\alpha j}|^2. \tag{2.4}$$

We note here that G_{jj} is a weighted sum over all the eigenstates $|\alpha\rangle$, the weight being their amplitude $|a_{\alpha j}|^2$ on site j. We can write the return probability $P_j(t) = |G_{jj}(t)|^2$ as

$$P_j(t) = \theta(t)\sum_{\alpha,\beta} e^{i(E_{\alpha}-E_{\beta})t}|a_{\alpha j}|^2|a_{\beta j}|^2. \tag{2.5}$$

In the thermodynamic limit, the off-diagonal ($\alpha \neq \beta$) oscillatory terms cancel out, we are left only with the diagonal ($\alpha = \beta$) terms. Hence,

$$P_j^{\infty} = \sum_{\alpha} |a_{\alpha j}|^4. \tag{2.6}$$

For a localised state overlapping site j, $a_{\alpha j}$ will be an $\mathcal{O}(1)$ number independent of the system size, and hence in a phase in which *all* eigenstates are localised, P_j^{∞} will, as expected, remain finite. For a delocalised state, on the other hand, $|a_{\alpha j}| \sim N^{-1/2}$, where N is the system size, and hence if all of the eigenstates $|\alpha\rangle$ are delocalised, then the return probability will decay to zero as the particle escapes the site on which we initially place it. However, if the Hamiltonian admits both localised and delocalised states (as typically occurs, with the states separated in energy), then the return probability will not vanish, due to the contribution to P_j of the overlapping localised states. The infinite time return probability therefore only vanishes in the thermodynamic limit if *all* of the eigenstates, at *all energies*, overlapping site j

are delocalised. If even a single localised state overlaps site j, then the infinite time return probability will remain finite in the thermodynamic limit. The return probability is therefore not 'energy resolved', and cannot distinguish states which have different localisation properties and are separated in energy from each other. We will therefore focus from now on on the Fourier transform of $G_{jk}(t)$, which as a function of energy ω is suitably energy resolved.

2.1.2 Propagators in the energy domain

To obtain the propagator in the energy domain, we Fourier transform Eq. 2.2 as follows:

$$G_{kj}(\omega) = \int_{-\infty}^{\infty} \mathrm{d}t \; e^{i(\omega+i\eta)t} G_{kj}(t) = \langle k|(\omega + i\eta - \hat{H})^{-1}|j\rangle, \tag{2.7}$$

where $\eta \equiv 0^+$ is a regulator. Inserting the resolution of the identity $\mathbb{1} = \sum_\alpha |\alpha\rangle\langle\alpha|$ gives the so-called Lehmann representation of the propagator[1] [134]

$$G_{kj}(\omega) = \sum_\alpha \frac{a_{k\alpha} a^*_{j\alpha}}{\omega + i\eta - E_\alpha}. \tag{2.8}$$

The numerical computation of G_{kj} requires all of the eigenvalues and eigenvectors of the Hamiltonian $\hat{H}$ (so-called 'exact diagonalisation' [135]). By setting $k = j$ in Eq. 2.8, we obtain the diagonal propagator

$$G_j \equiv G_{jj}(\omega) = \sum_\alpha \frac{|a_{j\alpha}|^2}{\omega + i\eta - E_\alpha}, \tag{2.9}$$

which has real and imaginary parts

$$G_j(\omega) = G^R_j(\omega) - i\pi D_j(\omega), \tag{2.10}$$

such that

$$D_j(\omega) = -\frac{1}{\pi} \mathrm{Im}\; G_j(\omega). \tag{2.11}$$

To proceed, we recall the following identity. Given that $\eta \equiv 0^+$, we have

$$\frac{1}{x - x_0 + i\eta} = \mathcal{P}\left(\frac{1}{x - x_0}\right) - i\pi\delta(x - x_0), \tag{2.12}$$

[1] Note that for real symmetric Hamiltonians, the eigenstate amplitudes $\{a_{k\alpha}\}$ can always be chosen to be real.

where $\mathcal{P}$ denotes the Cauchy principle value. Using Eq. 2.9 with 2.12 then gives

$$D_j(\omega) = \sum_\alpha |a_{j\alpha}|^2 \delta(\omega - E_\alpha) \tag{2.13}$$

as the local density of states (lDoS), or local single-particle spectrum. If all of the states at a given energy are localised, then the local spectrum will be pure point-like, as only an $\mathcal{O}(1)$ number of states will overlap the site j, even in the thermodynamic limit. This implies that $D_j(\omega)$ is formed from an $\mathcal{O}(1)$ number of delta functions. If all of the states are instead delocalised, then $D_j(\omega)$ forms a continuum (specifically a branch cut). The total single-particle spectrum is given by

$$D(\omega) = L^{-1} \sum_j D_j(\omega) = L^{-1} \sum_\alpha \delta(\omega - E_\alpha). \tag{2.14}$$

2.1.3 The operator Dyson equation

From Eq. 2.7, we define the 'resolvent operator' as

$$\hat{G}(\omega) = (\omega^+ - \hat{H})^{-1}, \tag{2.15}$$

where we have subsumed the imaginary infinitesimal into the energy ω, such that $\omega^+ = \omega + i\eta$. We write the propagator G_{jk} as

$$G_{kj}(\omega) = \langle k|\hat{G}(\omega)|j\rangle. \tag{2.16}$$

$\hat{H}_0$ itself has a resolvent operator

$$\hat{G}_0(\omega) = (\omega^+ - \hat{H}_0)^{-1}, \tag{2.17}$$

with trivial matrix elements

$$\langle k|\hat{G}_0(\omega)|j\rangle = \langle k|(\omega^+ - \hat{H}_0)^{-1}|j\rangle = \delta_{kj}(\omega^+ - \epsilon_j)^{-1}. \tag{2.18}$$

To proceed, split $\hat{H}$ into $\hat{H}_0 + \hat{H}_1$ in the resolvent, such that

$$\left(1 - [\omega^+ - \hat{H}_0]^{-1}\hat{H}_1\right)(\omega^+ - \hat{H})^{-1} = (\omega^+ - \hat{H}_0)^{-1}, \tag{2.19}$$

which leads immediately to an operator Dyson equation,

$$\hat{G}(\omega) = \hat{G}_0(\omega) + \hat{G}_0(\omega)\hat{H}_1\hat{G}(\omega). \tag{2.20}$$

Eq. 2.20 could be iterated to form a series for $\hat{G}$ in terms of $\hat{G}_0$ and $\hat{H}_1$. We will return to this idea in Section 2.1.5, where the Dyson Eq. 2.20 is the starting point for the derivation of the renormalised perturbation series. Here, we note that the equation can also be written in matrix notation,

$$G_{kj}(\omega) = \langle k|\hat{G}(\omega)|j\rangle \tag{2.21}$$

$$= \langle k|\hat{G}_0(\omega)|j\rangle + \sum_{l,m}\langle k|\hat{G}_0(\omega)|l\rangle\langle l|\hat{H}_1(\omega)|m\rangle\langle m|\hat{G}(z)|j\rangle. \tag{2.22}$$

Now, $\langle k|\hat{G}_0(\omega)|j\rangle = \delta_{kj}(\omega + i\eta - \epsilon_j)^{-1}$ and $\langle k|\hat{H}_1(\omega)|j\rangle = J_{kj}$. Hence

$$(\omega^+ - \epsilon_j)G_{jk}(\omega) = \delta_{jk} + \sum_l J_{jl}G_{lk}. \tag{2.23}$$

In matrix form this reads

$$(\boldsymbol{\omega}' - \mathbf{J})\mathbf{G}(\omega) = \mathbf{1} \tag{2.24}$$

where $\boldsymbol{\omega}'_{jk} = \delta_{jk}(\omega^+ - \epsilon_j)$, $\mathbf{J}_{jk} = J_{jk}$, $\mathbf{1}_{ij} = \delta_{ij}$ and $[\mathbf{G}(\omega)]_{jk} = G_{jk}(\omega)$. The formal solution to this equation is

$$\mathbf{G} = (\boldsymbol{\omega}' - \mathbf{J})^{-1}. \tag{2.25}$$

However, the existence of a formal solution does not imply that the solution is easy to compute [133].

2.1.4 Introducing the self energy

We focus now on the site-diagonal propagator $G_j \equiv G_{jj}(\omega)$. First, note that the 'atomic limit' propagator is purely site-diagonal $\langle j|\hat{G}_0|k\rangle = \delta_{jk}g_j(\omega)$, with

$$g_j(\omega) = (\omega + i\eta - \epsilon_j)^{-1}. \tag{2.26}$$

Now, we introduce a quantity of central importance: the Feenberg self energy, $S_j(\omega)$, which is defined via [31–33]

$$G_j = \frac{1}{g_j^{-1} - S_j} = \frac{1}{\omega + i\eta - \epsilon_j - S_j}. \tag{2.27}$$

To discuss the physical meaning of S_j, note that

$$\left(g_j^{-1} - S_j\right) G_j = 1, \tag{2.28}$$

implies

$$G_j = g_j + g_j S_j G_j. \tag{2.29}$$

In the atomic limit, in which all hopping between sites is turned off, $S_j = 0$ by construction. The self energy therefore describes the effects of 'coupling' a particle on site j to the other sites. It is also clear from Eq. 2.27 that knowledge of the self energy is sufficient to obtain the full propagator G_j: this is precisely the approach we take in Chapters 4 and 5, using the renormalised perturbation series for $S_j(\omega)$. To proceed, we will first use the Dyson equation to generate unrenormalised infinite series for $G_{jj}(\omega)$ and $S_j(\omega)$.

2.1.5 Renormalised perturbation expansion

At this stage we make a convenient, though by all means not necessary assumption: that the tight-binding model Hamiltonian Eq. 2.1 has only nearest-neighbour hoppings. That is, $J_{jk} \neq 0$ only if sites j and k are nearest neighbours. The operator Dyson equation (2.20) may be iterated (dropping the explicit ω-dependence):

$$\hat{G} = \hat{G}_0 + \hat{G}_0 \hat{H}_1 \hat{G} \tag{2.30}$$

$$= \hat{G}_0 + \hat{G}_0 \hat{H}_1 \hat{G}_0 + \hat{G}_0 \hat{H}_1 \hat{G}_0 \hat{H}_1 \hat{G}_0 + \ldots \tag{2.31}$$

In matrix notation, this is

$$G_{jk} = \langle j|\hat{G}_0|k\rangle + \sum_{m,n} \langle j|\hat{G}_0|m\rangle\langle m|\hat{H}_1|n\rangle\langle n|\hat{G}_0|k\rangle \tag{2.32}$$

$$+ \sum_{m,n,p,q} \langle j|\hat{G}_0|m\rangle\langle m|\hat{H}_1|n\rangle\langle n|\hat{G}_0|p\rangle\langle p|\hat{H}_1|q\rangle\langle q|\hat{G}_0|k\rangle + \ldots \tag{2.33}$$

Now, note that $\langle n|\hat{G}_0|m\rangle = \delta_{nm} g_n$, where $g_n = (\omega + i\eta - \epsilon_n)^{-1}$. Similarly, $\langle n|\hat{H}_1|m\rangle = J_{nm}$ is only non-zero if sites n and m are adjacent. Hence

$$G_{jk} = \delta_{jk} g_j + g_j J_{jk} g_k + \sum_l g_j J_{jl} g_l J_{lk} g_k + \ldots \tag{2.34}$$

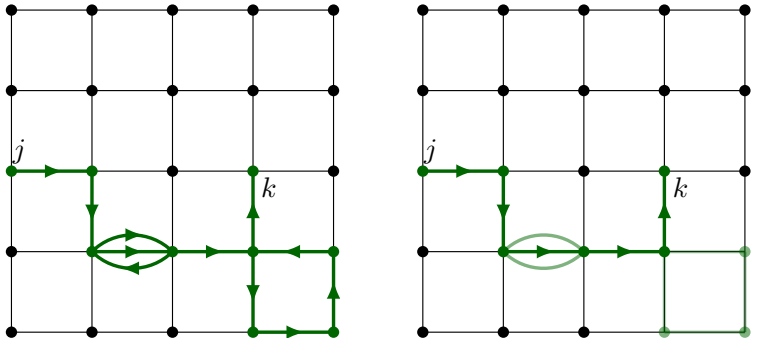


Figure 2.1: (Left) A schematic of one of the paths that make up the propagator G_{jk}. (Right) Renormalisation of the propagator involves the removal of loops from the self-avoiding 'backbones' of the paths.

This expansion has a one-to-one correspondence with the set of all possible paths linking sites j and k. An example of a path is shown in the left-hand panel of Figure 2.1. To compute the weight of each path, we associate a factor of g_m for each site m visited by the path, and for each hop between adjacent sites n and m we associate a factor of J_{nm}. The diagonal propagator G_{jj} includes the bare term g_j.

The failings of naïve perturbation theory

Naïvely writing the propagator as a sum of *all* paths between two points on the lattice leads to some serious problems. This stems from the fact that the number of paths between two sites is infinite, even for a lattice with a finite number of sites. This is because sites may repeatedly be revisited, with no restrictions, constituting "certain troublesome repeated terms" [4].

Following Anderson's argument [4], suppose that there are two adjacent sites with particularly large values of $g_k = (\omega^+ - \epsilon_k)^{-1}$. This will happen if both ϵ_k and its neighbour ϵ_l are close in magnitude to the energy ω. Provided the hopping term J_{kl} is not too small, then the 'loop' $k \to l \to k$ is associated with a weight $|g_k J_{kl}\, g_l J_{lk}| > 1$. Terms in the series which involve the particle repeatedly hopping back and forth between the two sites to form m loops will have associated with them a factor $|g_k J_{kl}\, g_l J_{lk}|^m$, which leads to trivial divergences in the series which are unrelated to the localisation properties of the problem. Instead, this is a simple failing of the perturbation theory to converge.

As an instructive way to understand the source of these divergences, focus on the Hamiltonian between two sites k and l, with a hopping term J between them:

$$H = \begin{pmatrix} \epsilon_k & J \\ J & \epsilon_l \end{pmatrix}, \tag{2.35}$$

the eigenvalues of which are

$$\epsilon_\pm = \bar{\epsilon} \pm \sqrt{\delta\epsilon^2 + J^2}, \tag{2.36}$$

where $\bar{\epsilon} = (\epsilon_k + \epsilon_l)/2$ and $\delta\epsilon = (\epsilon_k - \epsilon_l)/2$. Trying to expand the eigenvalues as a power series in J, we see that convergence is only possible if $|J/\delta\epsilon| < 1$. If the two sites are too close in energy, the perturbation series will fail to converge. These 'local resonances' are the source of the trivial divergences in Eq. 2.34 (which after all is precisely a perturbation series in J), which go as $(J/\delta\epsilon)^{2m}$, where m is the number of loops between the resonant sites [136]. As Eq. 2.34 for $G_{jk}(\omega)$ is the sum of *all* paths connecting sites j and k, and as in the thermodynamic limit it is inevitable that resonances will occur if the site energies $\{\epsilon_j\}$ are randomly distributed, Eq. 2.34 *always* diverges in the thermodynamic limit for such problems. As now described, the sum can however be renormalised to remove these trivial divergences, and to ensure thereby that the renormalised series contains only a finite number of terms for a finite system [31, 33, 34].

Feenberg's renormalised perturbation series

The path in the left-hand panel of Fig 2.1 can be recast as a 'decorated' path, which consists of a self-avoiding 'backbone' path between j and k with the 'decorations' being the paths that begin and end at sites on the self-avoiding path. This is shown in the right-hand panel, with the backbone of the path in solid green, and the decorations in faded green. Now, consider the subset of all paths which consist of the same self-avoiding backbone, the only difference between them being the decorations on a given site m. The contribution from each of these paths can be written schematically as

$$g_j J_{jp} g_p \dots J_{qm} \left[\sum (\text{decorations at } m)\right] J_{ml} \dots J_{rk} g_k. \tag{2.37}$$

However, the sum of *all* paths which start and end at any site m is G_m. Hence we can account for all these paths at once by replacing g_m with G_m in Eq. 2.34 for $G_{jk}(\omega)$. The same will be true for the next site, with one change. We have already summed *all* of the paths which visit m, and hence we must not visit site m again. We write this propagator as $G_l^{[m]}$, where the superscript $[m]$ indicates that site m has been removed. The next site after must have sites m and l removed, and is likewise written $G_n^{[m,l]}$. The full propagator may therefore be rewritten as

$$G_{jk} = g_j\delta_{jk} + G_j J_{jk} G_k^{[j]} + {\sum_l}' G_j J_{jl} G_l^{[j]} J_{lk} G_k^{[j,l]} + \ldots, \tag{2.38}$$

where the primed sum $\sum'$ indicates that the paths must be *self-avoiding*, and hence $l \neq j, k$, for instance. For the diagonal propagator G_j

$$G_j = g_j + {\sum_l}' G_j J_{jl} G_l^{[j]} J_{lj} g_j + {\sum_{k,l}}' G_j J_{jk} G_k^{[j]} J_{kl} G_l^{[j,k]} J_{kj} g_j + \ldots \tag{2.39}$$

where the last factor is g_j as all the decorations on site j were accounted for by the initial factor of G_j. Now, by the definition of the self energy S_j, $G_j = g_j + G_j S_j g_j$ (Eq. 2.29) we have

$$S_j = \sum_k J_{jk} G_k^{[j]} J_{kj} + {\sum_{k,l}}' J_{jk} G_k^{[j]} J_{kl} G_l^{[j,k]} J_{lj} + \ldots \tag{2.40}$$

S_j is thus the sum of all possible paths that begin and end at site j, with the restriction that no path may return to site j, except to terminate there. In Eq. 2.40, we have *renormalised* this sum to include only non-repeating paths, with the added complication that the sites on the paths now have associated with them Green functions themselves (though with sites appropriately removed) [31–33].

To summarise, we have written the Green functions G_{jk} and the self energy S_j as sums of *self-avoiding* paths, where each site corresponds to a diagonal Green function on a lattice where each of the previous sites in the self-avoiding path has been deleted. These are called the renormalised perturbation series for G_{jk} and S_j. They depend on site-diagonal Green functions which can themselves be written in RPS form (with appropriate sites removed). For a finite system, this process would eventually terminate to give closed solutions to the diagonal Green functions and

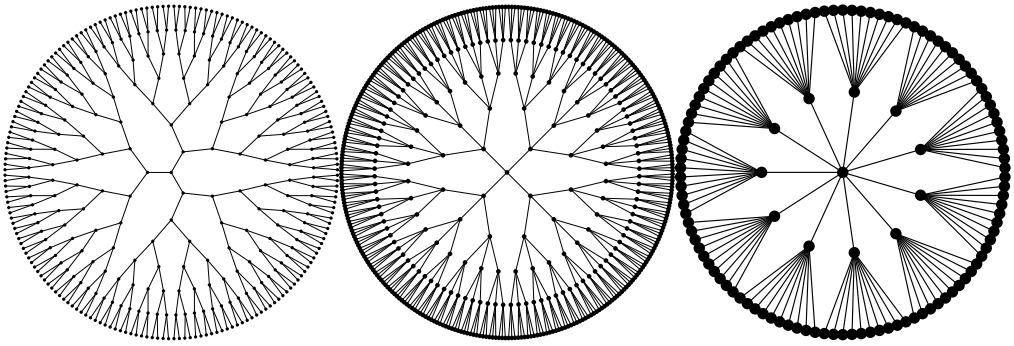


Figure 2.2: $K = 2$, $K = 3$ and $K = 10$ Cayley trees.

self energies. The formalism nevertheless remains immensely useful in dealing with thermodynamically large systems. The final RPS is non-perturbative, as each term is itself an infinite sum over types of paths. Hence, even if we terminate the RPS at first order, we are still performing an infinite sum over unrenormalised diagrams.

In this thesis, we study localisation specifically in one-dimensional tight-binding problems. A practical advantage of this choice is that the RPS greatly simplifies on Bethe lattices, of which a one-dimensional chain is the simplest member.

2.1.6 Bethe lattices

Bethe lattices - named after Hans Bethe, who introduced them in 1935 [137] - are infinite lattices with no closed loops, in which every node has the same coordination number Z. A Cayley tree shares the same structure, but is finite. Both types of graph are more commonly labelled by the connectivity $K = Z - 1$, and drawn 'generation by generation', as shown in Figure 2.2, with a 'root site' in the centre. The root site is unique for a Cayley tree, but in an infinite Bethe lattice all sites are equivalent and any site can be chosen to be the root site. Each site in a given generation, other than the first, is connected to K sites in the next, such that the total number of sites in generation m is $N_m = (K+1)K^{m-1}$ for $m > 0$, with the root site $m = 0$ satisfying $N_0 = 1$. As m increases, therefore, the number of sites in the lattice diverges exponentially for $K > 1$. A $K = 1$ Cayley tree is simply a $1d$ chain.

Bethe lattices are sometimes used as caricatures of high-dimensional Euclidean lattices; in particular, there is a strong history of studying Anderson problems on

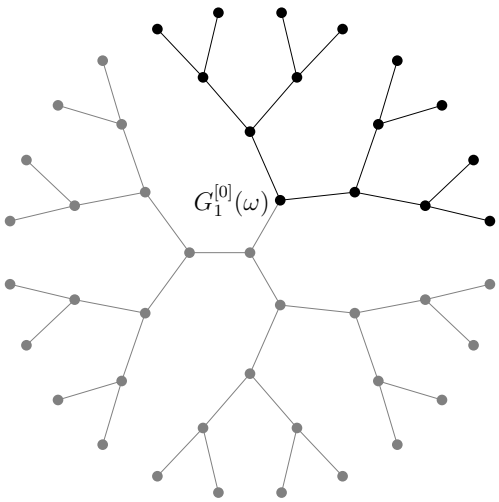


Figure 2.3: A small $K = 2$ Cayley tree, with one 'sector' of the tree in black and all the other sites greyed out. If the root site 0 is deleted, the propagator for the origin site of the black sector is $G_1^{[0]}(\omega)$.

them [34, 138–141], due in part to the simplification of the RPS.

RPS on Bethe lattices

As there are no closed loops on a Bethe lattice, only the first term in Eq. 2.40 for the self-energy $S_j(\omega)$ survives. Assuming that $J_{jk} = J$ for all nearest neighbour sites j and k, we have

$$G_j(\omega) = \frac{1}{\omega + i\eta - \epsilon_j - S_j} \quad ; \quad S_j = J^2 \sum_k G_k^{[j]}, \tag{2.41}$$

where the sum $\sum_k$ is performed over the $K + 1$ neighbours of site j. Due to the lack of loops on the lattice, deleting site j ensures that its neighbouring sites k now reside in disjoint sectors of the lattice. Furthermore, the sites k will, as a result of site j being deleted, only have K neighbours. As illustrated in Fig. 2.3, each site k therefore corresponds to the unique origin site of its sector, and has a diagonal propagator $G_k^{[j]}$. These propagators have self energies $S_k^{[j]}$ themselves, defined by

$$G_k^{[j]}(\omega) = \frac{1}{\omega + i\eta - \epsilon_k - S_k^{[j]}} \quad ; \quad S_k^{[j]} = J^2 \sum_l G_l^{[j,k]}. \tag{2.42}$$

This latter sum is performed over the K sites (labelled by l) in the next generation of the lattice which are connected to site k.

For the $K = 2$ Cayley tree shown in Fig. 2.3, deleting the root site 0 results in three disjoint sectors, each with a unique origin site. We label one of these origin sites as site 1, associated with which is the diagonal propagator $G_1^{[0]}(\omega)$. Were this process to be repeated, and site 1 deleted, then only 2 disjoint sectors would result. These sectors would be identical to the 'parent' sector, a fact embodied in the relation $G_2^{[0,1]}(\omega) \equiv G_2^{[1]}(\omega)$. This is the great simplification afforded by the Bethe lattice.

Eq. 2.42 in fact underlines all of our theoretical analysis of quasiperiodic chains. In Chapter 4 we will use it to implement a self-consistent theory for the self energy at leading order. In Chapter 5 it will then be iterated to form a continued fraction, whose convergence we study as a probe of localisation. The iteration procedure also allows us to implement self-consistent theories at *arbitrary* order, and to study the convergence of these theories as the order of implementation is increased. To conclude our discussion of Bethe lattices, we show how this continued fraction structure arises.

Continued fraction structure on Bethe lattices

Equation 2.42 for $G_k^{[j]}$ has a recursive structure, and may be iterated to give a continued fraction. The process is naturally simplest in, though not limited to, $1d$ (i.e., a $K = 1$ Bethe lattice), where Eq. 2.42 gives

$$G_k^{[k-1]}(\omega) = \frac{1}{\omega + i\eta - \epsilon_k - S_k^{[k-1]}} \quad ; \quad S_k^{[k-1]} = J^2 G_{k+1}^{[k]}. \tag{2.43}$$

Labelling the first site 0, the self energy can then be written as the following infinite continued fraction

$$S_0 = \cfrac{J^2}{\omega^+ - \epsilon_1 - \cfrac{J^2}{\omega^+ - \epsilon_2 - \cfrac{J^2}{\omega^+ - \epsilon_3 - \cfrac{J^2}{\ddots}}}}. \tag{2.44}$$

By truncating this continued fraction at progressively higher orders, the convergence properties of the self energy S_0 can be ascertained. This approach is rather similar in spirit to Anderson's original analysis of localisation [4], and will be returned to in Chapter 5.

2.2 The self energy

In this section, we obtain some key results relating to the Feenberg self energy, which demonstrate its utility as a probe of localisation. First of all, in physical terms, the meaning of the self energy is as follows:

> The imaginary part of the local self energy, $\Delta_j(\omega) = -\mathrm{Im}S_j(\omega)$, is physically the rate of loss of probability amplitude from site j to overlapping eigenstates at energy ω [31–33].

The self energy $S_j(\omega)$ has real and imaginary parts, defined via

$$S_j(\omega) = X_j(\omega) - i\Delta_j(\omega). \tag{2.45}$$

To illustrate the meaning of $\Delta_j(\omega)$, we make the simplistic (and not generally valid) assumption that the self energy $S_j(\omega) \approx S_j$ is independent of energy. Fourier transforming $G_j(\omega)$ back into the time domain then gives

$$G_j(t) = \frac{1}{2\pi}\int_{-\infty}^{\infty} \mathrm{d}\omega \, \frac{e^{-i\omega t}}{\omega - \epsilon_j - X_j + i(\eta + \Delta_j)}, \tag{2.46}$$

from which

$$G_j(t > 0) = -ie^{-(\eta+\Delta_j)t}e^{-i(\eta_j+X_j)t} \sim e^{-t/\tau}, \tag{2.47}$$

where τ is an inverse lifetime given by

$$\tau^{-1} = \eta + \Delta_j. \tag{2.48}$$

A finite value of Δ_j therefore leads to a finite rate of loss of probability amplitude from site j. We shall shortly see that in the localised phase, $\Delta_j \propto \eta \to 0$, corresponding in effect to an infinite lifetime.

2.2.1 The behaviour of Δ in localised and delocalised phases

In this section, following Ref. [72], we will demonstrate that Δ is finite in the delocalised phase and vanishingly small (specifically as $\Delta \propto \eta \to 0$) in the localised phase [127]. These properties of Δ are used extensively in Chapters 4 and 5

to distinguish the presence of localised and delocalised states. To start, we use Equations. 2.27 and 2.9 to write the S_j in terms of G_j, as

$$S_j(\omega) = \omega + i\eta - \epsilon_j - \frac{1}{G_j(\omega)} \quad \text{where} \quad G_j(\omega) = \sum_\alpha \frac{|a_{j\alpha}|^2}{\omega + i\eta - E_\alpha}. \tag{2.49}$$

With $G_j(\omega) \equiv G_j^R(\omega) - i\pi D_j(\omega)$, the imaginary part of the self energy $\Delta_j(\omega) = -\text{Im}S_j(\omega)$ is given by

$$\Delta_j(\omega) = \frac{\pi D_j(\omega)}{\left[G_j^R(\omega)\right]^2 + \left[\pi D_j(\omega)\right]^2} - \eta. \tag{2.50}$$

The real and imaginary parts of the Green function $G_j(\omega)$ are given by

$$G_j^R(\omega) = \sum_\alpha \frac{|a_{j\alpha}|^2}{(\omega - E_\alpha)^2 + \eta^2}(\omega - E_\alpha) \tag{2.51}$$

$$\text{and} \quad D_j(\omega) = \frac{1}{\pi}\sum_\alpha \frac{\eta |a_{j\alpha}|^2}{(\omega - E_\alpha)^2 + \eta^2}. \tag{2.52}$$

Deep in a delocalised regime, where eigenstates are in effect spread more-or-less uniformly over all sites, we approximate the squared amplitudes as $|a_{j\alpha}|^2 \approx 1/N$, where N is the number of sites. With this,

$$D_j(\omega) = \frac{1}{N}\lim_{\eta\to 0}\sum_\alpha \frac{\eta/\pi}{(\omega - E_\alpha)^2 + \eta^2} \equiv \frac{1}{N}\sum_\alpha \delta(\omega - E_\alpha) = D(\omega), \tag{2.53}$$

where $D(\omega)$ is the *total* density of states. As the name suggests, $D(\omega)$ is physically the number of eigenstates per unit energy, and does not depend on the localisation character of those states. It is therefore always finite if eigenstates exist at energy ω. $\Delta_j(\omega)$ is then given by

$$\Delta_j(\omega) = \frac{\pi D(\omega)}{\left[G^R(\omega)\right]^2 + \left[\pi D(\omega)\right]^2}, \tag{2.54}$$

with the real part $G^R(\omega)$ of the Green function given by the Hilbert transform of $D(\omega)$. In the delocalised phase, therefore, $\Delta_j(\omega)$ is finite. We have not assumed any specific details of models, and hence this result holds for the extended phases of all one-body problems [127].

In the localised regime by contrast, $\Delta_j(\omega) \propto \eta \equiv 0^+$ is vanishingly small. To obtain this result, set $\omega = E_\beta$ in Eqns. 2.51 and 2.52, where E_β is the eigenvalue

of some localised state labelled by β. The real and imaginary parts of the self energy are therefore given by

$$G_j^R(\omega) = \sum_{\alpha\neq\beta} \frac{|a_{j\alpha}|^2}{(E_\beta - E_\alpha)^2 + \eta^2}(E_\beta - E_\alpha)$$
$$\text{and} \quad \pi D_j(\omega) = \frac{|a_{j\beta}|^2}{\eta} + \sum_{\alpha\neq\beta} \frac{\eta|a_{j\alpha}|^2}{(E_\beta - E_\alpha)^2 + \eta^2}. \tag{2.55}$$

The central question at this point is: what happens to Eq. 2.55 as the thermodynamic limit is taken? We consider in turn those sites for which the squared amplitudes $|a_{j\beta}|^2$ remain finite, and those for which the squared amplitudes vanish in the thermodynamic limit.

In the first case, the term $|a_{j\beta}|^2/\eta$ diverges as $\eta \to 0$ and therefore dominates the expression for $\pi D_j(\omega) \sim |a_{j\beta}|^2/\eta$. $G_j^R(\omega)$ by contrast remains finite. Eq. 2.50 for $\Delta_j(\omega)$ therefore gives

$$\Delta_j(\omega) = \frac{\eta}{|a_{j\beta}|^2} - \eta. \tag{2.56}$$

For those sites on which the eigenstate β has vanishing weight in the thermodynamic limit, $|a_{j\beta}|^2/\eta$ instead vanishes. This implies that $D_j(\omega) \propto \eta$, and $G_j^R(\omega)$ is again finite. Eq. 2.50 therefore gives for these sites

$$\Delta_j(\omega) = \frac{\pi D_j(\omega)}{[G_j^R]^2} - \eta \quad (\propto \eta) \tag{2.57}$$

In both cases, therefore, $\Delta(\omega) \propto \eta \to 0$. We note that this argument depends on taking the thermodynamic limit *before* taking the limit $\eta \to 0$. If the limits are taken in the incorrect order, $\Delta_j(\omega)$ is ill-defined [72].

These results are of central important to our theory in Chapters 4 and 5. For instance, localised (delocalised) states are located using the leading-order theory (developed in Chapter 4) by looking for solutions to the approximate equations for which Δ_j is vanishing (finite).

2.2.2 Two order parameters and their distributions

Δ and y are probabilistic order parameters, fully specified by their distributions $P_\Delta(\Delta)$ and $P_y(y)$. The reader should have in mind that these distributions are formed by sampling many disorder realisations, though for the moment we do not need to be precise about exactly how this is done, as the points elaborated here are generally true.

A first instinct could be to characterise these distributions by their first moments. However, we will demonstrate that this is not possible by showing that the mean value of Δ is finite throughout both localised and delocalised phases. This in turn implies that the mean value of $y \equiv \Delta/\eta$ is divergent.

To show this result - which amounts to nothing more than Fermi's golden rule - recall that the Feenberg RPS gives to second order in the hopping element J,

$$S_j(\omega) = J^2 \sum_k G_k^{[j]} \tag{2.58}$$

on a Bethe lattice. This gives

$$\langle \Delta_j(\omega) \rangle = \pi J^2 \sum_k \langle D_k^{[j]} \rangle = \pi K J^2 D^{[j]}(\omega), \tag{2.59}$$

where $\langle \ldots \rangle$ indicates an average over disorder realisations. $D^{[j]}(\omega)$ is a disorder-averaged density of states (for the equivalent sites k with site j removed), and is finite wherever states are present. $\langle \Delta_j(\omega) \rangle$ is therefore also finite throughout both localised and delocalised phases. This result immediately implies that $\langle y_j \rangle \equiv \langle \Delta_j \rangle / \eta$ is divergent, meaning that the distribution of y generically has no first moment. This leads us to suspect that $P_y(y)$ is likely to be characterised by a power-law tail for large y:

$$P_y(y) \sim y^{-\gamma} \quad \text{for} \quad y \gg 1 \quad \text{where} \quad 1 < \gamma < 2, \tag{2.60}$$

with $\gamma > 1$ ensuring that $P_y(y)$ is normalisable, and $\gamma < 2$ that the distribution has no first moment. Such a power law tail (with $\gamma = 3/2$ specifically), indeed appears to be a generic feature of the localised phase [72], and shall be recovered within our theory of quasiperiodic models in Chapter 4. In one-dimensional single-particle

disordered systems, this result can be shown to follow from Ref. [142], and it appears to hold also in many-body systems in Ref. [72].

2.2.3 Δ_{typ} and y_{typ}

Given that $\langle\Delta_j\rangle$ is always finite, appropriate order parameters accompanying the heavy-tailed distributions are their *geometric* means, or typical values, which we denote Δ_{typ} and y_{typ}. Δ_{typ} is finite in the delocalised phase, and vanishes as $\Delta_{\text{typ}} \propto \eta$ in the localised phase. y_{typ}, on the other hand, is finite in the localised phase and divergent in the delocalised phase.

2.2.4 Relating y to the localisation length of states

Another reason why the self energy is a useful order parameter is that it can directly probe the localisation length of localised states close to the transition [2]. As the transition is approached from the localised side, y diverges with the same exponent as the localisation length of exponentially localised states. Assume that a state $|\beta\rangle$ is localised on site 0 with energy E_β, such that $|\langle j|\beta\rangle|^2 \sim e^{-j/\xi}$. Requiring that $\sum_j |\langle j|\beta\rangle|^2 = 1$ (normalisation) gives

$$|\langle j|\beta\rangle|^2 = (1 - e^{-1/\xi})e^{-j/\xi}. \tag{2.61}$$

Now, we use the relation $\Delta_j(\omega) = \text{Im}G_j^{-1}(\omega) - \eta$, and note that for $\omega \sim E_\beta$,

$$G_j(\omega) = \sum_\alpha \frac{|\langle j|\alpha\rangle|^2}{\omega^+ - E_\alpha} \quad \approx \quad \frac{|\langle j|\beta\rangle|^2}{\omega^+ - E_\beta}. \tag{2.62}$$

From Eq. 2.62, the residue of the pole of the propagator G_j at $\omega = E_\beta - i\eta$ is therefore the wavefunction density of eigenstate $|\beta\rangle$ at site j. This implies

$$\Delta_j(\omega = E_\beta) = \frac{\eta}{|\langle j|\beta\rangle|^2} - \eta, \tag{2.63}$$

which is exactly Eq. 2.56. Solving for $|\langle 0|\beta\rangle|^2$ then yields

$$|\langle 0|\beta\rangle|^2 = (1 + y_0(E_\beta))^{-1}, \tag{2.64}$$

where $y_0 \equiv \Delta_0/\eta$, which can be combined with the previous result to give

$$y_0(E_\beta) = (1 - e^{-1/\xi})^{-1} - 1 \quad \sim \quad \xi \quad \text{for} \quad \xi \gg 1. \tag{2.65}$$

Close to a transition, therefore, $y_0(\omega) \sim \xi$, and hence the two diverge with the same exponent on approaching a transition from the localised side.

2.2.5 The end-site self energy and approximate theories

To conclude this chapter, we explain how the RPS for the self energy can be used to form a self-consistent theory of localisation at arbitrary order - anticipating the methods of Chapters 4 and 5. In one dimension, the Green function for a site j in the bulk of the chain is given by

$$G_j(\omega) = \frac{1}{\omega + i\eta - \epsilon_j - S_j(\omega)} \quad \text{where} \quad S_j(\omega) = J^2 \left(G^{[j]}_{j+1}(\omega) + G^{[j]}_{j-1}(\omega) \right). \quad (2.66)$$

Knowledge of the end site propagators $G^{[j]}_{j\pm1}$ is therefore sufficient to recover the full propagator; hence localisation or its absence may be determined by examining end-site propagators alone. We therefore denote the 'end site self energy' as

$$S_0(\omega) = J^2 G^{[0]}_1(\omega), \quad (2.67)$$

where we have labelled the end-site of the semi-infinite half chain as site 0 for convenience. As for general Cayley trees, we focus on the end site not because of the simplicity of the equations for S_0, but because S_0 is a function of S_1 - another end-site self energy - and so on. In fact, by iterating Equation 2.67, we can express S_0 in terms of the self energy S_ℓ of any site with $\ell > 0$. The essence of our approach is:

1. Express S_0 as a function of S_ℓ for $\ell > 0$.

2. Replace S_ℓ with a typical imaginary part: $S_\ell \to -i\Delta_{\text{typ}}$.

3. Form a distribution of S_0 over disorder. This distribution depends on the input Δ_{typ}.

4. Impose self-consistency by requiring that the typical value of Δ_0 as obtained from the distribution be equal to the input Δ_{typ}.

This constitutes a self-consistent mean field theory at order ℓ. In Chapter 4, this process is carried out at leading order, at which analytic results can be derived, and is shown to capture very well the localisation phase diagrams and qualitative features of a broad range of quasiperiodic models. In Chapter 5, higher-order theories are studied and connections made between the convergence of the results there obtained and the convergence of the continued fraction (Sec. 5.2).

3

Quasiperiodic models

Contents

3.1 The beginning: the Aubry-André-Harper model 38
3.2 Post-Aubry-André-Harper models 40
3.3 Summary of models and localisation phase diagrams . 42
3.3.1 The Aubry-André-Harper model 43
3.3.2 The β model 43
3.3.3 The mosaic models 44
3.3.4 Computation of spectra 45

"Common sense tells us that there can be no physical effect stemming from the irrationality of some parameter, because an arbitrarily small change in that parameter would make it rational - and this would create some physical effect with the property of being everywhere discontinuous, which is unreasonable. The only alternative, then, is to show that a theory which apparently distinguishes between rational and irrational values of some parameter does so only in a mathematical sense, and yields physical observables which are nevertheless continuous."

— D. R. Hofstadter, Phys. Rev. B **14**, 2239–2249 (1976)

Before presenting theoretical results in Chapters 4 and 5, we provide in this chapter a brief introduction to quasiperiodic systems, and present known results pertaining to three diverse models. These models will be used to test the theory

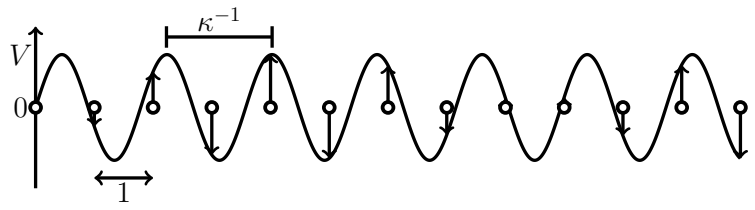


Figure 3.1: A schematic of the Aubry-André-Harper model. The separation between sites (shown as circles) is 1, and the height of the arrows on each site corresponds to the on-site potential energy. The wavelength of the cosine wave, from which the energies are drawn, is κ^{-1}, where κ is an irrational number. As such, no two site energies are the same.

developed in subsequent chapters in part by comparison to the known exact results presented here. We begin by discussing the AAH model, the first of its kind [28].

3.1 The beginning: the Aubry-André-Harper model

Quasiperiodic models made their début in the localisation community in 1980, when Aubry and André published a proof that their eponymous model hosts a localisation transition [28]. The model had been studied previously in different contexts, most notably by Harper as model of conduction electrons in magnetic fields [55], and for this reason it is often referred to as the Aubry-André-Harper (AAH) model. The simplest quasiperiodic model, it consists of a regular $1d$ chain of sites with energies drawn from a cosine function, as shown in Figure 3.1. Importantly, the cosine function has an irrational wavelength, and hence never repeats itself on the chain. This gives rise to what might be described as a 'quasi-randomness'; the model is deterministic, but no two site energies are the same, and hence translational invariance is lost.

The Hamiltonian of the Aubry-André-Harper model is a simple tight-binding chain,

$$\hat{H} = V \sum_{j=0}^{L-1} \cos(2\pi\kappa j + \phi)|j\rangle\langle j| + J \sum_{j=0}^{L-1} |j\rangle\langle j+1| + |j+1\rangle\langle j|, \tag{3.1}$$

where $V \geq 0$ is the strength of the potential - or amplitude of the wave - and L the number of sites in the chain. $J \geq 0$ controls the strength of the hopping element between nearest-neighbour sites, and may be set to 1 without loss of generality.

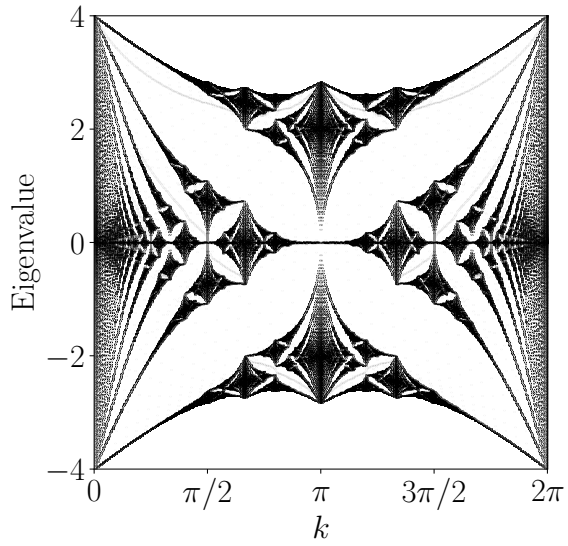


Figure 3.2: A plot of the eigenvalues of the AAH Hamiltonian equation 3.1 at the point $V = 2J$, for $k \equiv 2\pi\kappa$ between 0 and 2π. A system of size $L = 2500$ with $\phi = 0$ is used. This gives the Hofstadter butterfly [151].

Incommensurability is brought about by choosing κ to be an irrational number (here the golden ratio, $\kappa = (1 + \sqrt{5})/2$), and ϕ is an arbitrary phase factor that is common to all sites. By varying ϕ, each site in the chain experiences the full range of the potential function. ϕ therefore in effect plays the role of a disorder realisation in accumulating statistics (for instance, distributions of the self energy).

It is worth mentioning that the AAH model has also been studied in the mathematics community, where it is known as the *almost Mathieu operator* on a lattice [143–149]. The spectrum of the model, as first conjectured by Aubry and André (and later proven [150]), has measure $|4J - 2V|$ for $V \leq 2J$, such that the measure is zero at the point $V = 2J$. This critical point was studied by Hofstadter in 1976 [151]; Hofstadter showed that the spectrum is a Cantor set, and that if you plot said spectrum as a function of κ, the famous Hofstadter butterfly emerges, as shown in Fig. 3.2.

This critical point $V = 2J$ is in fact the minimum potential strength required to localise all of the eigenfunctions of the Hamiltonian. The central result of Aubry and André's paper [28] is that For $V < 2J$ all of the wavefunctions are delocalised and extended across the entire chain as modulated plane waves, while for $V > 2J$ all the

wavefunctions are exponentially localised with a common localisation length, given by $\xi = \log(V/2J)^{-1}$. As $V \to 2J^+$, ξ diverges as $\xi \sim (V - 2J)^{-1}$. The localisation transition is therefore energy independent, with all eigenstates localising/delocalising simultaneously as V is varied. This energy symmetry follows from a duality in the Hamiltonian [28]. With a change of basis defined by the Fourier transform

$$|\tilde{p}\rangle = \frac{1}{\sqrt{L}} \sum_{j=0}^{L-1} e^{i(2\pi\kappa\tilde{p}+\phi)j+i\tilde{p}\phi} |j\rangle \quad \text{and} \quad |j\rangle = \frac{1}{\sqrt{L}} \sum_{\tilde{p}=0}^{L-1} e^{-i(2\pi\kappa\tilde{p}+\phi)j-i\tilde{p}\phi} |\tilde{p}\rangle, \tag{3.2}$$

the Hamiltonian Eq. 3.1 is mapped onto itself as

$$H(V, J) \leftrightarrow H\left(2J, V/2\right). \tag{3.3}$$

Precisely *at* $V = 2J$, therefore, the Hamiltonian is self-dual, taking exactly the same form in both position and momentum bases. As the Fourier transform Eq. 3.2 maps localised states to delocalised states (and vice versa), it follows that an energy-independent localisation transition must occur at $V = 2J$. The AAH model is something of a special case in possessing this duality; a generic perturbation to the Hamiltonian will destroy the energy symmetry, leading to a mobility edge [14–27].

Lastly, we note that the curious properties of the Hamiltonian precisely at $V = 2J$ are reflected in its eigenstates. These eigenstates must be identical in two reciprocal bases, and hence cannot be localised or delocalised. Instead, they are somewhere in-between: they are *multifractal* [14]. The study of such 'anomalous' wavefunctions - albeit in a different setting - forms a large part of Chapter 6. In the next section, we turn to the development of new quasiperiodic models in the decades following Aubry and André's paper.

3.2 Post-Aubry-André-Harper models

In the years following Aubry and André's paper, a number of authors began to investigate modifications to the cosine potential, with one particular aim being the identification (usually numerically) of mobility edges. In 1982, Soukoulis and Economou provided evidence that the potential $\epsilon_j = V[\cos(2\pi\kappa j+\phi)+\frac{1}{3}\cos 2(2\pi\kappa j+\phi)]$ hosts a mobility edge, and Aubry found a very similar result for a model with

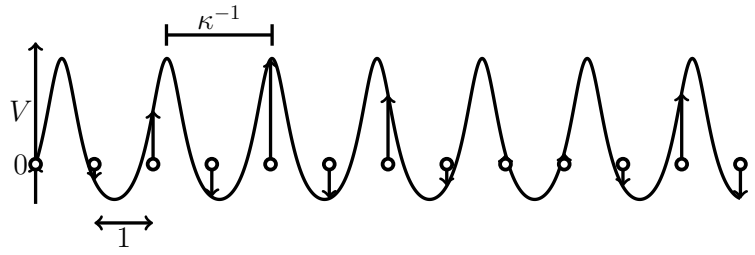


Figure 3.3: A schematic of the β model, with potential energy given by Eq. 3.4 with $\beta = 0.5$.

different coefficients [131, 152]. However, the first functional form for a mobility edge was not given until 1988, when Das Sarma, He and Xie provided robust numerical evidence for the model defined by $\epsilon_j = \cos(2\pi\kappa j^\alpha + \phi)$, for $\alpha < 1$, hosts two mobility edges at energies given by $\omega_\pm = \pm(2 - V)$ for $V \leq 2$. The authors remarked

> "Our discovery of a mobility edge in this one-dimensional problem is quite interesting because the popular wisdom has been that one-dimensional models, particularly in the gapless spectrum of a one-dimensional Schrödinger operator, do not allow for the existence of a mobility edge." [15]

The number of models now studied is vast, as there is no limit to the number of different ways of composing and distorting incommensurate functions to create new models. We therefore focus our attention on two particular models to stand alongside the AAH model as test subjects for our theory. The models are chosen for two reasons. First, the locations of their mobility edges are known exactly, thus providing a convenient measure of the accuracy of any theory developed. Second, the three models manifest quite different localisation phenomenology. Together, they will therefore probe the applicability of our theory to general models.

The first of these models is referred to by us as the β model, and its potential is a distortion of the Aubry-André-Harper potential, $\epsilon_j^{\text{AAH}} = \cos(2\pi\kappa j + \phi)$, as

$$\epsilon_j^\beta = \frac{\epsilon_j^{\text{AAH}}}{1 - \beta\epsilon_j^{\text{AAH}}}, \tag{3.4}$$

for $|\beta| < 1$. The model was introduced by Ganeshan, Pixley and Das Sarma in Ref. [21], and hosts a single linear mobility edge whose gradient depends on the value of β chosen, given by $\beta\omega_{\text{ME}} = 2J - V$.

A schematic of the β model for $\beta = 0.5$ is given in Figure 3.3. In skewing the potential function, and hence the energy spectrum, the energy symmetry of the AAH model is destroyed. For positive β, $|\max \epsilon_j^\beta| > |\min \epsilon_j^\beta|$ - leading to an eigenvalue spectrum skewed towards positive energies (as illustrated below in Fig. 3.4). Within these bounds, however, the distribution of site energies is skewed towards lower values of ϵ_j^β. This is seen as the 'troughs' are broader than the 'peaks' in the figure. As a result of this, sites lower in energy are more likely to have a neighbouring site with a similar energy to which they can resonantly hop. Lower energy states therefore remain delocalised for larger values of V than higher energy states [59], explaining the asymmetry of the mobility edge. A negative value of β gives precisely the reverse behaviour.

The second modification to the AAH potential involves setting the potential of regular blocks of sites to zero, creating a so-called *mosaic* model [22]. For simplicity, we focus on the model for which every other site in an AAH chain has its potential set to zero. This model has two symmetric mobility edges enclosing a central band of delocalised states that persists for large potential strengths, with the states precisely at the band centre never localising [22].

In addition to capturing the locations of the mobility edges, we hope that any theory developed for quasiperiodic chains will also capture the structure of the localisation phase diagram, including the band edges of the spectrum. In the next section, we use numerical exact diagonalisation to plot these spectra, and present a summary of some known exact results for all three models, for future reference.

3.3 Summary of models and localisation phase diagrams

In this section, we summarise the analytic results pertaining to the AAH, β and $l = 2$ mosaic models [21, 22, 28], for reference in Chapters 4 and 5. We also present the localisation phase diagrams of the models, as obtained from the numerical exact diagonalisation of large systems.

All three quasiperiodic models are one-dimensional nearest-neighbour tight-binding chains, such that the results of Chapter 2, pertaining to local propagators and their self energies, may be used. We write the general Hamiltonian as

$$H = V \sum_{j=0}^{L-1} \epsilon_j |j\rangle\langle j| + J \sum_{j=0}^{L-2} [|j\rangle\langle j+1| + |j+1\rangle\langle j|] \,, \tag{3.5}$$

where L is the length of the chain, and $V \geq 0$ is the magnitude of the on-site quasiperiodic potential, the form of which is encoded in ϵ_j. The hopping strength is controlled by J, and is the same for all pairs of adjacent sites.

3.3.1 The Aubry-André-Harper model

This simple model is defined via

$$\epsilon_j^{\mathrm{AA}} = \cos(2\pi\kappa j + \phi), \tag{3.6}$$

with κ an irrational number which brings about the incommensurability of the potential with the underlying lattice. In this thesis, we choose κ to be the Golden mean[1] [28, 55]. The model hosts an energy-independent localisation transition at $V = 2J$, and in the localised phase the states all have the same localisation length, given by [28]

$$\xi = \frac{1}{\log(V/2J)}. \tag{3.7}$$

The spectrum of the AAH model is symmetric in energy, with numerous fractal bandgaps, as seen in Figure 3.4.

3.3.2 The β model

The β model is defined via [21]

$$\epsilon_j^{\beta} = \frac{\cos(2\pi\kappa j + \phi)}{1 - \beta\cos(2\pi\kappa j + \phi)} \equiv \frac{\epsilon_j^{\mathrm{AA}}}{1 - \beta\epsilon_j^{\mathrm{AA}}}, \tag{3.8}$$

where $|\beta| < 1$. This model is a *deformation* of the Aubry-André-Harper model; in this thesis we will consider $\beta > 0$ (without loss of generality) when comparing our theoretical results to numerics, for which the spectrum acquires a

[1] Results are insensitive to the choice of κ, provided that it is irrational.

skew towards positive values of ω, as seen in Fig. 3.4. As shown in Ref. [21] by considering an energy *dependent* duality transformation, the β model possesses a single mobility edge given by

$$\beta\omega_{\mathrm{ME}} = 2J - V. \tag{3.9}$$

As $\beta \to 0$, $\epsilon_j^{\beta} \to \epsilon_j^{\mathrm{AA}}$ and consequently the mobility edge Eq. 3.9 becomes a straight line parallel to the energy axis at $V = 2J$. This mobility edge is plotted atop the exact numerical spectrum in Fig. 3.4.

3.3.3 The mosaic models

The mosaic models [22] depend on a parameter $l \in \mathbb{Z}^+$, and are defined via

$$\epsilon_j = \begin{cases} \cos(2\pi\kappa j + \phi) & : \ j = lk \\ 0 & : \ \text{otherwise} \end{cases}, \tag{3.10}$$

where $k \in \mathbb{Z}$. The mosaic models therefore consist of blocks of size l within which the first site has an AAH potential, and the remaining sites zero potential. In Ref. [22] the authors determined the locations of the mobility edges through a Lyapunov exponent calculation, finding that for a given value of V, the mobility edges are located at energies ω_{ME}, given by the solutions to the equation

$$\left|\frac{Va_l}{2}\right| = 1 \quad \text{where} \quad a_l = \frac{1}{\sqrt{\omega^2-4}}\left[\left(\frac{\omega+\sqrt{\omega^2-4}}{2}\right)^l - \left(\frac{\omega-\sqrt{\omega^2-4}}{2}\right)^l\right]. \tag{3.11}$$

For $l = 1$, $a_l = 1$ and hence the AAH transition at $V = 2$ is recovered. For simplicity, we focus on the $l = 2$ Mosaic model in the rest of this thesis, which has two hyperbolic mobility edges satisfying

$$\omega_{\mathrm{ME}} = \pm\frac{2J^2}{V}. \tag{3.12}$$

As can be seen in Fig. 3.4, these two mobility edges enclose a central band of delocalised states, with states localising first at the edges of the band. At the band centre $\Delta_{\mathrm{typ}}(\omega = 0)$, states are always delocalised.

3.3.4 Computation of spectra

In Sec. 2.2, we introduced the self energy, and focussed in particular on its imaginary part Δ, which is finite in the delocalised phase and vanishingly small in the localised phase (specifically as $\Delta \propto \eta \to 0$, where η is the regulator[2]). Its conjugate order parameter, $y \equiv \Delta/\eta$, is by contrast finite in the localised phase and divergent in the delocalised phase. In this section, we utilise these properties of Δ and y to map out numerically the localisation phase diagrams of all three models.

As explained in Sec. 2.2.5, we focus in this thesis on the end sites of semi-infinite half chains. This is because the theory developed in Chapters 4 and 5 is formulated explicitly in terms of the end-site self energy. To create a localisation phase diagram, therefore, we must compute $\Delta_0 = -\mathrm{Im}S_0$ for the end site 0 of a finite-size system, from which follows $y_0 \equiv \Delta_0/\eta$. For quasiperiodic models, we average these quantities over many ϕ values to obtain Δ_{typ} and y_{typ} as the geometric means of Δ_0 and y_0.[3]

To compute Δ_0 and y_0 for a given value of ϕ, we use exact diagonalisation [135] to obtain the eigenvalues and eigenvectors of large (but finite) systems. The Lehmann representation (defined in Eq. 2.8) is then used to compute the propagator $G_0(\omega)$, and hence its associated self energy $S_0(\omega) = [G_0(\omega)]^{-1} - \omega^+ + V\epsilon_j$, where $\omega^+ = \omega + i\eta$. In order to average over ϕ, this process is repeated for many values of $\phi \in [0, 2\pi)$.

Provided that a sufficiently large system size is employed, localised and delocalised states can be distinguished by the magnitudes of $\Delta_{\mathrm{typ}}/y_{\mathrm{typ}}$. In Fig. 3.4 we plot the spectra of all three models alongside the exactly-known mobility edges. The spectra are created by plotting the eigenvalues of 5000 realisations of a chain of length $L = 2500$ against V. Each eigenstate is coloured according to the value of $\Delta_{\mathrm{typ}}/y_{\mathrm{typ}}$ at an energy equal to the corresponding eigenvalue; for the system size employed, the two phases are thus clearly distinguished, and the mobility edges well captured.

We note that the colouring of the spectra is necessary, as the density of eigenvalues *per se* is unrelated to the localisation properties of the states. However,

[2]For finite-size systems, η cannot be set to zero. Rather, it must be on the order of the level spacing between eigenvalues, $\eta \sim \mathcal{O}(1/L)$, where L is the chain length. See Sec. 4.2.1 for details.

[3]Recall from Sec. 2.2.2 that the arithmetic mean of Δ is always finite, implying that the arithmetic mean of y is divergent. This is due to the heavy-tailed nature of the self energy distributions; in such cases the geometric mean is the most appropriate definition of typicality.

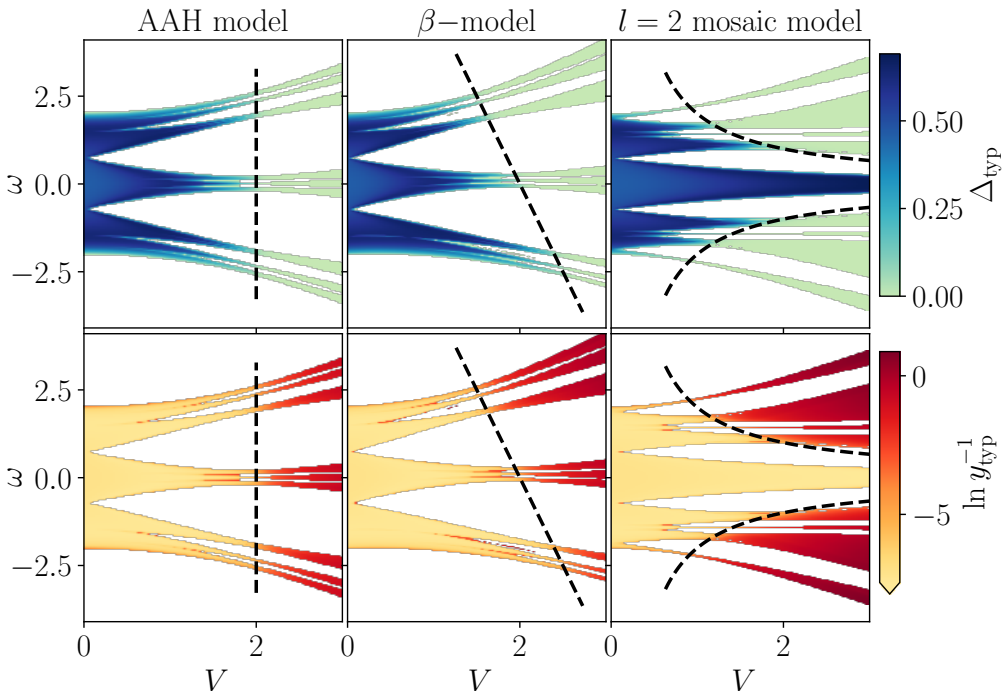


Figure 3.4: Spectra for the three models studied in this thesis as a function of the potential strength V, colour coded according to the values of Δ_{typ} (top row) and y_{typ} bottom row. The black dashed lines are the exact mobility edges, separating the localised and extended phases. A finite value of Δ_{typ} indicates delocalised states, and a vanishingly small value localised states. As a consequence, y_{typ} is finite in the localised phase and divergent in the extended phase. All data are computed for chains of length $L = 2500$ over 5000 values of ϕ, with $\eta = 1/L$ and $J = 1$. For the β model, $\beta = 0.2$ is employed for illustration.

two notable features are present in the spectra themselves. First, the spectra broaden as V is increased, and second, each spectrum has numerous fractal bandgaps [153]. When theories are developed for the self energy in the next two chapters, we will be interested in whether the localised and delocalised phases (and accompanying mobility edges) are recovered, and also whether these intrinsic spectral properties are reflected in the results.

In the next Chapter, one of our aims is to use the first-order theory to generate localisation phase diagrams for all three models present here, comparing our results to Fig. 3.4.

4

Leading-order self-consistent theory

Contents

4.1 Introduction 48
4.2 The self energy 49
4.2.1 Numerical computation 51
4.3 First-order self-consistent theory 52
4.3.1 Localised phase 53
4.3.2 Delocalised phase 54
4.3.3 Mobility edge condition 54
4.3.4 Distributions of Δ and y 55
4.3.5 Band edges and density of states 56
4.4 First-order phase diagrams 58
4.4.1 Aubry-André-Harper model 58
4.4.2 β model 60
4.4.3 Mosaic model 63
4.4.4 Numerical solutions to mean-field equations 66
4.4.5 Comparison to exact results 66
4.5 Distributions at first-order 68
4.5.1 Aubry-André-Harper model 69
4.5.2 β and Mosaic models 72
4.5.3 Comparison to numerical results 73
4.6 Conclusion 76

"It can be a disadvantage rather than an advantage to be able to compute or to measure too accurately, since often what one measures or computes is irrelevant in terms of mechanism. After all, the perfect computation simply reproduces Nature, does not explain her."

— P. W. Anderson, Nobel Prize lecture, 1977

4.1 Introduction

The methods used to prove exact results for quasiperiodic models are many and varied, and often specific to the particular model. Aubry and André's original paper proved the presence of a localisation transition by constructing an energy-independent duality transformation [28]. Likewise, several more recent works have constructed energy-*dependent* duality transformations to extract the mobility edges of more complicated models [21, 23, 154]. Another approach has been to relate two models with known mobility edges with a duality transformation [155], and Lyapunov exponent calculations have been used to extract the localisation lengths of states, and hence also the locations of mobility edges [22, 156].

It is therefore desirable to develop a theory of localisation in quasiperiodic chains that is model-independent, and which could be used to understand new models. In this chapter, we take a step towards this goal by constructing a simple approximate theory. The theory, of a self-consistent nature, is built around the self energy $S_j(\omega)$, introduced in Chapter 2. In particular, we focus the imaginary part of the self energy, $\Delta_j(\omega) = -\mathrm{Im}\, S_j(\omega)$, which physically is the rate of loss of probability amplitude from a site j into participating states of energy ω. A natural diagnostic of localisation, the characteristics of $\Delta_j(\omega)$ have long proven successful in understanding Anderson transitions [4, 34, 45, 127–129].

In the delocalised phase, $\Delta_j(\omega)$ is finite (non-zero) with unit probability, and in the localised phase vanishes as $\Delta_j(\omega) \propto \eta \to 0$, where η is the regulator. We therefore define a conjugate order parameter $y_j(\omega) \equiv \Delta_j(\omega)/\eta$, which is finite in the localised phase and divergent in the delocalised phase. With these two

order parameters, the localisation phase diagrams, and corresponding mobility edges, can be mapped out. The essential result of this chapter is a series of approximate, model-independent equations for the distributions (and corresponding typical values) of Δ_j and y_j.

We begin in Sec. 4.2 by recalling the definition of the self energy and explaining how it is computed numerically using exact diagonalisation. We then demonstrate the validity of Δ_j and y_j as order parameters for localisation transitions. Throughout this chapter, we compare the predictions of our theory with analytic results for the three models introduced in Chapter 3: the Aubry-André-Harper model, the β model and the $l = 2$ mosaic model [21, 22, 28].

The central mean-field equations for the self energy in both phases are then derived in Sec. 4.3. This is followed by derivations of model-independent equations for the locations of mobility edges and spectral band edges, for distributions of Δ and y, and for the density of states.

An important test of the validity of the theory is how well it reproduces the numerically exact localisation phase diagrams presented in Fig. 3.4. In Sec. 4.4 we use the mean-field equations to map out the phase diagrams of all three models, and find results to be in very good qualitative agreement with the exact results. Lastly, in Sec. 4.5, we compare the first-order expressions for the distributions of Δ and y to numerical results, and show that the approximate theory captures the qualitative features of the distributions in both phases. We close in Sec. 4.6 with a brief discussion of our results, and of future directions.

4.2 The self energy

In this section, we recap the definition the self energy $S_j(\omega)$ (specifically for one-dimensional nearest-neighbour systems) and present numerical results for its imaginary part, demonstrating that the latter acts as an order parameter for localisation transitions. The models considered in this chapter (introduced in Chapter 3) are one-dimensional tight-binding chains. Models in higher dimensions, or with longer-ranged hoppings, are also of interest [20, 23, 24, 155, 157–159],

though the structure of the resultant equations for the self energy is significantly more complicated.

In general, the local self energy $S_j(\omega)$ is defined by the Green function $G_j(\omega)$ as $G_j(\omega) = [\omega + i\eta - V\epsilon_j - S_j(\omega)]^{-1}$ (Eq. 2.27), where $\eta \equiv 0^+$, and $S_j(\omega) = X_j(\omega) - i\Delta_j(\omega)$. For the one-dimensional nearest-neighbour models considered here, S_j can be expressed in terms of the half-chain propagators of the sites adjacent to it

$$S_j(\omega) = J^2 \left[G^{[j]}_{j-1}(\omega) + G^{[j]}_{j+1}(\omega) \right], \tag{4.1}$$

where $G^{[j]}_{j+1}$ is the Green function for site j with the previous site removed. The localisation properties of the eigenstates of the Hamiltonian are thus encoded fully in the *end-site* propagators $G^{[j]}_{j\pm1}(\omega)$. Dropping the superscripts, we therefore consider from now on the self energy of an end site with index 0, $S_0(\omega) \equiv S_0^{[-1]}(\omega)$. As $S_0(\omega)$ is connected only to the site to its right, Eq. 4.1 simplifies to $S_0(\omega) = J^2 G_1^{[0]}$. S_0 may therefore be written in terms of S_1,

$$S_0(\omega) = \frac{J^2}{\omega + i\eta - V\epsilon_1 - S_1(\omega)}, \tag{4.2}$$

where the dependence of S_0 on the site-energies $(\epsilon_2, \epsilon_3, \ldots, \epsilon_{L-1})$ of the rest of the chain is parametric in S_1, which can likewise be expressed in terms of S_2, and so on. The recursive structure of these equations leads to the continued fraction representation of the self energy, introduced in Sec. 5.2. As the imaginary part of the self energy is finite (non-zero) in the delocalised phase and vanishing in the localised phase, the convergence properties of this continued fraction must also be a probe of localisation. This approach is similar to Anderson's original method [4], and is the main theme of Chapter 5. Here, we consider the continued fraction only at first order, but in a self-consistent fashion, and focus on approximating Eq. 4.2 such that it can be solved analytically. In this context, "first order" means that $S_0(\omega)$ depends explicitly only on the energy $V\epsilon_1$ of site 1.

Before we implement the first-order mean-field theory, we explain in the following section how the self energy is computed numerically, and show its validity as an order parameter for localisation transitions.

4.2.1 Numerical computation

The end-site Green function $G_0(\omega)$ is computed numerically using the Lehmann representation (Eq. 2.8), which in terms of the half-chain eigenstates $|\psi_n\rangle$ and eigenvalues E_n reads

$$G_0(\omega) = \sum_{n=1}^{L} \frac{|\langle 0|\psi_n\rangle|^2}{\omega + i\eta - E_n}, \tag{4.3}$$

from which S_0 follows as $S_0 = \mathrm{Im}G_0^{-1} - \eta$. We then define $\Delta = -\mathrm{Im}S_0$ and $y \equiv \Delta/\eta$. By sampling Eq. 4.3 over many values of ϕ (for some chosen energy ω), we may compute the distributions of Δ and y, and their geometric means (or typical values) Δ_{typ} and y_{typ}.

At this stage, we briefly remark on how the regulator η is handled in numerical calculations. Strictly speaking, the limit $\eta \to 0$ should only be taken *after* the limit $L \to \infty$ has been taken (see Sec. 2.2.1). However, all calculations are necessarily performed for finite-size systems. In a finite system, η may not simply be set to zero, reflecting the fact that finite-size systems have discrete spectra even in cases when the thermodynamic limit would yield a continuous spectrum [72]. The smallest energy scale in a finite-size system is the typical eigenvalue spacing, which is of order $1/L$, and hence we take $\eta \sim \mathcal{O}(L^{-1})$, which gives the correct limiting behaviour as L is increased.[1] The practical effect of having a finite value of η is that all delta functions are broadened into Lorentzians of half-width η - for instance in Eq. 2.13 for the density of states. This is necessary to obtain smooth results for such functions, which would otherwise be point-like for finite L.

We have already seen evidence for the efficacy of the self energy as an order parameter for localisation transitions. In Fig 3.4, we plotted the localisation phase diagrams of three quasiperiodic models by colour-coding their spectra with Δ_{typ} and y_{typ}. However, this calculation was for a single system size, and so in Fig. 4.1 we show how Δ_{typ} scales with system size L in the two phases. As expected, Δ_{typ} is finite in the delocalised phase, and in the localised phase vanishes as $\Delta_{\mathrm{typ}} \sim \mathcal{O}(L^{-1})$. Precisely *at* the transition, an anomalous decay $\Delta_{\mathrm{typ}} \sim L^{-\alpha}$ is observed, with

[1] We let $\eta = a/L$, where $a \sim \mathcal{O}(1)$. Results are insensitive to the precise value of a chosen.

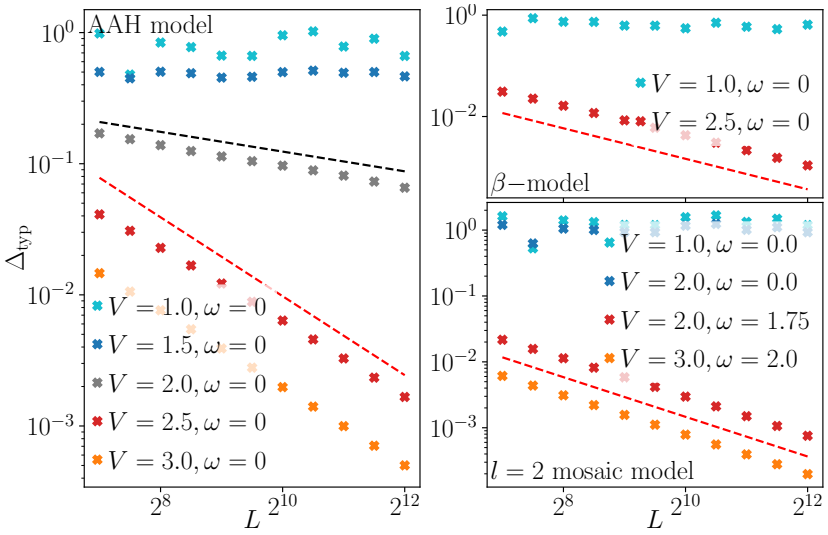


Figure 4.1: Plots of Δ_{typ} as a function of system size L at representative points in the (V, ω)-plane for all three models. Data in blue correspond to the delocalised regime, in which Δ_{typ} is finite, and red/orange to the localised phase, in which Δ_{typ} vanishes as L^{-1} (shown as red dashed lines). For the Aubry-André-Harper model, we also show data *at* the critical point $V = 2$, where $\Delta_{\mathrm{typ}} \sim L^{-0.25}$ (dashed black line) decays to zero with an anomalous power. All data points are accumulated over 5000 values of ϕ.

$\alpha = 0.25$ for the parameters used. This reflects the underlying multifractal states of quasiperiodic models at criticality.

In the next section, we implement the first-order mean-field approximation, allowing us to derive approximate analytic expressions for both Δ_{typ} and the underlying distribution of Δ.

4.3 First-order self-consistent theory

From Eq. 4.2 for $S_0(\omega)$, the mean-field approximation is to replace $S_1(\omega)$ with a *typical* self energy, $S_1(\omega) \to -i\Delta_{\mathrm{typ}}(\omega)$, from which we obtain the central mean-field equation for $\Delta = -\mathrm{Im}S_0(\omega)$ as[2]

$$\Delta(\omega) = \frac{J^2(\eta + \Delta_{\mathrm{typ}}(\omega))}{(\omega - V\epsilon_1(\phi))^2 + (\eta + \Delta_{\mathrm{typ}}(\omega))^2}. \tag{4.4}$$

This equation is pertinent to both localised and delocalised phases, and will be solved self-consistently. The site energy $\epsilon_1(\phi)$ depends on the phase ϕ, which is

[2]Note that the real part $X_1(\omega)$ of $S_1(\omega)$ has been dropped. In Chapter 5, higher-order theories will be shown to include exactly contributions from the real parts of the self energies.

common to all quasiperiodic models and plays the role of the disorder realisation in accumulating statistics. We therefore form the distribution $P_\Delta(\Delta)$ of Δ by sampling equation 4.4 over many ϕ-values. Self-consistency is achieved by requiring that the geometric mean of this distribution be equal to the input Δ_{typ}. That is,

$$\log \Delta_{\text{typ}} = \int_0^\infty \mathrm{d}\Delta \ \log(\Delta) P_\Delta(\Delta; \Delta_{\text{typ}}), \tag{4.5}$$

where we have made explicit the dependence of $P_\Delta(\Delta)$ on Δ_{typ}. Though Eq. 4.5 provides an intuitive definition of Δ_{typ}, we will usually compute it directly from Eq. 4.4 for simplicity,

$$\log \Delta_{\text{typ}} = \int_0^{2\pi} \mathrm{d}\phi \ \log \Delta(\phi; \Delta_{\text{typ}}), \tag{4.6}$$

where we have made explicit the fact that Δ as defined in Eq. 4.4 takes Δ_{typ} as an input parameter. In the following, we set $J = 1$ without loss of generality.

4.3.1 Localised phase

In the localised regime, $\Delta_{\text{typ}}(\omega) \sim \eta \to 0^+$, such that $y_{\text{typ}}(\omega) \equiv \Delta_{\text{typ}}(\omega)/\eta$ is finite. This reduces Eq. 4.4 to give $y \equiv \Delta/\eta$ as

$$y(\omega) = \frac{1 + y_{\text{typ}}(\omega)}{(\omega - V\epsilon_1)^2}. \tag{4.7}$$

Until now, we have implicitly considered only models for which there is one 'class' of end site, and hence one function $\epsilon_1(\phi)$ on which y and Δ depend. However, for some models there are multiple choices for the functional form of the end site; the $l = 2$ mosaic model, for instance, could have either no potential or an AAH potential on the root site. In such cases, we need to average over classes of end site as well as over ϕ. With $\langle\langle \ldots \rangle\rangle$ denoting an average over both end sites and ϕ values, the self-consistency condition in the localised phase is

$$\log y_{\text{typ}} = \langle\langle \log y \rangle\rangle. \tag{4.8}$$

Combining Equations 4.7 and 4.8, and making our averaging explicit, we obtain an expression for y_{typ},

$$\log\left(\frac{1 + y_{\text{typ}}}{y_{\text{typ}}}\right) = \frac{1}{2\pi n_0} \sum_{j_0} \int_0^{2\pi} \mathrm{d}\phi \ \log(\omega - V\epsilon_{j_0}(\phi))^2, \tag{4.9}$$

where $\{j_0\}$ label the n_0 distinct end sites. For the Aubry-André-Harper and β models, there is just one distinct class of sites, and the additional site-averaging is unnecessary. We note that, due to the integration over ϕ, there is no explicit dependence of y_{typ} on the site index chosen to label the end site (hence our freedom to choose $j = 0$). It is for this reason that we need only average over end sites which have different functional forms of their on-site potentials.

Eq. 4.9 will be analysed in detail in Sec. 4.4 for all models considered.

4.3.2 Delocalised phase

In the delocalised phase, we may let $\eta \to 0$ from the outset as Δ_{typ} is finite, reducing Eq. 4.4 to

$$\Delta = \frac{\Delta_{\text{typ}}}{(\omega - V\epsilon_1)^2 + \Delta_{\text{typ}}^2}. \tag{4.10}$$

The self-consistency condition is

$$\log \Delta_{\text{typ}} = \langle\langle \log \Delta \rangle\rangle, \tag{4.11}$$

which gives the integral equation

$$\frac{1}{2\pi n_0} \sum_{j_0} \int_0^{2\pi} \mathrm{d}\phi \ \log\left((\omega - V\epsilon_{j_0}(\phi))^2 + \Delta_{\text{typ}}(\omega)^2\right) = 0, \tag{4.12}$$

which is satisfied for each ω-point by the function $\Delta_{\text{typ}}(\omega)$.

In the following sections, we derive equations for important features of the localisation phase diagrams. These results will be applied to concrete models and compared to exact results in Sec. 4.4.

4.3.3 Mobility edge condition

To locate mobility edges, we look for solutions to Eq. 4.7 as $y_{\text{typ}} \to \infty$ and Eq. 4.12 with $\Delta_{\text{typ}} = 0$. Both equations generate the same result,

$$\sum_{j_0} \int_0^{2\pi} \mathrm{d}\phi \ \log(\omega_{\text{ME}} - V\epsilon_{j_0}(\phi))^2 = 0, \tag{4.13}$$

where as before the sum $\sum_{j_0}$ is taken over unique end sites. The theories in both phases are therefore consistent; on approach to the localisation transition, the same

mobility edges are recovered. By solving Eq. 4.13 for a given model, the mobility edge(s) ω_{ME} can be obtained as a function of V.

4.3.4 Distributions of Δ and y

By solving Eqs. 4.12 and 4.7, we can obtain the functions $\Delta_{\mathrm{typ}}(V,\omega)$ and $y_{\mathrm{typ}}(V,\omega)$ respectively. Both Δ and y are, however, probabilistic order parameters, specified in full by their distributions $P_\Delta(\Delta)$ and $P_y(y)$. Though the geometric means are undoubtedly useful order parameters - particularly when it comes to mapping out phase diagrams and locating mobility edges - the distributions naturally contain more information. Over an ensemble of ϕ values, the distribution $P_\Delta(\Delta)$ is defined as

$$P_\Delta(\Delta) = \frac{1}{2\pi n_0}\sum_{j_0}\int_0^{2\pi} \mathrm{d}\phi\, \delta\left(\Delta - f_{j_0}\right) \quad \text{where} \quad f_{j_0} = \frac{\Delta_{\mathrm{typ}}}{(\omega - V\epsilon_{j_0})^2 + \Delta_{\mathrm{typ}}^2}. \tag{4.14}$$

Employing a change of variable $\phi \to f$, $P_\Delta(\Delta)$ can be written

$$P_\Delta(\Delta) = \frac{1}{2\pi n_0}\sum_{j_0}\sum_{\phi^*}\left|\frac{\partial f_{j_0}}{\partial \phi}\right|^{-1}_{\phi=\phi^*}, \tag{4.15}$$

where $\{\phi^*\}$ is the set of solutions to the equation $f(\phi^*) = \Delta$. Similarly,

$$P_y(y) = \frac{1}{2\pi n_0}\sum_{j_0}\int_0^{2\pi} \mathrm{d}\phi\, \delta\left(y - g_{j_0}\right) \quad \text{where} \quad g_{j_0} = \frac{1+y_t}{(\omega - V\epsilon_{j_0})^2}. \tag{4.16}$$

With the change of variable now $\phi \to g$, the localised-side distribution can be written

$$P_y(y) = \frac{1}{2\pi n_0}\sum_{j_0}\sum_{\phi^*}\left|\frac{\partial g_{j_0}}{\partial \phi}\right|^{-1}_{\phi=\phi^*}, \tag{4.17}$$

with $\{\phi^*\}$ the set of solutions to $g(\phi^*) = y$. In terms of these distributions, the self consistency requirements Eqns. 4.8 and 4.11 can be written as

$$\log\Delta_{\mathrm{typ}} = \int_0^\infty \mathrm{d}\Delta\; P_\Delta(\Delta)\log\Delta \quad \text{and} \quad \log y_{\mathrm{typ}} = \int_0^\infty \mathrm{d}y\; P_y(y)\log y. \tag{4.18}$$

For quasiperiodic potentials which are finite for all $\phi \in [0, 2\pi)$ (which is the case for the three models considered in this chapter), Eq. 4.16 implies that $P_y(y)$ will have a hard lower cut-off. Likewise, Eq. 4.14 implies that $P_\Delta(\Delta)$ will have both lower and upper cut-offs. This behaviour is also seen in the exact numerical results for all three models (see Sec. 4.5).

Universality of Lévy tail in the localised phase

The presence of a power-law tail $P_y(y) \overset{y\gg 1}{\sim} y^{-3/2}$ appears to be a universal feature of the localised phases of random models, in both single-particle and many-body contexts [72, 142] (see Sec. 2.2.2). Here, we show that within the framework of the leading-order theory, the same feature is present in the localised phases of quasiperiodic models. To this end, consider the band centre $\omega = 0$, and substitute g (Eq. 4.16) into Eq. 4.17. This gives

$$P_y(y) = y^{-3/2} \frac{\sqrt{1+y_{\text{typ}}}}{4\pi V n_0} \sum_{j_0} \sum_{\phi^*} \left| \frac{\partial \epsilon_{j_0}}{\partial \phi} \right|^{-1}_{\phi=\phi*}, \tag{4.19}$$

with the only explicit dependence on y contained in the factor of $y^{-3/2}$, which dominates for $y \gg 1$.[3] The presence of a Lévy tail appears to be an inevitable consequence of the structure of the first-order equations, not the specific potential used.

4.3.5 Band edges and density of states

Δ_{typ} is an *end-site* quantity, defined as the geometric mean (over values of ϕ and end sites) of $\Delta_0 \equiv -\text{Im}S_0$, for the end site 0 of a semi-infinite half chain. With $J = 1$, $S_0(\omega) = G_1(\omega)$, where $G_1(\omega) = G_1^R(\omega) - i\pi D_1(\omega)$ is the local propagator for site 1 with site 0 deleted. Δ_{typ} is therefore proportional to the typical *end-site* density of states $D_{\text{typ}}(\omega) \equiv \exp\langle\langle \log D_1(\omega)\rangle\rangle$,

$$\Delta_{\text{typ}} = \pi D_{\text{typ}}(\omega). \tag{4.20}$$

A finite value of Δ_{typ} (from Eq. 4.12) therefore indicates the presence of delocalised states at a particular point in the (V, ω) plane; points where Δ_{typ} vanishes can be identified either as band edges, beyond which there are no states, or transitions to localised states (where it is accompanied by a divergent y_{typ} from the other side). The mean density of states on the other hand remains finite across mobility edges and

[3] The precise quasiperiodic potential ϵ_j chosen affects only the small-y behaviour of $P_y(y)$ for all models tested.

throughout the localised phase. To probe the localised regime, therefore, we compute the average density of states at first order, which with $\Delta(\omega)$ given by Eq. 4.4 is

$$\begin{aligned}\bar{D}(\omega) &= \langle\langle \Delta(\omega)/\pi \rangle\rangle \\ &= \frac{1}{2\pi n_0} \sum_{j_0} \int_0^{2\pi} \mathrm{d}\phi \, \frac{1}{\pi} \frac{(\eta + \Delta_{\mathrm{typ}})}{(\omega - V\epsilon_{j_0}(\phi))^2 + (\eta + \Delta_{\mathrm{typ}})^2}.\end{aligned} \tag{4.21}$$

In the localised regime, $\Delta_{\mathrm{typ}} \propto \eta$, whence taking the limit $\eta \to 0$ gives

$$\bar{D}(\omega) = \frac{1}{2\pi n_0} \sum_{j_0} \int_0^{2\pi} \mathrm{d}\phi \, \delta(\omega - V\epsilon_{j_0}). \tag{4.22}$$

This result implies that states in the localised phase exist only in the region

$$\min\{V\epsilon_{j_0}(\phi)\} < \omega < \max\{V\epsilon_{j_0}(\phi)\}, \tag{4.23}$$

i.e., for a range of ω bounded by the maximum and minimum value of the site potential over ϕ and end sites $\{j_0\}$. Using Eqs 4.20 and 4.22, we may map out the band edges of arbitrary spectra (within our first-order approximation).

Eq. 4.22 is intuitive as a first-order approximation to the mean density of states, with the exact result following from Eq. 2.13 for $D_j(\omega)$ as

$$\bar{D}^{\mathrm{exact}}(\omega) = \frac{1}{2\pi n_0} \sum_{j_0} \int_0^{2\pi} \sum_{\alpha} |a_{j_0\alpha}|^2 \delta(\omega - E_\alpha), \tag{4.24}$$

with E_α the eigenvalue of eigenstate α, and $|a_{j_0\alpha}|$ its amplitude on the end site j_0. Deep in the localised phase, Eq. 4.22 will become quantitatively accurate, as in the limit $V \to \infty$ (or equivalently $J \to 0$), the Hamiltonian $\hat{H} \to V \sum_j \epsilon_j |j\rangle\langle j|$, whence the eigenenergies are simply the site energies. Eq. 4.22 may therefore be understood as the large V limit of the exact density of states Eq. 4.24.

To summarise, mobility edges are located as the loci of points for which $\Delta_{\mathrm{typ}}(\omega) = 0$ and $y_{\mathrm{typ}}(\omega) \to \infty$, and which lie within the spectral band edges. These band edges are located as separate loci of points for which either the mean (in the localised regime) or typical (in the delocalised regime) density of states vanishes. In the next section, we will apply these results to the Aubry-André-Harper , β and $l = 2$ mosaic models, comparing the predictions of the first-order theory to known exact results.

4.4 First-order phase diagrams

The purpose of this section is to use the leading-order theory to generate localisation phase diagrams for all three models defined in Sec. 3.3. In each phase, we will first compute the density of states in order to locate the spectral band edges. Within the band, we will then look for solutions to Eqs. 4.9 and 4.12 for y_{typ} and Δ_{typ} respectively, analysis of which will yield the locations of the mobility edges. Taken together, these results will allow us to map out phase diagrams which can be compared directly with the exact results presented in Fig. 3.4.

4.4.1 Aubry-André-Harper model

The AAH model is something of a special case as it lacks a true mobility edge. Instead, it possesses an energy-*independent* localisation transition at $V = 2$ (with $J = 1$ as before). Modifications to the Hamiltonian invariably lead to the destruction of the 'vertical' transition and the emergence of a mobility edge (as illustrated previously in Fig. 3.4). As mobility edges are the norm for quasiperiodic models, the AAH model is an ideal test-case for the first-order theory. Somewhat remarkably, the first-order theory will be shown to capture *exactly* the AAH model's fine-tuned transition. We begin by determining the band edges of the localised phase.

Localised phase

To determine the boundaries of the localised phase, we first compute the mean density of states in the localised phase from Eq. 4.22, which for the Aubry-André-Harper model can be written

$$\bar{D}(\omega) = \frac{1}{2\pi}\int_0^{2\pi} \mathrm{d}\phi\, \delta(\omega - V\cos(\phi)) = \frac{1}{\pi\sqrt{V^2-\omega^2}}, \tag{4.25}$$

for $|\omega| < V$, giving the localised-side band edges as $\omega_{\pm}^{L} = \pm V$. As $\bar{D}(\omega)$ is a continuous function, the first-order theory predicts a continuous band of states for $V > 2$, which is symmetrical and broadens linearly as V is increased. In Fig. 3.4, the numerical spectrum for the AAH model was likewise seen to broaden as V is increased. As $V \to \infty$, the leading-order theory in fact captures exactly the locations of the

band edges, which are found numerically to lie at $\omega_{\pm} = \pm V$. This reflects the result in Sec. 4.3.5 that the leading-order mean density of states becomes exact as $V \to \infty$.

However, the first-order theory naturally misses the spectral bandgaps which are present in the exact spectrum. We return to this point in Sec. 4.4.5, where we discuss how the deficiencies of the first-order theory prompt our creation of higher-order theories in Chapter 5.

Turning to y_{typ}, we look for solutions to Eq. 4.7 within the bounds of the spectrum, which for the AAH model is

$$\log\left(\frac{1+y_{\text{typ}}}{y_{\text{typ}}}\right) = \underbrace{\frac{1}{2\pi}\int_0^{2\pi} \mathrm{d}\phi \ \log(\omega - V\cos(\phi))^2}_{I}. \tag{4.26}$$

For $|\omega| < V$, the integral I is readily solved by substitution to yield

$$I = \log V^2 + \frac{1}{2\pi}\int_0^{2\pi} \mathrm{d}\phi \ \log\left(\frac{\omega}{V} - \cos(\phi)\right)^2 = \log V^2 - \log 4, \tag{4.27}$$

leading to

$$y_{\text{typ}} = \frac{4}{V^2 - 4}, \tag{4.28}$$

for $V > 2$. As $V \to 2^+$, $y_{\text{typ}} \sim (V-2)^{-1}$ diverges with exponent 1, and there is no dependence of y_{typ} on ω. The exact result - an energy-independent transition at $V = 2$ - is therefore recovered. This same condition is naturally obtained by the mobility edge condition Eq. 4.13, which corresponds to setting $y_{\text{typ}}^{-1} = 0$. The unit exponent with which y_{typ} diverges is also the exponent with which the localisation length diverges (see Sec. 2.2.4), and is the exact result [28]. We will find that this unit critical exponent is shared by all three models.

Delocalised phase

As the function $\Delta_{\text{typ}}(\omega, V)$ is proportional to the typical density of states at the point (ω, V) (from Eq. 4.20), the delocalised-side band edges and mobility edges of a given model may be found by examining where $\Delta_{\text{typ}}(V, \omega)$ vanishes. In general, the integral Eq. 4.12 does not readily yield analytic solutions for $\Delta_{\text{typ}}(V, \omega)$. However,

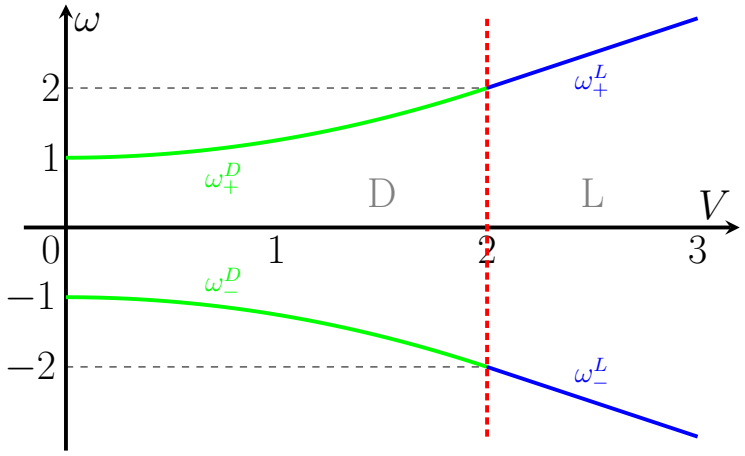


Figure 4.2: Schematic localisation phase diagram for the Aubry-André-Harper model. The locations of band edges are shown in green (delocalised) and blue (localised), and the mobility edge is shown as a dashed red line. 'L' and 'D' represent localised and delocalised states respectively. See main text for discussion.

by using the $V = 0$ result for Δ_{typ} as a starting point, we have been able to infer the following solution (which has been checked numerically) for the AAH model:

$$\Delta_{\text{typ}}(\omega) = \frac{4 - V^2}{8}\sqrt{4 - \left(\frac{8}{4 + V^2}\right)^2 \omega^2} \quad \text{for} \quad |\omega| < \frac{4 + V^2}{4}, \tag{4.29}$$

holding in the delocalised phase for $V < 2$. As $V \to 2^-$, $\Delta_{\text{typ}} \sim (2 - V)$ vanishes with the same exponent 1 as y_{typ} diverges from the other side of the transition, and the same energy-independent localisation transition at $V = 2$ is recovered.

Away from the transition at $V = 2$, the vanishing of Δ_{typ} gives the delocalised-side band edges as

$$\omega_\pm^D = \pm(4 + V^2)/4. \tag{4.30}$$

In contrast to the localised side, the band edges $\omega_\pm^D$ of the delocalised phase are curved functions of V, and smoothly evolve into $\omega_\pm^L$ as the transition is approached.

We are therefore able to present in Fig. 4.2 a schematic phase diagram for the Aubry-André-Harper model at first order, showing the location of the mobility edge and of the band edges in both phases.

4.4.2 β model

The β model is a deformation of the AAH model; by increasing β from zero, the vertical AAH transition is tilted to form a mobility edge and the spectrum

becomes asymmetric (as seen in Fig. 3.4). The β model therefore possesses several qualitative features which which we can test the first-order theory. In all cases, we will find excellent agreement between the theory and known exact results. We begin in the localised phase.

Localised phase

For the β model, Eq. 4.22 for the mean density of states in the localised phase gives

$$\bar{D}(\omega) = \frac{1}{\pi\left(1+\frac{\beta\omega}{V}\right)\sqrt{(\beta\omega+V)^2-\omega^2}}, \tag{4.31}$$

for $|\omega| < |\omega\beta + V|$. Once again, a smooth band of states is predicted, and the asymmetry of the band (seen in Fig. 3.4) is correctly captured, with the β-dependent band edges given by

$$\omega_{\pm}^{L} = \pm\frac{V}{1\mp\beta}, \tag{4.32}$$

which are exact in the limit $V \to \infty$. For $y_{\text{typ}}(\omega) \equiv \Delta_{\text{typ}}(\omega)/\eta$, Eqn. 4.7 gives

$$y_{\text{typ}} = \frac{\lambda^2}{(\omega\beta+V)^2-\lambda^2} \quad \text{where} \quad \lambda = 1+\sqrt{1-\beta^2}. \tag{4.33}$$

The condition $y_{\text{typ}}^{-1} = 0$ gives the location of a single mobility edge at

$$\omega_{\text{ME}} = \beta^{-1}[\lambda - V] \overset{\beta\ll 1}{\sim} \beta^{-1}(2-V)\,. \tag{4.34}$$

Close to this mobility edge,

$$y_{\text{typ}} \sim \frac{\lambda}{2}(\omega\beta + V - \lambda)^{-1} \tag{4.35}$$

diverges with the same exponent 1 as in the AAH model. As per the discussion in Sec. 2.2.4, this is the exponent with which the localisation length ξ diverges as the transition is approached, and is the exact result [22, 28]. The first-order theory recovers the energy-dependent mobility edge for the β model, which is a straight line whose gradient depends on the parameter β. Eq. 4.34 agrees qualitatively with the exact result $\omega_{\text{ME}} = \beta^{-1}(2-V)$, and is quantitatively correct in the limit $\beta \to 0$. Setting $\beta = 0$ naturally returns the results for the Aubry-André-Harper model.

The locations at which the mobility edge enters and exits the band - $V^{\pm}$, respectively - are given by equating the mobility edge $\omega_{\mathrm{ME}}(V)$ (Eq. 4.34) and the band edges $\omega_{\pm}^{L}(V)$ (Eq. 4.32), as

$$V_{\pm} = (1 \pm \beta)\lambda \quad \text{where} \quad |\omega| = \lambda, \tag{4.36}$$

which again reduces to the AAH result ($V_{\pm} = 2$, $|\omega| = 2$) for $\beta = 0$.

Delocalised phase

We have not been able to find complete analytic solutions for $\Delta_{\mathrm{typ}}(V, \omega)$ for the β and mosaic models. Nonetheless, key information pertaining to the band edges and mobility edges may be extracted analytically. In the delocalised phase, setting $\Delta_{\mathrm{typ}} = 0$ in Eq. 4.12 gives an integral equation,

$$\frac{1}{2\pi}\int_{0}^{2\pi} \mathrm{d}\phi \, \log\left(\omega - \frac{V\cos(\phi)}{1 - \beta\cos(\phi)}\right) = 0, \tag{4.37}$$

which admits as solutions curves describing both the mobility edge and band edges. To obtain the mobility edge, we consider $|\omega| < |\omega\beta + V|$, which positions us within the boundaries of the localised band and gives as a solution exactly Eq. 4.34. To locate the band edges, however, we assume $|\omega| > |\omega\beta + V|$, which gives the condition

$$|\omega| + \sqrt{\omega^2 - (\omega\beta + V)^2} = \lambda, \tag{4.38}$$

the solutions to which are

$$\pm\omega_{\pm}^{D} = \frac{\lambda \mp V\beta - \sqrt{(1-\beta^2)\lambda^2 \mp 2V\beta\lambda}}{\beta^2}. \tag{4.39}$$

Note that care must be taken when solving Eq. 4.38 to avoid spurious solutions introduced by squaring both sides of the equation. In Fig 4.3, we present the first-order phase diagram for the β model (shown for illustration for $\beta = 0.2$). The spectrum is skewed towards positive energies, and the two phases separated by a linear mobility edge whose gradient decreases as β is increased. As before, the localised-side band edges (Eq. 4.32) are exact in the $V \to \infty$ limit, and otherwise are in qualitative agreement with the numerically exact spectrum (Fig. 3.4). The

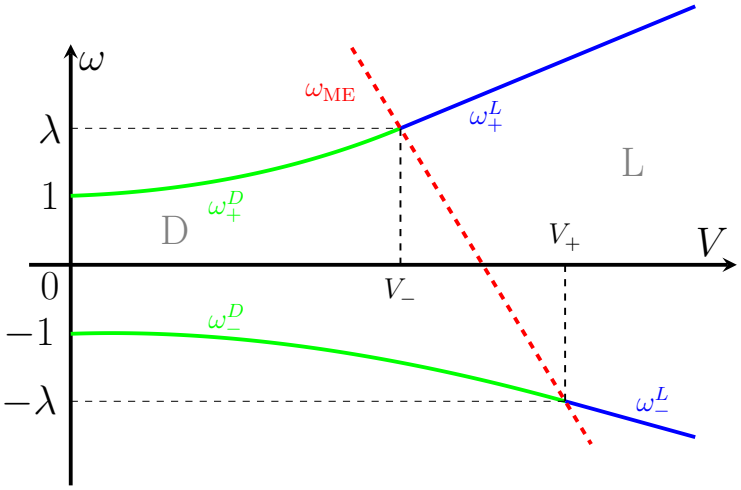


Figure 4.3: Schematic localisation phase diagram for the β model with $\beta = 0.2$. The locations of band edges are shown in green (delocalised) and blue (localised), and the mobility edge is shown as a dashed red line.

first-order theory is therefore not only successful for the simplest quasiperiodic model - the AAH model - but is capable also of capturing the more complicated behaviour present generically in models which are not fine-tuned to energy independence. In the next section, we repeat the above calculations for the mosaic model, which possesses the most intricate phenomenology of the three models studied here.

4.4.3 Mosaic model

The $l = 2$ mosaic model, like the β model, is constructed by modifying the AAH potential; in this case, by setting the site energy of every other site to zero. (For a discussion of arbitrary-l Mosaic models, see Sec. 3.3.3.) However, the qualitative behaviour which arises is significantly different from that in the β model. As seen previously in Fig. 3.4, the mosaic model possesses two mobility edges, which after entering the spectrum enclose a central band of delocalised states that persists to infinite potential strength. In what is perhaps the most surprising success of the first-order theory, both of these mobility edges are captured exactly, alongside the central delocalised band. For this model, we must consider the fact that there are two types of end site, which must be averaged over.

Localised phase

Computing the mean density of states in the localised phase (using Eq. 4.22) over ϕ and the two types of end site gives

$$\bar{D}(\omega) = \frac{1}{4\pi}\sum_{j_0=0}^{1}\int_0^{2\pi} \mathrm{d}\phi\ \delta(\omega - V\epsilon_{j_0}) = \frac{1}{2\pi\sqrt{V^2-\omega^2}} + \frac{1}{2}\delta(\omega). \tag{4.40}$$

The first part of the DoS arises from the site j_0 which has an AAH potential, and the delta function from the site which has no potential. At first sight the presence of a delta function $\delta(\omega)$ appears to be a strange result, as we know that analytically the states at $\omega = 0$ are always delocalised (and in fact we shall soon show that the mean-field theory correctly predicts the same result). However, as per the discussion in Sec. 4.3.5, $\bar{D}(\omega)$ can be understood as the large V limit of the density of states, for which Eq. 4.40 captures the correct behaviour. As half of the sites in the $l = 2$ Mosaic chain have no on-site potential, the density of states develops a peak at the band centre which becomes increasingly sharp as V is increased; in the $V \to \infty$ limit the peak is precisely a delta function containing half of the total number of eigenvalues. Another way to understand why the mean density of states takes the form in Eq. 4.40 is that the density of states is, at the level of the approximate first-order theory, *linear* in the different types of input end sites - each type of end site gives rise to a separate term in $\bar{D}(\omega)$. As far as estimating the density of states is concerned, the first-order theory in effect neglects hybridisation between sites.

The band edges of the localised phase are the same as the Aubry-André-Harper model; $\omega_{\pm}^{L} = \pm V$. Within these bounds, we search for solutions to Eq. 4.9 for the self-consistent y_{typ}, which for the mosaic model gives

$$\log\left(\frac{1+y_{\mathrm{typ}}}{y_{\mathrm{typ}}}\right) = \frac{1}{4\pi}\int_0^{2\pi}\mathrm{d}\phi\ \log(\omega - V\cos\phi)^2 + \log|\omega| \tag{4.41}$$

$$= \frac{1}{2}\log\left(\frac{V^2}{4}\right) + \log|\omega|, \tag{4.42}$$

where the integral computed is one half the integral I in Eq. 4.27, and is the contribution from those sites with an Aubry-André-Harper potential. This gives

$$y_{\mathrm{typ}} = \frac{2}{V|\omega| - 2}, \tag{4.43}$$

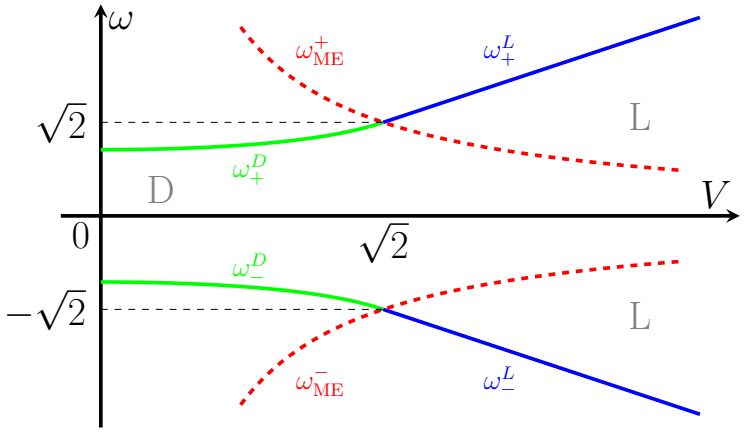


Figure 4.4: Schematic localisation phase diagram for the $l = 2$ mosaic model. The locations of band edges are shown in green (delocalised) and blue (localised), and the mobility edges are shown as dashed red lines.

from which follow the two mobility edges,

$$\omega^{\pm}_{\rm ME} = \pm\frac{2}{V}, \tag{4.44}$$

which is the exact result. Just as for the AAH and β models, $y_{\rm typ}$ diverges with unit exponent as the mobility edges are approached from the localised phase. The two mobility edges enter the band at $V = \sqrt{2}$, and do not leave thereafter. The first-order theory therefore recovers correctly a central band of delocalised states which persist for large values of V.

Delocalised phase

As we know from Sec. 4.3.3, the delocalised-side equation for $\Delta_{\rm typ}$ (Eq. 4.12) gives the same mobility edge condition as from the localised side. To locate the delocalised-side band edges shwon in Fig. 4.4, we consider the solutions to Eq. 4.12 with $\Delta_{\rm typ} = 0$ *outside* the general region in which localised states may exist ($-V < \omega < V$). This entails letting $|\omega| > |V|$ in Eq. 4.13, resulting in the equation

$$2\log|\omega| + \underbrace{\frac{1}{4\pi}\int_0^{2\pi} \mathrm{d}\phi\ \log\left(1 - \frac{V}{\omega}\cos\phi\right)^2}_{J} = 0, \tag{4.45}$$

with the integral J solved by substitution to give

$$J = \frac{1}{4\pi}\int_0^{2\pi} \mathrm{d}\phi\ \log\left(1 - \frac{V}{\omega}\cos\phi\right)^2 = \log\left|\frac{1}{2} + \frac{\sqrt{1-(V/\omega)^2}}{2}\right|, \tag{4.46}$$

for $|V/\omega| < 1$. From this,

$$\omega_{\pm} = \pm \frac{2}{\sqrt{4 - V^2}}, \tag{4.47}$$

for $V < \sqrt{2}$, thus defining the spectral band edges in the delocalised regime, as shown in Fig. 4.4. A full solution $\Delta_{\text{typ}}(V, \omega)$ has not been found, though Eq. 4.12 is soluble for $\omega = 0$, giving

$$\Delta_{\text{typ}}(\omega = 0) = \frac{2}{\sqrt{V^2 + 4}}, \tag{4.48}$$

which is finite for all V, indicating the presence of delocalised states exactly at the band centre for arbitrarily large V. These results are summarised in Fig. 4.4 as a localisation phase diagram for the model at first-order.

In the next section, we will complement our analysis of the β and mosaic models with numerical solutions to the mean-field equations for $\Delta_{\text{typ}}(V, \omega)$ and $y_{\text{typ}}(V, \omega)$ throughout the spectrum.

4.4.4 Numerical solutions to mean-field equations

The equations for y_{typ} (Eq. 4.9) and Δ_{typ} (Eq. 4.12) are not expected to yield analytic results for arbitrary quasiperiodic models. However, they are easily solved numerically. In Fig. 4.5 we plot numerical solutions to the β and mosaic models for $y_{\text{typ}}(\omega)$ and $\Delta_{\text{typ}}(\omega)$ at select values of V, alongside the band edges (grey lines) and mobility edges (red lines). In the next section, we will compare the analytic and numerical results obtained from the first-order theory to exact results, highlighting both the successes of the simple theory, as well as the features that it fails to capture.

4.4.5 Comparison to exact results

For the Aubry-André-Harper and $\ell = 2$ mosaic models, the first-order mobility edges are the exact mobility edges. For the β model, the exact result Eq. 3.9 is obtained as the limit $\beta \to 0$, and otherwise is approximately recovered. (Specifically, the gradient of the mobility edge is exactly recovered, and the intercept approximately.) For all three models, y_{typ} diverges as $y_{\text{typ}} \sim (\omega - \omega_{\text{ME}})^{-1}$ as the mobility edges are

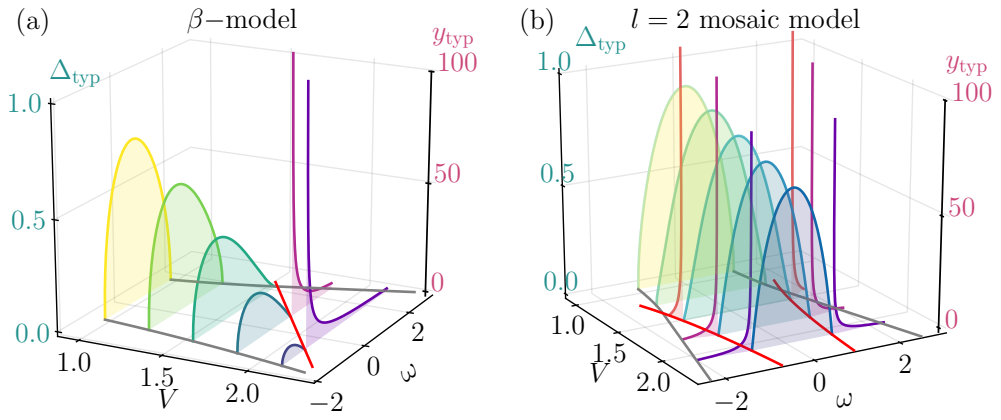


Figure 4.5: For the β model with $\beta = 0.2$, and $\ell = 2$ mosaic models, we plot $\Delta_{\text{typ}}(\omega)$ and $y_{\text{typ}}(\omega)$ for select values of V, obtained by solving the first-order equations 4.9 and 4.12 numerically. A finite value of $\Delta_{\text{typ}}(\omega)$ indicates the presence of delocalised states, and its vanishing that states, if present, are localised. Within the spectral band edges (grey curves in the (V, ω) plane), a finite value of $y_{\text{typ}}(\omega)$ implies that states are localised. The mobility edges of the models are plotted as red curves, at which $\Delta_{\text{typ}}(\omega)$ vanishes and $y_{\text{typ}}(\omega)$ diverges. $\Delta_{\text{typ}}(\omega)$ also vanishes on approach to the band edges.

approached from the localised side ($y_{\text{typ}} \sim (V-2)^{-1}$ as $V \to 2^+$ for the Aubry-André-Harper model). As the divergence of y_{typ} is proportional to the divergence of the localisation length of states, $\xi(\omega)$ (Sec. 2.2.4), the first-order theory theory predicts a critical exponent $\nu = 1$ for the divergence of ξ. This agrees with the exact results for the mosaic [22] and AAH [28] models, and appears to be a consequence of the structure of the first-order equations that is not destroyed by higher-order terms.

In the limit $V \to \infty$, the mean-field band edges are the exact band edges in all three models, and for all V the energy symmetry of the Aubry-André-Harper and mosaic models is recovered, and the energy *asymmetry* of the β model is recovered. (These energy (a)symmetries are clear in the exact numerical spectra in Fig. 3.4.) Furthermore, the approximate shape of the exact localisation phase diagrams (Fig. 3.4) is in all cases captured.

The most obvious feature missed by the first-order results is the presence of band-gaps in the spectrum. In Fig. 4.5, for example, the functions $\Delta_{\text{typ}}(\omega)$ are smooth curves, vanishing only at band edges and mobility edges. By contrast, the exact band structures in Fig. 3.4 feature hierarchical (fractal) gaps. From the structure of the underlying mean-field equation 4.4 it is obvious that such

gaps must be higher-order processes. The first-order theory takes as input the quasiperiodic potential on a single site, and as such does not capture effects which can be attributed to the infinite-range correlations between site energies.

In the next section, we compute from the first-order theory the distributions $P_\Delta(\Delta)$ and $P_y(y)$, of which Δ_{typ} and y_{typ} are the geometric means. Generally speaking, excellent agreement is found between the first-order distributions and numerically exact results. However, we shall also find that there are fine details present in the distributions which are missed at first order, and which may therefore be attributed to higher order processes. These observations motivate us in Chapter 5 to construct a more general framework for localisation in quasiperiodic chains, which takes into account the quasiperiodic potential on all sites simultaneously.

4.5 Distributions at first-order

In Sec. 4.3.4, general expressions for the distributions $P_\Delta(\Delta)$ (Eq. 4.15) and $P_y(y)$ (Eq. 4.17) were derived. Here, these equations are used to generate analytic results for all three models studied in this chapter. The process will be worked through in some detail for the Aubry-André-Harper model, after which we will present select results for the β and mosaic models, which are qualitatively similar. We will then compare the analytic results with exact numerical distributions, finding excellent agreement between the two. Analysis of the distributions reveals several seemingly universal features. In the localised phase, all distributions $P_y(y)$ feature power-law Lévy tails (as argued on general grounds in Sec. 4.3.4), as well as strict lower cut-offs which diverge as mobility edges are approached. In the delocalised phase, the distributions $P_\Delta(\Delta)$ feature both lower and upper cut-offs, which vanish and diverge respectively as mobility edges are approached.

4.5.1 Aubry-André-Harper model

Localised phase

At the band centre $\omega = 0$, the localised-side mean-field equation 4.7 reads,

$$y = \frac{1 + y_{\text{typ}}}{V^2 \epsilon(\phi)^2} = \frac{1}{(V^2 - 4)\cos^2(\phi)} \quad \Big(\equiv g(\phi) \Big), \tag{4.49}$$

and hence

$$y \geq \frac{1}{V^2 - 4} \quad \Big(\equiv a \Big). \tag{4.50}$$

As $V \to 2^+$, therefore, this lower bound diverges concomitantly with the divergence of y_{typ}. We note that the presence of such lower cut-offs is essentially obvious from Eq. 4.7 for y, in conjunction with the bounded nature of the potentials studied here. The AAH model has only one kind of end site, and hence Eq. 4.17 for $P_y(y)$ reads

$$P_y(y) = \frac{1}{2\pi} \int_0^{2\pi} \mathrm{d}\phi \; \delta(y - g(\phi)) = \frac{1}{2\pi} \sum_{\phi^*} \left| \frac{\partial g}{\partial \phi} \right|^{-1}_{\phi = \phi^*}, \tag{4.51}$$

where ϕ^* are the roots of the equation $y = g(\phi)$. As an illustration of this process, we plot in Fig. 4.6 $g(\phi)$ as a function of ϕ, showing that the equation $y = g(\phi)$ has four roots for $y > a$. Now, using $\partial g/\partial \phi = (\partial g/\partial \epsilon)(\partial \epsilon/\partial \phi)$,

$$\left| \frac{\partial g}{\partial \phi} \right|^{-1}_{\phi = \phi^*} = \frac{1}{2} y^{-3/2} \sqrt{\frac{1 + y_{\text{typ}}}{V^2 - V^2 \epsilon(\phi^*)^2}}, \tag{4.52}$$

and each of the four roots ϕ^* satisfies $V^2 \epsilon(\phi^*)^2 = (1 + y_{\text{typ}})/y$. We therefore arrive at

$$P_y(y) = \frac{1}{\pi} y^{-3/2} \sqrt{\frac{y}{\frac{y}{a} - 1}} \quad ; \quad y \geq a \equiv \frac{1}{V^2 - 4}, \tag{4.53}$$

which naturally satisfies $\log y_{\text{typ}} = \int_a^\infty \mathrm{d}y \;\; \log(y) \;\; P_y(y)$.

The simplicity of Eq. 4.53 is suggestive of a universal form for the localised phase, which may be obtained by letting $y = ax$, resulting in the band centre distribution

$$P_x(x) = \frac{1}{\pi} \frac{1}{x\sqrt{x - 1}} \quad ; \quad x \geq 1. \tag{4.54}$$

The localised phase is therefore characterised by a power law tail, $P_x(x) \overset{x \gg 1}{\approx} x^{-3/2}$, as expected from the discussion in Sec. 4.3.4.

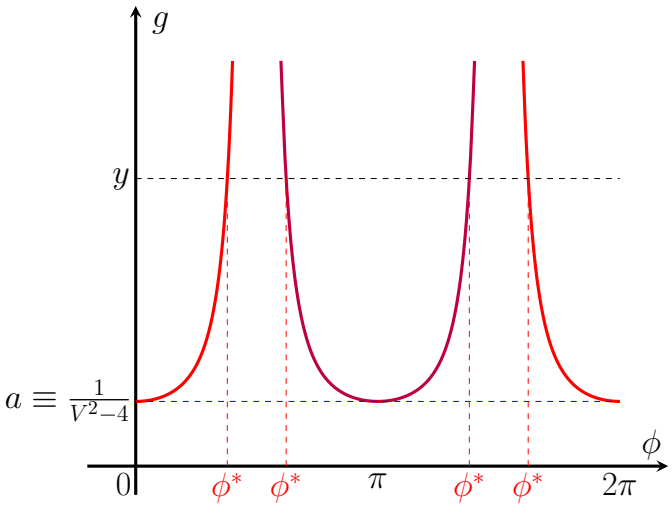


Figure 4.6: A plot of $g(\phi)$ against ϕ (Eq. 4.49), showing that the equation $y = g(\phi)$ has four roots for all $y > a$, where $a = (V^2 - 4)^{-1}$. Alternatively, this plot illustrates how y changes as the phase ϕ changes. By accumulating y over $\phi \in [0, 2\pi]$, we form the distribution $P_y(y)$. It is clear from this plot that $y > a$, and that y has no upper bound.

Distributions at finite ω (within the localised band edges) are obtained in exactly the same way, the only complication being that the roots ϕ^* are no longer four-fold degenerate over the whole range of y. Instead, the basic equation

$$y = \frac{1 + y_{\text{typ}}}{(\omega - \epsilon(\phi))^2}, \tag{4.55}$$

gives

$$P_y(y) = \frac{1}{4\pi} \sum_{\phi^*} \frac{y^{-3/2}\sqrt{1 + y_{\text{typ}}}}{\sqrt{V^2 - \epsilon(\phi^*)^2}}, \tag{4.56}$$

where

$$\epsilon(\phi^*) = \begin{cases} \omega - \sqrt{\frac{1+y_{\text{typ}}}{y}} & \equiv \quad R_- \qquad \text{if } \omega - \epsilon > 0 \\ \omega + \sqrt{\frac{1+y_{\text{typ}}}{y}} & \equiv \quad R_+ \qquad \text{if } \omega - \epsilon < 0 \end{cases}. \tag{4.57}$$

Depending on the value of y, one or both of these roots may exist for $\phi \in [0, 2\pi]$. The restriction that R_- corresponds to the domain in ϕ in which $\omega - \epsilon > 0$ translates to the restriction that $y \geq (1 + y_{\text{typ}})/(\omega + V)^2$. When this is true, the root occurs twice in the domain $\phi \in [0, 2\pi]$. Similarly, the fact that R_+ occurs for $\omega - \epsilon < 0$ gives a lower bound for R_+ of $(1 + y_{\text{typ}})/(\omega - V)^2$, with R_+ similarly occurring twice in this domain.

The distribution Eq. 4.56 is therefore the sum of two distinct components, with both roots from Eq. 4.57 used, and can be written as

$$P_y(y) = \sum_{\pm} P_{\pm} \quad \text{where} \quad P_{\pm} = \frac{1}{2\pi} y^{-3/2} \sqrt{\frac{y}{\frac{y}{a}\left(1 - \left(\frac{\omega}{V}\right)^2\right) \mp 2\frac{\omega}{V}\sqrt{\frac{y}{a}} - 1}}, \tag{4.58}$$

$$\text{domain}: \quad \frac{1 + y_{\text{typ}}}{(\omega \mp V)^2} \leq y \leq \infty \quad \text{for} \quad P_{\pm} \tag{4.59}$$

where $a = 1/(V^2 - 4)$ as before. Again, $\log(y_{\text{typ}}) = \int \mathrm{d}y \ \log(y) P_y(y)$, with the ω dependence of $P_y(y)$ somewhat remarkably cancelling out. When $\omega = 0$, the two roots in Eq. 4.57 and their domains are identical, and the band-centre distribution is returned. This distribution has two integrable singularities and a sharp lower cut-off which is in common with the band-centre result. We note that Eq. 4.58 can again be written in terms of $x = y/a$ in single-parameter scaling form, depending only on ω/V. At the band centre, this reduces to the universal distribution Eq. 4.54.

Delocalised phase

At the band centre $\omega = 0$, Eq. 4.10 reads

$$\Delta = \frac{\Delta_{\text{typ}}}{\epsilon(\phi)^2 + \Delta_{\text{typ}}^2} \quad \Big(\equiv h(\phi) \Big). \tag{4.60}$$

The minimum value $\epsilon(\phi)$ takes in the domain $\phi \in [0, 2\pi)$ is 0, and the maximum value is takes is V^2. This, coupled with the fact that Δ_{typ} is nonzero, implies that Eq. 4.60 has strict upper *and* lower cut-offs

$$\Big(b \equiv \Big) \quad \frac{\Delta_{\text{typ}}}{V^2 + \Delta_{\text{typ}}^2} \leq \Delta \leq \frac{1}{\Delta_{\text{typ}}}, \tag{4.61}$$

where Δ_{typ} is given by Eq. 4.29. From this, the delocalised-side distribution Eq. 4.15 gives

$$P_{\Delta}(\Delta) = \frac{1}{\pi\Delta} \frac{1}{\sqrt{1 - \Delta_{\text{typ}}\Delta}} \frac{1}{\sqrt{\Delta/b - 1}} \quad ; \quad b \leq \Delta \leq \frac{1}{\Delta_{\text{typ}}}, \tag{4.62}$$

with $\log \Delta_{\text{typ}} = \int_b^{\Delta_{\text{typ}}^{-1}} \mathrm{d}\Delta \ \log(\Delta) P_{\Delta}(\Delta)$. Results for finite ω can be obtained by the same process, though as in the localised phase the roots of Eq. 4.60 lose their degeneracy, resulting in an unwieldy distribution comprising two parts. As $V \to 2^-$,

$\Delta_{\text{typ}} \to 0$ and hence the domain encompasses all positive Δ; similarly, we note that the distributions in the two phases are, modulo a factor of η, *connected*. That is, $\eta P_y(y) = P_\Delta(\Delta)$ at $V = 2$. This is expected as $y \equiv \Delta/\eta$; $P_y(y)$ and $P_\Delta(\Delta)$ describe the same object. This result is straightforward to show analytically at the band centre from Eqs. 4.53 and 4.62.

4.5.2 β and Mosaic models

For the β and Mosaic models, the same process explained in some detail in the context of the AAH model can be used to generate analytic forms for the distributions $P_\Delta(\Delta)$ and $P_y(y)$. As the same essential qualitative features arise for all models, we present only select analytic results with a focus on the localised phase due to its apparent universality. Representative distributions for *all* models in both phases are plotted alongside numerical results in in Sec. 4.5.3.

β model

For the β-model, the distribution $P_y(y)$ acquires β-dependence, and naturally reduces to the Aubry-André-Harper result for $\beta = 0$. At the band centre, the effect of the additional parameter β is to split the distribution into two parts, $P_y(y) = P_y^+(y) + P_y^-(y)$, where

$$P_y^\pm(y) = \frac{y^{-3/2}}{2\pi} \frac{V\sqrt{1+y_{\text{typ}}}}{V \pm \beta\sqrt{\frac{1+y_{\text{typ}}}{y}}} \left\{ \left(V \pm \beta \sqrt{\frac{1+y_{\text{typ}}}{y}} \right)^2 - \frac{1+y_{\text{typ}}}{y} \right\}^{-1/2}, \tag{4.63}$$

with $y_{\text{typ}} = \lambda^2/[(\omega\beta + V)^2 - \lambda^2]$, and limits given by

$$\frac{1+y_{\text{typ}}}{V^2}(1 \mp \beta)^2 \leq y \leq \infty. \tag{4.64}$$

The presences of a lower cut-off and $\sim y^{-3/2}$ tail are unchanged from the AAH model. Likewise, the distributions $P_\Delta(\Delta)$ are formed of two parts at the band centre.

Mosaic model

For the mosaic model, there are two kinds of end sites: even-indexed sites, which have an AAH potential, and odd-indexed sites, which have zero potential. As for the AAH model, once again, $P_y(y) = P_y^{\pm}(y)$, where each term $P_y^{\pm}(y)$ is expressed as the sum of two terms,

$$P_y^{\pm}(y) = P_y^{\text{even},\pm} + P_y^{\text{odd},\pm}. \tag{4.65}$$

For odd sites, $\epsilon_{\text{odd}} = 0$ and hence

$$P_y^{\text{odd},\pm} = \frac{1}{4}\delta\left(y - \frac{1+y_{\text{typ}}}{\omega^2}\right), \tag{4.66}$$

where $y_{\text{typ}} = 2/(V|\omega| - 2)$. The zero-potential sites therefore contribute a delta-function spike to the distribution $P_y(y)$, with the position of the spike diverging as y_{typ} diverges on approach to a mobility edge.

The even sites have an Aubry-André-Harper potential, and hence $P_y^{\text{even},\pm}$ are given by one half of the AAH result Eq. 4.58:

$$P_y^{\text{even},\pm} = \frac{1}{4\pi} y^{-3/2} \sqrt{\frac{y}{\frac{y}{a}\left(1 - \left(\frac{\omega}{V}\right)^2\right) \mp 2\frac{\omega}{V}\sqrt{\frac{y}{a}} - 1}}, \tag{4.67}$$

with the distributions supported on $y \geq (1 + y_{\text{typ}})/(\omega \mp V)^2$. The distribution $P_\Delta(\Delta)$ likewise comprises an AAH term and a delta function term.

Like the density of states, the first-order expressions for $P_y(y)$ and $P_\Delta(\Delta)$ neglect hybridisation between the sites. However, this simple approximation captures well the *qualitative* features of the distributions in all cases. In the next section, we will compare directly the distributions in both phases with exact numerical results for all three models.

4.5.3 Comparison to numerical results

In Fig. 4.7 we plot the first-order distributions $P_\Delta(\Delta)$ and $P_y(y)$ for all three models alongside their numerical counterparts, for representative points in the (V, ω) plane. In the localised phase, excellent agreement is found. The $P_y(y) \sim y^{-3/2}$ Lévy tail -

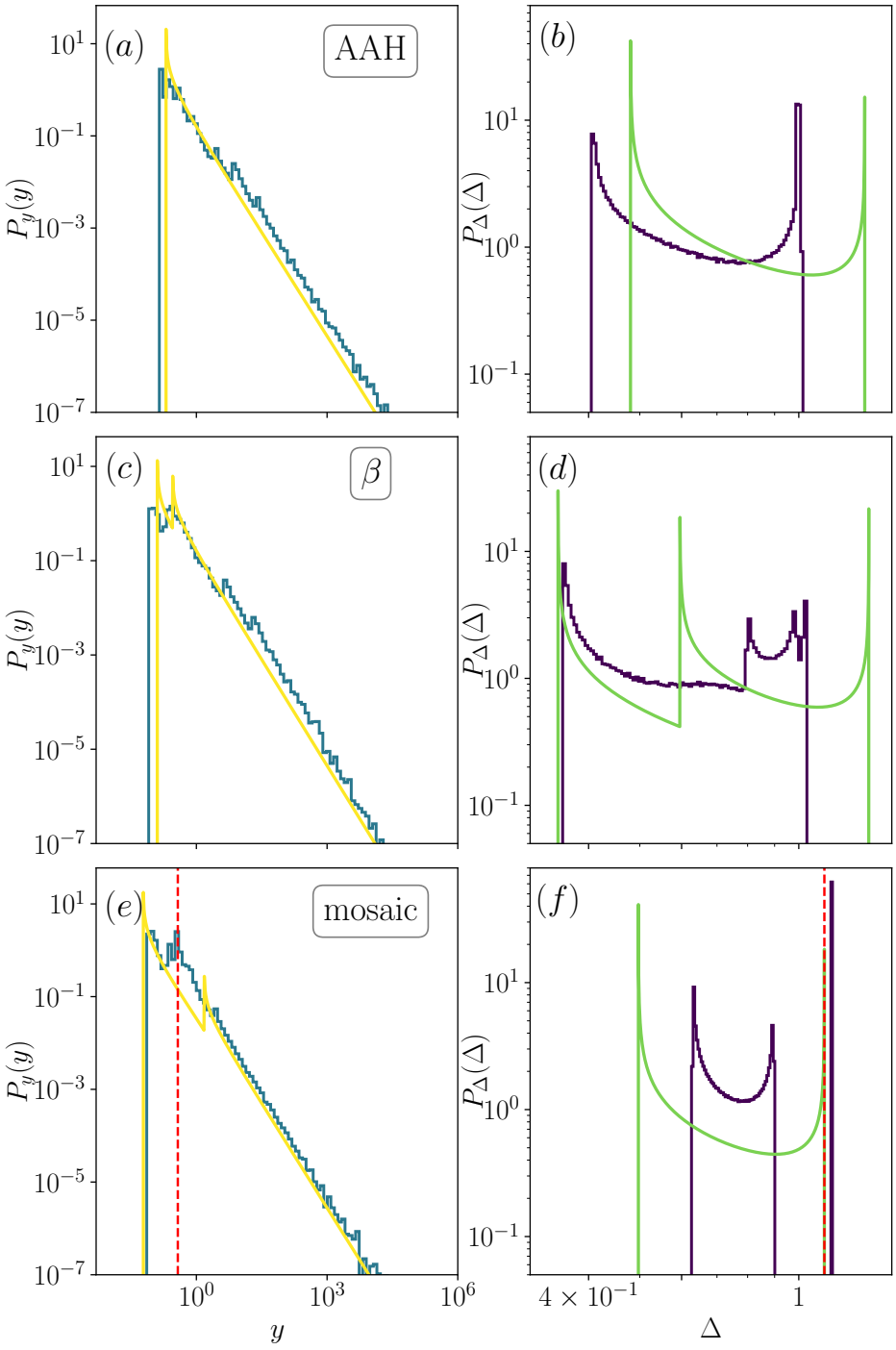


Figure 4.7: Distributions $P_y(y)$ and $P_\Delta(\Delta)$ for the AAH model [panels (a) and (b)], β model [panels (c) and (d)] and $l = 2$ mosaic model [panels (e) and (f)], from the first-order theory (yellow and green) and from exact diagonalisation (blue and purple). For the red dashed lines in the case of the mosaic model, see text. For all delocalised distributions $P_\Delta(\Delta)$, $V = 1$ and $\omega = 0$. For the localised distributions $P_y(y)$, $V = 3$, with $\omega = 0$ for the AAH and β models, and $\omega = 2$ for the mosaic model. Exact diagonalisation results are for a chain of length $L = 2000$, averaged over 2000 disorder realisations, and with $\eta = 4/L$.

present at first-order in all three models - is also found in the numerical distributions, along with the sharp lower cut-off. The theory captures the approximate locations of these cut-offs, as well as the peaks at low y, which are present as integrable singularities in the theory. In the delocalised phase, the most significant qualitative feature of the exact distributions is the presence of both lower and upper cut-offs, which is captured by the theory, along with the approximate shapes and locations of the distributions.

The expression for the AAH distribution $P_y(y)$ (Eq. 4.53 at $\omega = 0$) consists of a single peak and a Lévy tail. Numerically, this same structure is found, though with the addition of *fine structure* atop the power-law tail that is missed at first-order. This detail can be attributed to the infinite-range correlations present in the model, as it is not washed away by ϕ-averaging. The β model distribution (Eq. 4.63 at $\omega = 0$) consists of two parts, and hence has two integrable singularities at low y. In the corresponding numerical data, two peaks at low y can indeed be seen. In the mosaic model, a delta-function peak is also present in $P_y(y)$ (shown as a red dashed line); this peak is aligned with a peak in the numerical distribution. Both the β and mosaic models also have fine structure atop their tails that is not captured by the theory. In order to recover this fine detail, longer-ranged correlations between site energies must be incorporated into the theory; this necessitates going to higher order in the RPS for the self energy, and is one of the topics of Chapter. 5.

Turning now to the delocalised phase, the qualitative features of the numerical distributions are well-captured at first-order. For the AAH model, the mean-field $P_\Delta(\Delta)$ (Eq. 4.62) consists of a skewed curve bounded by two integrable singularities; aside from an overall re-scaling of the distribution, the numerical results are qualitatively the same. For the β model, the distribution consists in both cases of two nested curves, each with the same approximate shape as the AAH distribution. For the mosaic model, the distribution $P_y(y)$ consists of an AAH part and a delta function component (shown as a red dashed line), the latter of which is attributed to the sites which have zero potential. In the numerical data, the same behaviour is seen.

Despite its simplicity, the first-order theory captures the important qualitative features of the self energy distributions for three diverse quasiperiodic models. This result makes a case for the universality of the mean-field approach, and its utility in performing approximate calculations for new models. In the next section, we will summarise our findings and provide motivation for the analysis carried in out Chapter 5.

4.6 Conclusion

In summary, we have introduced a simple approximate theory for localisation in quasiperiodic models with nearest-neighbour hopping. The theory is constructed within the framework of the renormalised perturbation series for the local self energy, which after being truncated at first-order is evaluated self-consistently. Such an approach has its antecedents in the self-consistent theory of localisation by Abou-Chacra, Anderson and Thouless [34], and enables localisation phase diagrams to be mapped out for arbitrary models. The theory was tested with three diverse models, and despite its simplicity was shown to reproduce the important qualitative features of each. Surprisingly, for both the Aubry-André-Harper and $l = 2$ mosaic models, the locations of the mobility edges were recovered exactly.

At the same time, the results of this chapter raised a number of important questions. We found that certain higher-order processes, such as the presence of fractal bandgaps in the spectra of the models, and fine details in the self energy distributions, were missed by the first-order description. An obvious question, therefore, is whether these features are recovered by extending the theory to higher orders.

As discussed in Sec. 2.1.6, the self energy S_0 (for the end site 0 of a semi-infinite half chain) may be iterated to an order $\ell > 1$, which includes explicitly the site energies $\epsilon_1, \epsilon_2, \ldots, \epsilon_\ell$. Progressively longer-ranged correlations between the sites are thereby incorporated as ℓ is increased. Higher-order self-consistent theories may then be implemented by replacing $S_\ell \to -i\Delta_{\text{typ}}$ (see Sec. 2.2.5 for discussion). We hypothesise that these higher-order theories capture with greater quantitative

accuracy objects such as the self energy distributions. In a similar spirit, we ask: what happens to the theories as the order of evaluation is taken to infinity? To answer this question, the convergence properties of the self energy must be evaluated in continued fraction form, in an approach that bears resemblance to Anderson's original work [4]. Generalising the results of this chapter to higher order, analysing the convergence properties of the self energy, and connecting these approaches both conceptually and mathematically, forms the basis of Chapter 5.

5

Higher-order theories and the continued fraction

Contents

5.1 Introduction 79
5.2 The continued fraction 80
5.2.1 Localised phase 82
5.3 Convergence of the continued fraction 83
5.4 Self-consistent theory at arbitrary order 86
5.4.1 Self-consistent equations 87
5.4.2 Convergence of self-consistent theories 88
5.5 Self energy distributions 91
5.5.1 End-site spectra 94
5.6 Discussion 94

"But there is a very important fundamental truth about random systems we must always keep in mind: no real atom is an average atom, nor is an experiment ever done on an ensemble of samples. What we really need to know is the probability distribution of [Im S] not its average, because it's only each specific instance we are interested in. I would like to emphasize that this is the important, and deeply new, step taken here: the willingness to deal with distributions, not averages."

— P. W. Anderson, Nobel Prize lecture, 1977

5.1 Introduction

In the previous chapter, a leading-order theory for mobility edges and localisation phase diagrams in quasiperiodic models was constructed. The theory was based on a self-consistent analysis of the local propagator, in particular the imaginary part of the associated self energy, using a renormalised perturbation series (RPS). The first-order theory was shown to give analytical access to mobility edges, spectral band edges and localisation length critical exponents, with very good agreement with exact results. However, the theory was approximate in nature, taking as input the quasiperiodic potential on only one site. This was most obviously evident in the theory missing certain higher-order processes, such as the presence of fractal band gaps in the spectra and finer details in the distributions of self energies.

These observations prompted significant conceptual questions. Prime among them is whether the theory is robust to the addition of higher order terms. One may express the root-site self energy S_0 in terms of the self energy S_ℓ of any site, and with the replacement $S_\ell \to -i\Delta_{\text{typ}}$ construct an ℓ-th order self-consistent theory. Does carrying out this process at increasingly high orders produce more quantitatively accurate results, and recover what was missed at first order? Answering these questions necessarily involves going beyond the leading-order treatment, and evaluating the RPS at higher orders, such that the deterministic potential is accounted for on many sites simultaneously. Finally, we will be interested in the fate of higher-order theories as the order of evaluation is taken to infinity, in particular whether results become exact in this limit.

In order to answer these questions, we first use the RPS to represent the self energy as a continued fraction, and study its convergence, or lack thereof, in both phases. This treatment is closer in spirit to Anderson's original work [4] than subsequent self-consistent theories. The continued fraction at order ℓ includes contributions from all site energies within a distance ℓ of the root site, and is obtained by setting $S_\ell = 0$. Physically, this criterion is equivalent to cutting the chain between sites ℓ and $\ell + 1$, and 'convergence' is achieved if such a cut does not affect the root site. By taking into account the correlated potential on many

sites, higher-order processes are recovered, including the presence of spectral band gaps that were missed by the first-order theory.

Alongside analysing the bare CF, we also truncate it at arbitrary orders and impose self-consistency. This procedure allows us to analyse the convergence of the self-consistent theories with ℓ. In practice, both approaches yield quantitatively the same results for the localisation phase diagram, as well as very good agreement with the first-order theory. This makes a case for the robustness of the first-order theory: for all models tested, its qualitative predictions are unchanged upon going to higher orders.

5.2 The continued fraction

As in the previous chapter, we begin with the result that the Green function $G_0(\omega)$ for the end-site of a semi-infinite half chain can be written in terms of the self energy $S_1(\omega)$ of the adjacent site (with site 0 removed), as $G_0(\omega) = (\omega + i\eta - V\epsilon_1 - S_0(\omega))^{-1}$, where $S_0 = J^2 G_1(\omega)$. The recursive structure of these equations allows us to write $G_0(\omega)$ as a continued fraction,

$$G_0(\omega) = \cfrac{1}{\omega + i\eta - V\epsilon_0 - \cfrac{J^2}{\omega + i\eta - V\epsilon_1 - \cfrac{J^2}{\ddots}}}, \tag{5.1}$$

such that the self energy $S_0(\omega)$ is also given by a continued fraction,

$$S_0(\omega) = \cfrac{J^2}{\omega + i\eta - V\epsilon_1 - \cfrac{J^2}{\omega + i\eta - V\epsilon_2 - \cfrac{J^2}{\ddots}}}. \tag{5.2}$$

These continued fractions continue *ad infinitum* and as such are exact; they include the energies of all sites, which is important for quasiperiodic models as the site-energy correlations have infinite range.

The convergence of Eqs. 5.1 and 5.2 may be studied directly (and numerically). Alternatively, we can express $\Delta_0 = -\mathrm{Im}S_0$ as an infinite series, from which it is

easy to take the relevant limits for the localised and delocalised phases. Using $S_1 \equiv X_1 - i\Delta_1$, we first rationalise the expression for S_0, giving Δ_0 as

$$\Delta_0 = \frac{J^2(\eta + \Delta_1)}{(\omega - V\epsilon_1 - X_1)^2 + (\eta + \Delta_1)^2}. \tag{5.3}$$

This equation may be iterated to give

$$\Delta_0 = \sum_{n=1}^{\infty} \Delta_0(n) \quad \text{with} \quad \Delta_0(n) \equiv \eta \prod_{k=1}^{n} \frac{J^2}{\Omega_k^2}, \tag{5.4}$$

where

$$\Omega_k^2 = (\omega - V\epsilon_k - X_k)^2 + (\eta + \Delta_k)^2. \tag{5.5}$$

Though Eq. 5.4 appears simple, it is in fact highly complex due to the dependence of Ω_k on on X_k and Δ_k, which themselves have corresponding CF/series representations. For X_0, in fact, a similar recursion gives

$$X_0 = \sum_{n=1}^{\infty} X_0(n) \quad \text{where} \quad X_0(n) = (-1)^{n+1}(\omega - V\epsilon_n) \prod_{k=1}^{n} \frac{J^2}{\Omega_k^2}, \tag{5.6}$$

with similar complexity arising due to the Ω_ks. $S_0 = X_0 - i\Delta_0$ may therefore be written as a series, albeit one with a nested structure, where the denominators contain series of a similar form. Physically, the renormalised perturbation series casts the self energy as a sum over all paths that leave the root site 0, go out to a site n, and then return to the root site. $\Delta_0(n)$ is the contribution to Δ_0 of such a path. The fact that the theory is exactly renormalised is reflected by the full inclusion of the Δ_ks and X_ks in the denominators Ω_k^2.

Lastly, we introduce the following notation

$$S_0^{[\ell]} = \cfrac{J^2}{\omega + i\eta - V\epsilon_1 - \cfrac{J^2}{\omega + i\eta - V\epsilon_2 - \cfrac{J^2}{\ddots \cfrac{J^2}{\omega + i\eta - V\epsilon_\ell - S_\ell}}}}. \tag{5.7}$$

$S_0^{[\ell]}$ is exactly Eq. 5.2, but iterated to level ℓ and written as an explicit function of S_ℓ; this latter self energy itself admits a continued fraction representation, and contains the dependence of $S_0^{[\ell]}$ on the rest of the chain. The notation will be

useful when we implement ℓ-th order mean-field theories, as we do so with the replacement $S_\ell \to -i\Delta_{\text{typ}}$. It allows us to define truncation at order ℓ as setting $S_\ell = 0$; physically, this is equivalent to cutting the J-bond between sites ℓ and $\ell+1$.

We now conclude this section by turning to the localised phase, in which the CF and its associated series representations simplify greatly.

5.2.1 Localised phase

In the localised phase, we may take the limit $\Delta_0 \sim \eta \to 0^+$, reducing Eq. 5.4 to

$$y_0 = \sum_{n=1}^{\infty} y_0(n) \quad \text{with} \quad y_0(n) \equiv \prod_{k=1}^{n} \frac{J^2}{\tilde{\Omega}_k^2}, \tag{5.8}$$

where

$$\tilde{\Omega}_k = (\omega - V\epsilon_k - X_k). \tag{5.9}$$

y_0 therefore includes exactly the contributions from the real parts of the self energy, X_k, which in the localised phase each have continued fraction representation,

$$X_k = \cfrac{J^2}{\omega - V\epsilon_{k+1} - \cfrac{J^2}{\omega - V\epsilon_{k+2} - \cfrac{J^2}{\ddots}}}, \tag{5.10}$$

and have no dependence on Δ_k. In the localised phase, therefore, $\tilde{\Omega}_k$ is related to $\tilde{\Omega}_{k+1}$ by the recursion relation

$$\tilde{\Omega}_k = \omega - V\epsilon_k - J^2/\tilde{\Omega}_{k+1}, \tag{5.11}$$

and truncation of Eq. 5.8 by setting $S_\ell = 0$ gives the boundary conditions

$$X_{\ell-1} = \frac{J^2}{\omega - V\epsilon_\ell} \quad \text{and} \quad \tilde{\Omega}_\ell = \omega - V\epsilon_\ell. \tag{5.12}$$

Crucially, none of equations 5.8-5.12 are dependent on η, and as such all are defined *directly* in the thermodynamic limit. This is in contrast to the series for Δ_0 in the delocalised phase (Eq. 5.4), which when evaluated numerically must be done so with a finite value of η, meaning that all such calculations are strictly speaking performed for finite systems. In the localised phase, the convergence of y_0 can be

analysed for an infinite system. This is the first significant result of this chapter. Having now established the basic equations for the CF representation of the self energy, we turn to an analysis of its convergence properties.

5.3 Convergence of the continued fraction

In this section, we explore the link between the convergence of the continued fraction equations and the underlying localisation properties of the two phases. We begin with Eq. 5.4 for Δ_0. As mentioned before, this equation can only be computed for finite-size systems due to its explicit dependence on η. With $\eta \sim \mathcal{O}(L^{-1})$ (as in exact diagonalisation calculations), Δ_0 truncated at order $\ell = L$ is exact for a finite chain of length L. The same is true for the CF (Eq. 5.7) for S_0.

By sampling Eq. 5.4 over may ϕ-values, one can compute the geometric mean Δ_{typ}. In Fig. 5.1 we plot Δ_{typ} as a function of L for the AAH and Mosaic models (results for the β model are qualitatively similar) at various points in the (V, ω) plane. In the localised phase, we find that $\Delta_{\text{typ}} \sim L^{-1}$ decays to zero as L is increased, implying that $y_{\text{typ}} \sim L\Delta_{\text{typ}}$ is finite. This is just as expected physically in the localised phase, $\Delta_{\text{typ}} \propto \eta \propto 1/L$. In the delocalised phase, Δ_{typ} is by contrast finite as $L \to \infty$, again as expected physically. Precisely *at* the transition, $\Delta_{\text{typ}} \sim L^{-\alpha}$ with $\alpha < 1$, reflecting the multifractal nature of the critical eigenstates. We note at this stage that these results are exactly the same as those obtained in Sec. 4.2.1 by exact diagonalisation.

In the localised phase, we utilise the series form of y_0 (Eq. 5.8). As the limit $\eta \to 0$ has been taken, Eq. 5.8 is valid for a thermodynamically large system. Denoting $y_0^{[\ell]} = \sum_{n=1}^{\ell} y_0(n)$, we study the convergence properties of this partial sum as a function of ℓ. Where localised states are present at a particular point in the (V, ω) plane, $y_0^{[\ell]}$ will admit a finite saturation value upon increasing ℓ; where delocalised states are present, it will diverge as $\ell \to \infty$ as the framework itself breaks down. In Fig. 5.2 we plot the typical values $y_{\text{typ}}^{[\ell]}$ as functions of ℓ at various points in the localisation phase diagrams of the three models. Saturation to finite values of y_{typ} is found in the localised phase of each model. We also observe that the

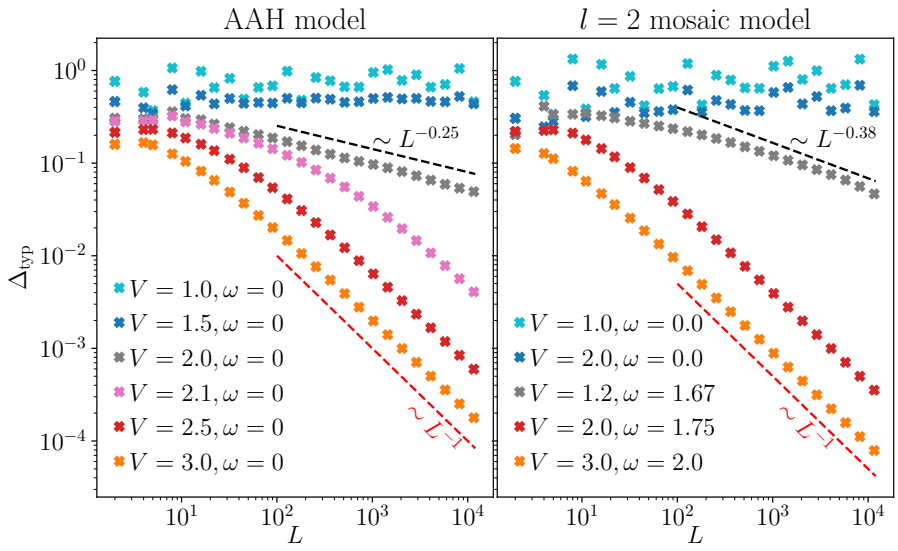


Figure 5.1: Plots of the L-dependence of Δ_{typ} obtained from the exact series for Δ_0 (Eq. 5.4), with $\ell = L - 1$, for a system with L sites, for the AAH and mosaic models. Data in orange/red/pink correspond to points in the localised phases of the models, in which $\Delta_{\text{typ}} \sim L^{-1}$ for sufficiently large L. On the other hand, data in blue/cyan correspond to the delocalised phases, in which Δ_{typ} is finite as $L \to \infty$. Data in grey correspond to points in the (V, ω) plane at criticality, and as such $\Delta_{\text{typ}} \sim L^{-\alpha}$ decays to zero with an anomalous exponent, reflecting the multifractal nature of the critical eigenstates. These exponents are indicated on the graph by means of straight dashed lines which serve as a guide to the eye. All data points are formed by sampling Eq. 5.4 over 5000 values of $\phi \in [0, 2\pi)$.

saturation value, as well as the length scale at which saturation occurs, grows as the mobility edges are approached. This is a consequence of the fact that the localisation length of the underlying states grows with proximity to the critical points.

The fact that the saturation value y_{typ} grows with the localisation length of states was demonstrated in Sec. 2.2.4, in which we showed that $y_0(\omega) \sim \xi$ for $\xi \gg 1$, where ξ is the localisation length of a state of energy ω centred on the root site of the chain. y_{typ} therefore diverges with the same critical exponent ($\nu = 1$) as the localisation length on approaching a delocalisation transition.

Employing the same physical reasoning, we can also understand why the order ℓ of convergence increases as the transition is approached. $y_0(n)$ in Eq. 5.8 is the contribution to y_0 of a path which goes out to site n and then back to the root site. Such a process is sketched in Fig. 5.3, atop an exponentially decaying localised state. For all $n \gg \xi$, the contributions for such processes are evidently negligible.

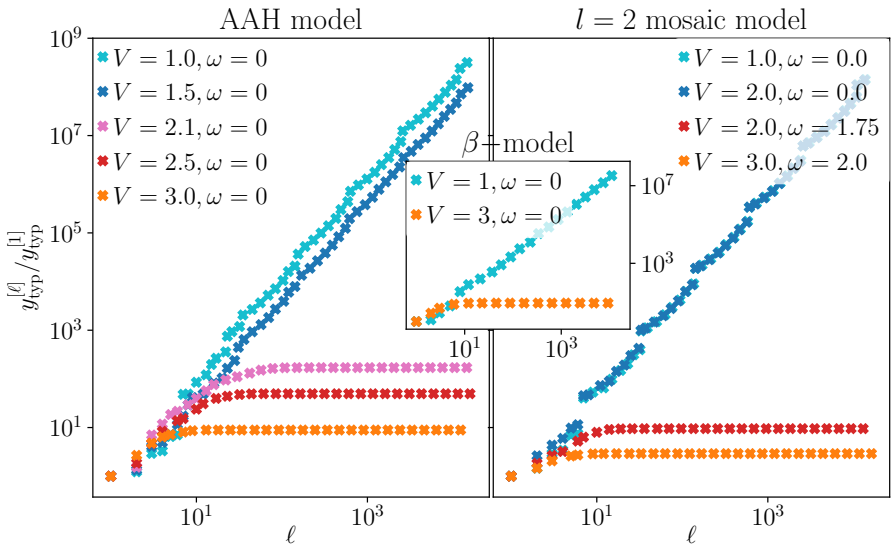


Figure 5.2: Results for $y^{[\ell]}_{\text{typ}}$ against ℓ, obtained by sampling the series in Eq. 5.8 over 5000 values of ϕ, for all three models. In the localised phases, $y^{[\ell]}_{\text{typ}}$ saturates at a finite value of ℓ, with both the saturation value and the order at which saturation occurs increasing as the mobility edges are approached and the localisation length of the underlying states diverges. In the delocalised phases, the framework itself breaks down, and $y^{[\ell]}_{\text{typ}}$ diverges as $\ell \to \infty$.

Alternatively, one could say that the self energy of the root site is insensitive to cutting the chain at order ℓ, provided that $\ell \gg \xi$. Indeed, this latter criterion could be taken as the definition of a localised phase.

As the transition is approached and the localisation length ξ diverges, so too does y_{typ} and the order ℓ at which the series in Eq. 5.8 converges. In the delocalised phase, the framework itself breaks down (as the limit $\eta \to 0$, which we took in deriving Eq. 5.8, is no longer appropriate), which is reflected in the divergence everywhere of $y^{[\ell]}_{\text{typ}}$ as $\ell \to \infty$.

In this section, we have analysed the convergence properties of the self energy by truncating its CF (Eq. 5.7) and series (Eqs. 5.4 and 5.8) representations at different orders ℓ by setting $S_\ell \to 0$. This is equivalent to cutting the chain a distance ℓ away from the root site, and asking: Is there an order ℓ after which cutting the chain does not affect the root site? We found that the answer to this question is always *yes* in the localised phase, with the critical ℓ being of the order of the localisation length ξ of states which overlap the root site. The alternative approach to truncating the

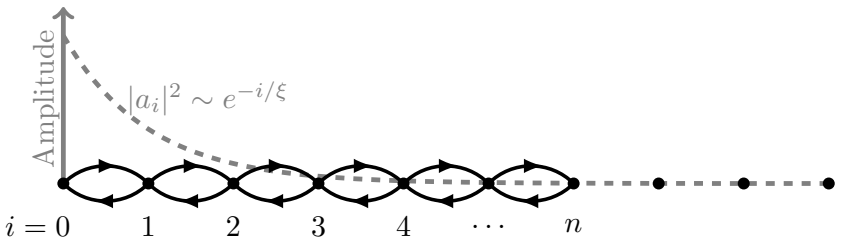


Figure 5.3: A schematic diagram of the contribution $y_0(n)$ to y_0 (Eq. 5.8). Also shown is a localised state centred on the root site. As the localisation length ξ of this state is less than the order n of the path, we expect $y_0(n)$ to be small.

CF is to replace $S_\ell \to -i\Delta_{\text{typ}}$, and solving the resultant equations self-consistently. Such an approach constitutes a mean-field theory at order ℓ, and in the next section we study the convergence properties of these theories as ℓ is increased.

5.4 Self-consistent theory at arbitrary order

In this section, we focus on arbitrary-order mean-field theories, which are constructed at an order ℓ by endowing the terminal self energy with a typical imaginary part: $S_\ell \to -i\Delta_{\text{typ}}$. Self-consistency is then imposed by requiring that the typical value of Δ_0 be equal to the input Δ_{typ},

$$\exp\langle\langle \log \Delta_0 \rangle\rangle = \Delta_{\text{typ}}, \tag{5.13}$$

where $\langle\langle \ldots \rangle\rangle$ denotes an average over ϕ and different types of end-site. The structure of the resultant equations will incorporate all the quasiperiodic site energies upto site ℓ, with the rest of the chain parametrised through Δ_{typ}. The convergence properties of this self-consistent Δ_{typ} can then be studied as a function of the order ℓ.

In Chapter 4 the self-consistent theory at first order $\ell = 1$ was analysed in detail, and analytic expressions for the mobility edges, spectral band edges and functional forms of $\Delta_{\text{typ}}/y_{\text{typ}}$ obtained. For all three models detailed in Sec. 3.3, very good agreement between the first-order theory and exact (where available) and numerical results was found. In this chapter, our focus will be on the higher-order theories, with the self-consistent equations for Δ_{typ} and y_{typ} solved numerically. In particular, we will examine how the higher-order theories' convergence properties

are dictated by the convergence of the underlying CF. We begin by deriving the mean-field equations at arbitrary order ℓ.

5.4.1 Self-consistent equations

Arbitrary-order mean-field equations are readily generated from the series in Eqs. 5.4 and 5.8 as,

$$\begin{aligned} \Delta_0 &= \Delta_0^{[\ell-1]} + \Delta_0(\ell)(1+\Delta_{\text{typ}}/\eta) \\ y_0 &= y_0^{[\ell-1]} + y_0(\ell)(1+y_{\text{typ}}) \end{aligned} . \tag{5.14}$$

As before, $\Delta_0^{[\ell-1]}$ is the sum of terms upto order $\ell-1$ that contribute to Δ_0, and the terminal factor of $(1+\Delta_{\text{typ}}/\eta)$ results from the mean-field replacement $S_\ell \to -i\Delta_{\text{typ}}$. Self-consistency is then imposed as

$$\log \Delta_{\text{typ}} = \langle\langle \log \Delta_0 \rangle\rangle \quad \text{and} \quad \log y_{\text{typ}} = \langle\langle \log y_0 \rangle\rangle. \tag{5.15}$$

Equivalently, self-consistency can be imposed through the distribution $P_\Delta(\Delta)$ as $\log \Delta_{\text{typ}} = \int \mathrm{d}\Delta \; P_\Delta(\Delta) \log \Delta$, where

$$P_\Delta(\Delta) = \langle\langle \delta(\Delta - \Delta_0) \rangle\rangle, \tag{5.16}$$

and similarly for $P_y(y)$. Through Eq. 5.14, $P_\Delta(\Delta)$ and $P_y(y)$ depend parametrically on the input Δ_{typ} or y_{typ}.

At any order, self-consistent solutions in the localised and delocalised phases must give the same result for the locations of mobility edges. To see this, note that as a localisation critical point is approached from the delocalised side, $\Delta_0 \to 0$, such that $\Omega_k \to (\omega - V\epsilon_k - X_k)$. In this limit, the two equations in Eq. 5.14 reduce to the same equation. The connected nature of the two phases also manifests in the distributions $P_\Delta(\Delta)$ and $P_y(y)$, which after a trivial rescaling by η are identical at the critical points. $P_\Delta(\Delta)$ is therefore smoothly connected to $P_y(y)$ in the localised phase. This result was shown explicitly at first order for the AAH model in Sec. 4.5.

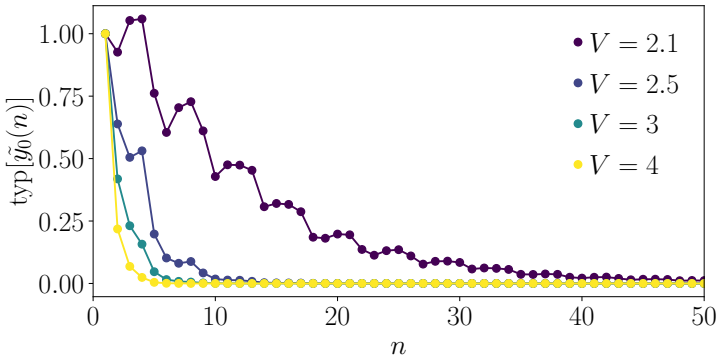


Figure 5.4: For the Aubry-André-Harper model, we plot the typical values of the terms $\tilde{y_0}(n) \equiv y_0(n)/y_0(1)$ for different values of V (as indicated in the figure), for $\ell = 200$. For $n \gtrsim \xi$, where ξ is the localisation length of the states, these terms decay to zero. All datapoints averaged over 5000 ϕ values.

5.4.2 Convergence of self-consistent theories

In this section, we first establish the connection between the convergence of the CF and of the self-consistent Δ_{typ} and y_{typ}. In the delocalised phase, convergence of the series for Δ_0 is possible only if the terms $\Delta_0(n) \geq 0$ decay to zero sufficiently rapidly with increasing n. It must therefore be the case that $\Delta_0(n) \to 0$ as $n \to \infty$, implying that the term $\Delta_0(\ell)(1 + \Delta_{\text{typ}}/\eta) \to 0$ too. As $n \to \infty$, the self-consistent Δ_{typ} is therefore equal to that obtained from the bare series in Eq. 5.4.

In the localised phase, convergence of the series for y_0 after a finite number of terms ℓ (where $\ell \gtrsim \xi$) implies that $y_0(n) \to 0$ for $n \gtrsim \xi$. This is illustrated in Fig. 5.4 for the AAH model. The same argument as above then applies: the effect of capping $y_0(\ell)$ with $(1 + y_{\text{typ}})$ is negligible, provided $\ell \gg \xi$. The self-consistent y_{typ} is therefore identical to the value obtained from the series alone, provided the series has converged.

For sufficiently large ℓ, the higher-order mean-field theories therefore converge to the continued fraction results. However, there is a qualitative difference between the processes in the delocalised and localised phases. The series in Eq. 5.8 for y_0 is evaluated in the thermodynamic limit, and as such when it converges, it does so to the exact thermodynamic result. A key advantage of the series representation is that deep in the localised phase (where ξ is small), this convergence may occur after an $\mathcal{O}(1)$ number of terms. From the perspective of the self-consistent theories, this

result implies that low-order theories are sufficient to achieve quantitative accuracy and recover what was missed at first-order. This will be evident in Sec. 5.5 when we compare the distributions $P_y(y)$ at different orders to the numerical result. This result generalises the observation in Chapter 4 that the first-order theory becomes increasingly accurate the deeper in the localised phase one uses it.

In the delocalised phase, by contrast, the series and hence also the mean-field theories are defined for finite-size systems of length L, where $\eta \sim L^{-1}$. Per the above argument, the two approaches necessarily converge to the same result, and that result is the same as would be obtained by exact diagonalisation of a system of size $L = \ell$. However, the localisation length $\xi \propto L$ in the delocalised phase. In contrast to the localised phase, one must therefore go to very large values of L to obtain thermodynamic results. This is evident in Fig. 5.1, where deep in the delocalised phase of the AAH model, convergence of Δ_{typ} has not been achieved by $L = 10000$. The very nature of the delocalised phase makes it more susceptible to finite-size effects, as the delocalised nature of the states implies a sensitivity to boundary conditions.

Returning now to the localised phase, we confirm the mutual convergence of the self-consistent and continued fraction results for y_{typ} in Fig. 5.5. There, we evaluate numerically the difference $\delta y^{[\ell]}_{\text{typ}}$ between the two approaches as a function of the order ℓ, finding that the relative error $\delta y^{[\ell]}_{\text{typ}}/y^{[\ell]}_{\text{typ}}$ decays to zero exponentially rapidly in ℓ for all three models. We also plot the raw data $y^{[\ell]}_{\text{typ}}$ against ℓ, showing the rapid convergence of both approaches to the thermodynamic y_{typ}. As discussed, this convergence occurs at an order ℓ controlled by the localisation length of the eigenstates at the point of evaluation in the (ω, V) plane. As discussed in Sec. 5.3, when a critical point is approached from the localised phase, the divergence of the localisation length implies a concomitant divergence of the order required to achieve convergence. This is confirmed by the left sub-panel in Fig. 5.5, which shows the average ℓ required to achieve convergence to a given tolerance as a function of $(V - V_c)$ for the AAH model. For sufficiently small tolerances, the required

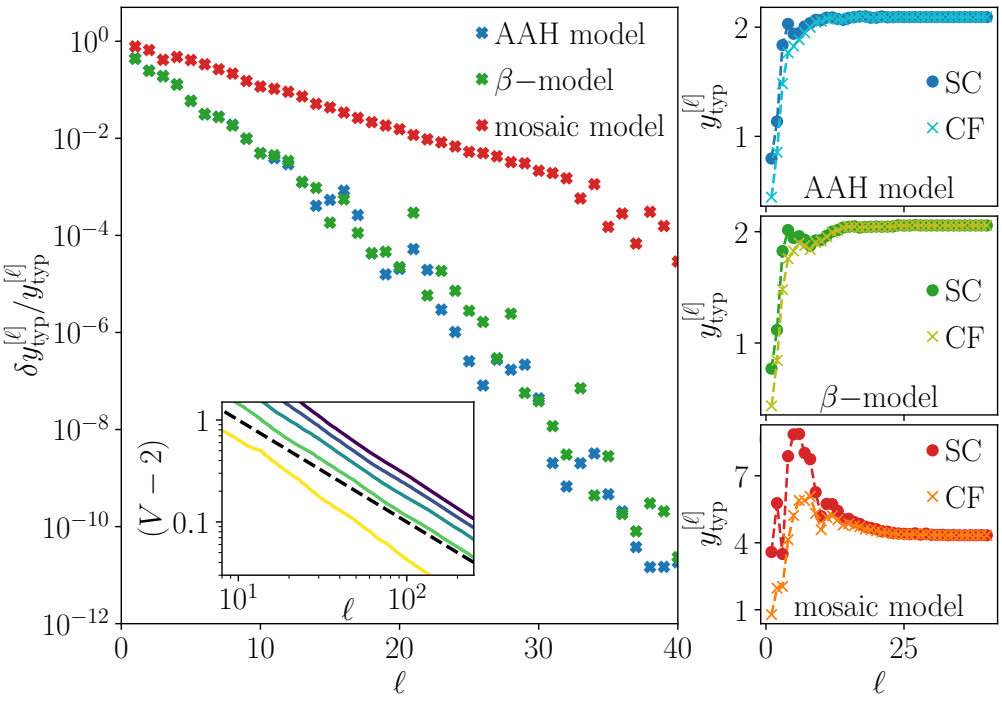


Figure 5.5: Plots demonstrating the convergence of the self-consistent (SC) and continued fraction (CF) results for $y_{\rm typ}$ to the same value with increasing order ℓ in the localised regimes of all three models. *Left-hand panel:* A plot of $\delta y_{\rm typ}^{[\ell]}/y_{\rm typ}^{[\ell]}$ against ℓ for all three models, where $\delta y_{\rm typ}^{[\ell]} = y_{\rm typ}^{[\ell],\rm SC} - y_{\rm typ}^{[\ell],\rm CF}$. This quantitiy is necessarily positive. The plot is log-linear, demonstrating that $\delta y_{\rm typ}^{[\ell]}$ decays exponentially with ℓ. Results are at the band centre $\omega = 0$ with $V = 3$ for the AAH and $\beta = 0.2$ models, and for $\omega = 1.5$ and $V = 1.7$ for the mosaic model. Convergence is in practice achieved at $\ell \sim \mathcal{O}(10)$. The inset panel shows the mean value of ℓ required to achieve convergence in the CF to within a given tolerance. The different coloured lines correspond to $\delta y_{\rm typ}^{[\ell],\rm CF} = 10^{-2}, 10^{-4}, 10^{-6}, 10^{-8}$ and 10^{-10} from yellow to purple, where $\delta y_{\rm typ}^{[\ell],\rm CF} = y_{\rm typ}^{[\ell+1],\rm CF} - y_{\rm typ}^{[\ell],\rm CF}$. The black dashed line denotes $(V - V_c)^{-1}$. *Right-hand panels*: Plots of $y_{\rm typ}^{[\ell],\rm CF}$ alongside $y_{\rm typ}^{[\ell],\rm SC}$ demonstrating directly their convergence with increasing ℓ to a common thermodynamic limit $y_{\rm typ}$.

$\ell \sim (V - V_c)^{-1}$ diverges with exponent 1; this is, as expected, the same exponent as that with which the localisation length diverges.

In the next section, we will use both the continued fraction and the self-consistent theory to compute self energy distributions and the end-site density of states. From the discussion in this section, we expect that both approaches will give the same results, and furthermore that convergence in the localised phase to the exact result will be rapid.

5.5 Self energy distributions

When we studied the first-order theory in Chapter 4, a particular focus was given to the distributions of Δ_0 and y_0, as conjugate probabilistic order parameters for localisation transitions. In the localised phase, the overall agreement of the self-consistent distributions $P_y(y)$ with numerical results was excellent. In particular, the $\sim y^{-3/2}$ Lévy tail emerged as a seemingly universal feature of the localised phase. While the distributions $P_\Delta(\Delta)$ were less quantitatively accurate - capturing only approximately the locations and shapes of the numerical distributions - the presence of hard cut-offs in the numerical data was correctly predicted, along with other, model-specific features.

However, in the localised phase, the numerical distributions have additional fine structures which reside on top of the Lévy tails, and which are not captured by the first-order theory. These structures are not washed away by ϕ-averaging, and hence can be attributed to deterministic ("infinite-range correlated") nature of the quasiperiodic potentials. In this section, we will focus on the recovery of these fine structures at higher order in the theory, and the convergence of mean-field results to the exact numerical results.

In Fig. 5.6 distributions $P_y(y)$ for various orders ℓ alongside exact numerical results for all three models. The first-order ($\ell = 1$) theory predicts a smooth $\sim y^{-3/2}$ Lévy tail in each case, missing all other detail. As the higher-order theories explicitly take into account the potential on all sites upto the order of truncation, we expect the finer structures to reveal themselves as ℓ is increased. As seen in Fig. 5.6, this is indeed the case. At second-order ($\ell = 2$), select features begin to emerge atop the Lévy tail, and by $\ell = 20$, the self-consistent and numerical distributions are hardly distinguishable. In order to quantify the convergence of the self-consistent distributions to the ED results, we compute the Kullback-Leibler (KL) divergence [160],

$$D_{\mathrm{KL}}(\ell) = \int \mathrm{d}y \; P_y^{\mathrm{ED}}(y) \log\left(\frac{P_y^{\mathrm{ED}}(y)}{P_y^{[\ell]}(y)}\right), \tag{5.17}$$

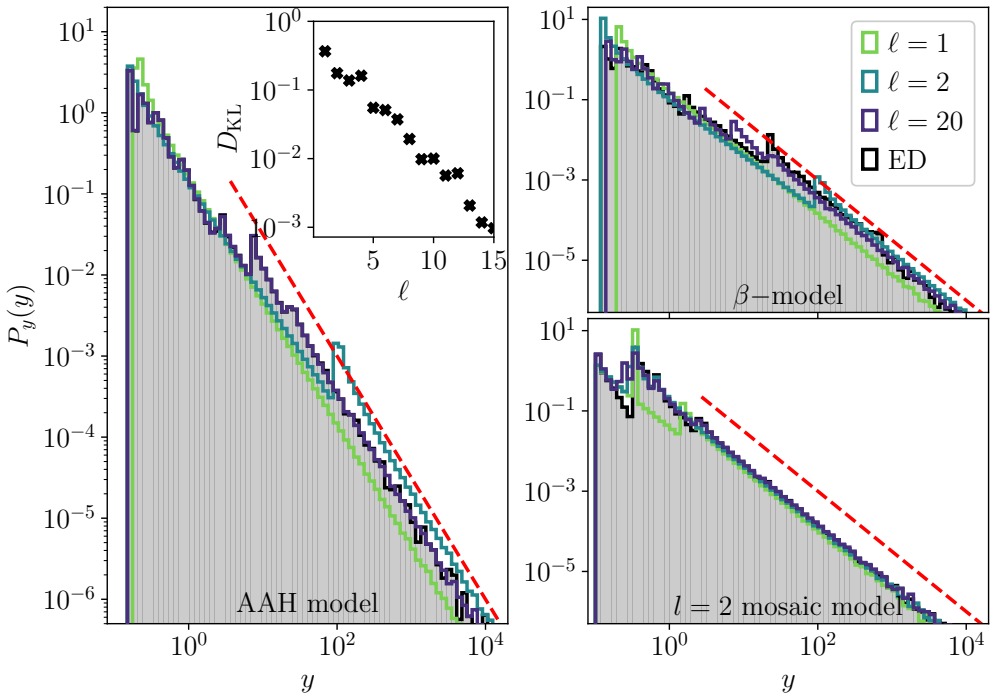


Figure 5.6: For the AAH, β, and mosaic models, distributions $P_y(y)$ obtained from the self-consistent (SC) theory at different orders ℓ are plotted alongside exact results obtained by the exact diagonalisation (ED) of systems of length $L = 5000$ (black curves with grey shading). Results are presented for $\ell = 1, 2$ and 20. In each case, a $\sim y^{-3/2}$ Lévy tail is present, with additional structures becoming apparent with increasing ℓ. The $\ell = 20$ SC distributions are barely distinguishable from the ED distributions. Results are shown for $V = 3$ in all cases, with $\omega = 0$ for the AAH and $\beta = 0.2$ models, and $\omega = 2$ for the mosaic model. *Inset panel:* The Kullback-Leibler divergence D_{KL} between the SC and ED distributions as a function of ℓ for the AAH model. D_{KL} decays exponentially with ℓ, demonstrating the rapid convergence of the SC distributions to the exact result.

where $P_y^{[\ell]}$ is the ℓ-th order self-consistent distribution. The KL divergence is a measure of statistical distance between two probability distributions, and a value of $D_{\mathrm{KL}} = 0$ implies that the distributions are identical. As shown in the inset panel of Fig. 5.6, D_{KL} decays to zero exponentially rapidly in ℓ.

This rapid convergence is due to the convergence properties of the underlying CF in the localised phase. As per the discussion in Sec. 5.4.2, as the localisation length ξ increases in the vicinity of a critical point, higher orders of theory will be necessary to recover the exact distributions. On the other hand, deep in the localised phase where $\xi \sim \mathcal{O}(1)$, low-order theories will be sufficient. Where the mean-field theories have converged, the CF must necessarily also have converged - and hence either approach can be used in practice to generate exact distributions.

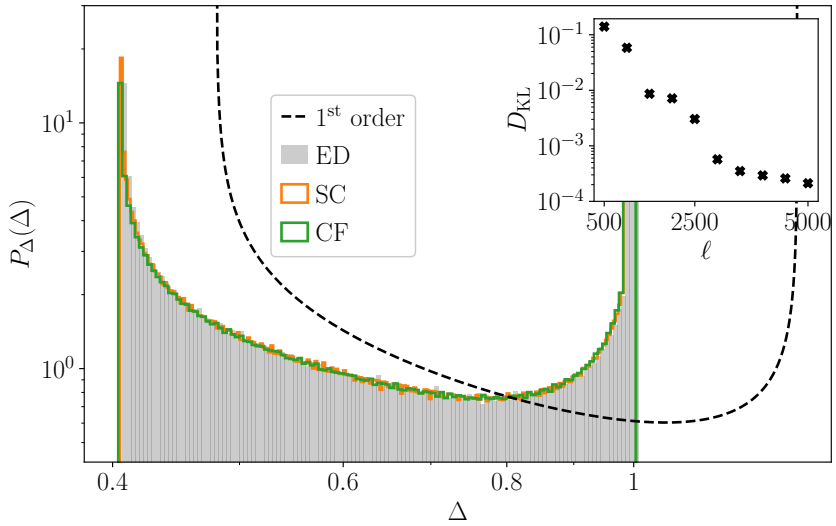


Figure 5.7: Distributions $P_\Delta(\Delta)$ computed from the continued fraction (CF), self-consistent theory (SC) and numerical exact diagonalisation (ED), for the AAH model in the delocalised phase ($V = 1$, $\omega = 0$). Both CF and SC distributions are for $\ell = 5000$, and the ED distribution for $L = 5000$; excellent quantitative agreement between all three is seen. Also shown is the first-order SC result (dashed black line), which captures only approximately the shape and location of the exact distribution. The inset panel shows the Kullback-Leibler divergence D_{KL} between the SC distributions at different orders ℓ, and the ED distribution with $L = 5000$. The decay of D_{KL} to zero as ℓ increases quantifies the increasing accuracy of the self-consistent theories as the order is increased.

In the delocalised phase, rapid, ξ-controlled convergence does not occur. Rather, An ℓ-th order theory recovers the ED result for a system of size $L = \ell$. In Fig. 5.7, we plot distributions $P_\Delta(\Delta)$ for the AAH model obtained from the truncated CF, and from the self-consistent theory, at order $\ell = 5000$. Alongside, we show the equivalent distribution obtained from ED; the three plots are barely distinguishable. For reference, the first-order analytic result is shown; while the overall shape and skew of the distributions is captured at first order, quantitative accuracy is not obtained. The inset panel to Fig. 5.7 shows the Kullback-Leibler divergence D_{KL} between the self-consistent distributions at various orders ℓ, and the reference ED distribution with $L = 5000$. D_{KL} naturally decays with ℓ; however, as expected this decay is much slower than in the localised phase (Fig. 5.6).

Lastly, a qualitative feature of quasiperiodic models that is missed entirely by the first-order theory is the presence of fractal bandgaps in the eigenspectra. In the next section, we demonstrate that going to higher orders (in both the CF

and self-consistent theories) recovers this structure; and that such bandgaps are therefore attributable to long-ranged correlations in the potentials [153].

5.5.1 End-site spectra

The first-order theory gives results for the mean and typical densities of states, using which one can map out the localisation phase diagrams of arbitrary quasiperiodic models. In Chapter 4 we showed that these results capture important qualitative features of the exact phase diagrams. However, the bands predicted by the first-order theory are smooth and feature no gaps - failing to capture the hierarchical structure intrinsic to quasiperiodic systems. (Numerical spectra are plotted in Fig 3.4.) These structures are again attributable to the correlated nature of the potentials, as ϕ-averaging does not wash them away [153]. We therefore expect that as the order of CF or SC theory is increased, the bandgaps will begin to reveal themselves. Before presenting results however, we note the following. We define the bandgaps of each model as those regions of the spectra where no states are present for an infinite system. For finite-size systems, however, we find numerically that a small number of states are present in these regions. In particular, these states are found to reside on the end sites of the chain, such that the *end-site* density of states has a small, but finite, proportion of states present in the 'gaps'.

With this in mind, we plot in Fig. 6.4 the average local density of states (LDoS) for the root site of the AAH model. Results are shown for the continued fraction approach at increasing order ℓ, and are compared to the ED result. At first-order ($\ell = 1$), the mean LDoS is a smooth curve, and fails to capture any of the structure of the peaks and troughs in the ED spectrum, which reflect the bands and gaps in the total DoS. Peaks begin to appear as ℓ is increased, and by $\ell = 32$ convergence with respect to the (numerically exact) ED result is achieved.

5.6 Discussion

In this chapter, we have presented a theoretical framework for understanding localisation in nearest-neighbour quasiperiodic chains. The theory is based on the

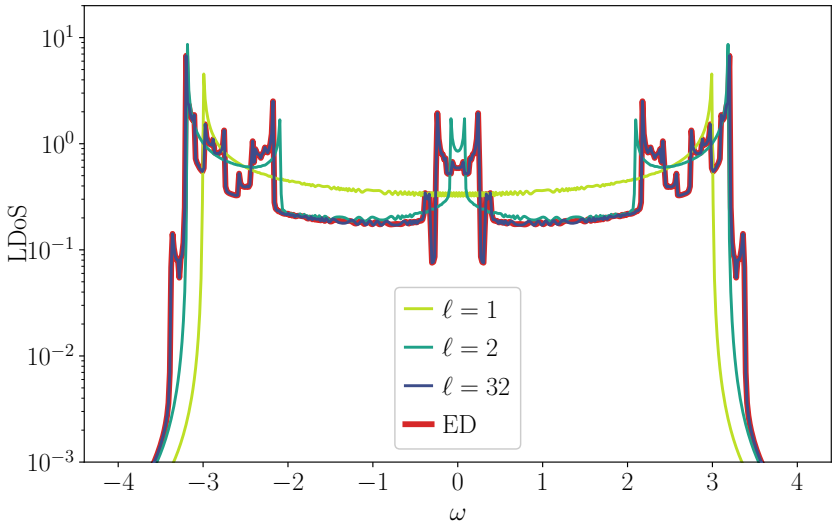


Figure 5.8: The mean local density of states (LDoS) for the root site of the AAH model with $V = 3$. Results are obtained from the continued fraction at $\ell = 1, 2$ and 32, and are plotted alongside the ED spectrum for a system of length $L = 1024$. Though the nested structure of peaks and troughs is not captured at first order, the $\ell = 32$ theory is well-converged to the ED result.

continued fraction (CF) representation of local propagators and their associated self energies, in particular for the root site of a semi-infinite half chain. Our main focus was on the imaginary part of the end-site self energy, Δ_0, which is a probabilistic order parameter for localisation; its typical value $\Delta_{\text{typ}}(\omega)$ converges to a finite value in the delocalised phase, and decays to zero in the localised phase as the order of evaluation is increased. Defining the conjugate order parameter $y_0 \equiv \Delta_0/\eta$, its typical value y_{typ} by contrast converges to a finite value in the localised phase and diverges in the extended phase. By analysing the convergence properties of these two order parameters as the energy and Hamiltonian parameters are changed, therefore, one can map out the localisation phase diagrams and associated mobility edges of arbitrary models.

Higher-order self-consistent theories were also studied, and their convergence properties shown to be intimately related to those of the underlying CF. In the limit of infinite order, it was shown that the two approaches are asymptotically equivalent, and furthermore agree quantitatively with exact numerical results. In going to higher orders in the theory, fine structures in the distributions of y were recovered, which we attribute to the strong correlations present in quasiperiodic potentials. Similarly, we

found that the hierarchical band gaps present in the disorder-averaged spectrum are progressively resolved with increasing order. These structures appear in addition to universal features such as the presence of a power-law Lévy tail in the distributions of y in the localised regime. Though the sub-structures were missed by the first-order theory, the universal features were well-captured, and the essential qualitative predictions of the theory remain unchanged at higher order. This makes a case for the robustness of the leading-order treatment to the addition of higher-order terms.

A physical connection between the convergence properties of the CF and the localisation length of the underlying states was made. Focussing on regions of the phase diagrams where states are localised with characteristic length ξ, we first showed that y_0 can be represented as a sum of paths which go out a distance ℓ from the root site and then back again. Crucially, we demonstrated that those paths for which $\ell \gtrapprox \xi$ make a negligible contribution to the self energy. Deep in the localised phase, therefore, y_0 converges rapidly, with the precise order of convergence controlled by the localisation length. As the mobility edges are approached, and the localisation length diverges, so too does the order of theory required to achieve convergence. Such rapid convergence does not occur in the delocalised phase. There, results obtained from the CF at ℓ-th order are the same as those obtained by the exact diagonalisation of a system of size $L = \ell$.

In the CF approach, truncation at order ℓ was achieved by setting $S_\ell \to 0$. In the self-consistent approach, on the other hand, $S_\ell \to -i\Delta_{\text{typ}}$ was set to a typical value. Accompanying both approaches was the use of a regulator η, by which the energy ω is given an infinitesimal imaginary component: $\omega \to \omega + i\eta$. We mention here another method which has been used to study disordered systems, in which a regulator is not used, and self-consistency is not imposed [161–163]. Though quite different, the approach has a similar spirit in that one seeds the imaginary part of the terminal self energy with $S_\ell \to -i$, which corresponds to attaching the terminal site of the chain to a conducting lead. Focussing on the imaginary part Δ_0 that is induced on the root site, the two phases may be distinguished. In the localised

regime, the imaginary part in S_ℓ does not propagate to the root site, such that $\Delta_0 \to 0$ for $\ell \gg \xi$; in the extended regime, a non-vanishing Δ_0 is induced.

6

The maximally-correlated chain

Contents

6.1 Introduction 98
6.2 Maximally correlated chain 101
6.2.1 Statistics of the maximally correlated chain 105
6.3 Extended, multifractal and mixed phases 107
6.3.1 Distribution of tabletop lengths 108
6.3.2 Generalised inverse participation ratios 113
6.3.3 The transfer matrix 114
6.4 Dynamics of the maximally correlated chain 116
6.4.1 A heuristic picture 119
6.5 Discussion 120

6.1 Introduction

Multifractal wavefunctions are beautiful electronic states that are neither fully extended in space nor fully localised. Characterised by the statistics of their amplitudes, they are described by an infinite set of fractal dimensions. For a wavefunction $\psi(x)$,

$$\sum_{x=1}^{L} |\psi(x)|^{2q} \sim \begin{cases} L^{-(q-1)} & : \text{extended} \\ L^{-D_q(q-1)} & : \text{(multi)fractal} \\ L^0 & : \text{localised} \end{cases}, \tag{6.1}$$

where $0 < D_q < 1$ is the fractal dimension [5], and q is a real number. If D_q is a constant with no q dependence, $D_q \equiv D$, then the wavefunction is a standard fractal. For a multifractal state, however, D_q is a nontrivial function of q. Multifractal wavefunctions therefore have associated with them an infinite set of exponents, describing how powers of the wavefunction scale. If $q > 1$, for instance, then the wavefunction is suppressed more on sites where it has a low amplitude, leading in effect to the peaks of the wavefunction being enhanced. Conversely, a value of $q < 1$ leads to a relative enhancement of the wavefunction on sites where it has a lower amplitude, in effect suppressing the peaks. If changing the value of q, and hence the relative enhancement or suppression of the peaks, changes the exponent with which the wavefunction scales, then its statistics are multifractal. Multifractal wavefunctions are sometimes called 'extended non-ergodic' wavefunctions [140, 164, 165], as they have weight on a diverging number of lattice sites in the thermodynamic limit, but a vanishing fraction of the total number.

In short-ranged disordered models in finite dimensions, multifractal wavefunctions are often present at critical points such as Anderson transitions [5, 47, 51, 166–171], mobility edges [172, 173], and quantum Hall plateau transitions [52, 174, 175]. Being associated with critical points, however, these multifractal states are *fine-tuned*. In the case of mobility edges in quasiperiodic models, for example, a small change to either the energy or the potential strength will move the model into either the localised or delocalised phase, destroying the multifractal wavefunction (see Sec. 3.1).

Robust multifractality can be realised in several ways. It is for example present in several long-ranged disordered-hopping models, and in fully-connected random-matrix ensembles [24, 140, 164, 176–178]. An interesting question thus arises: is it possible to realise a robust multifractal phase in a short-ranged disordered quantum system in low dimensions? One such avenue was proposed in Ref [53], in a manifestly out-of-equilibrium setting. The authors considered a periodically driven (Floquet) quasiperiodic chain, and demonstrated that a robust band of



Figure 6.1: A schematic diagram of the three regimes of the maximally correlated chain as a function of disorder strength (for Hamiltonian Eq. 6.2 with correlations given by Eq. 6.4). For sufficiently strong disorder, all states are multifractal, and for sufficiently weak disorder all states are by contrast extended. In between these two phases is a mixed regime, in which some realisations host multifractal states and some extended.

multifractal states arises through the coupling of extended and localised states (at different energies) in the presence of a mobility edge.

In this chapter, an alternative pathway to robust multifractality in one-dimensional short-ranged systems is taken, importantly in a time-independent Hamiltonian setting. We show that the presence of *maximal* correlations [29, 30] between the sites of a disordered chain leads to a robust multifractal phase for sufficiently strong disorder. These correlations are such that any two sites separated by a finite or sub-extensive distance have a statistical correlation of one in the thermodynamic limit [29, 30], and therefore take the same value. For small disorder strengths, we find that suppression of site-energy fluctuations leads to a delocalised phase, and between the two phases is a mixed regime, in which some disorder realisations host extended eigenstates and some multifractal. A schematic of the resultant phase diagram, as a function of disorder strength, is shown in Fig. 6.1.

These results are in stark contrast to uncorrelated Anderson models in one dimension [37, 39]. Furthermore, the multifractal states present in this model are markedly different from conventional multifractal states. Rather than having a self-similar peak structure and long polynomial tails of wavefunction amplitudes [47, 51], the multifractal states are tabletop-like, being approximately constant over a continuous segment ℓ of the chain and zero elsewhere. Multifractality is embodied both in the scaling of the wavefunction moments (Eq. 6.1), and in the anomalous scaling of the tabletop lengths ℓ with system size. For example tabletop states, see Fig. 6.2.

We begin this chapter with a detailed discussion of the model in Sec. 6.2, and of the statistics of the correlations in Sec. 6.2.1. We will demonstrate that the strong

correlations induce strong realisation-to-realisation fluctuations in the density of states: this is the origin of the mixed region of multifractal and extended states.

Our numerical analysis begins in Sec. 6.3, where we provide detailed evidence for the presence of extended, multifractal and mixed regimes. We begin with an analysis of the distributions of tabletop lengths ℓ, before focussing on the scaling of wavefunction moments, as in Eq. 6.1. Lastly, we perform a transfer matrix calculation, demonstrating how the conductance properties of the chain can be used to distinguish the three regimes.

In Sec. 6.4 we examine the consequences of the 'anomalous' nature of the multifractal states on the dynamical properties of the system. Multifractal states are commonly associated with subdiffusive transport [53, 125, 179, 180]; here, by contrast, a localised wavepacket prepared in the multifractal phase initially spreads ballistically, before saturating to a value that scales non-trivially with system size. We close with a discussion in Sec. 6.5.

6.2 Maximally correlated chain

As a concrete model consider a one-dimensional tight-binding chain of length L, described by the Hamiltonian

$$H = W \sum_{x=1}^{L} \epsilon_x |x\rangle\langle x| + t \sum_{x=1}^{L-1} \{|x\rangle\langle x+1| + |x+1\rangle\langle x|\}\,, \tag{6.2}$$

where W is the strength of the on-site potential, the form of which is encoded in the variables $\{\epsilon_x\}$. From here on, we set the hopping strength t to 1 without loss of generality. If $\{\epsilon_x\}$ are chosen to be independent random variables, then Eq. 6.2 describes a $1d$ Anderson system, with all eigenstates localised for all $W > 0$ [37, 39].

Arbitrary correlations between the site energies may be imposed by drawing the site energies from a multivariate Gaussian with zero mean: $\vec{\boldsymbol{\epsilon}} \sim \mathcal{N}(\mathbf{0}, \Sigma)$, where $\vec{\boldsymbol{\epsilon}} = (\epsilon_1, \epsilon_2, \ldots, \epsilon_L)^T$ is a vector of site energies, and Σ the covariance matrix with elements $\Sigma_{xy} = \langle \epsilon_x \epsilon_y \rangle$, where $\langle \ldots \rangle$ represents a disorder average. The $1d$

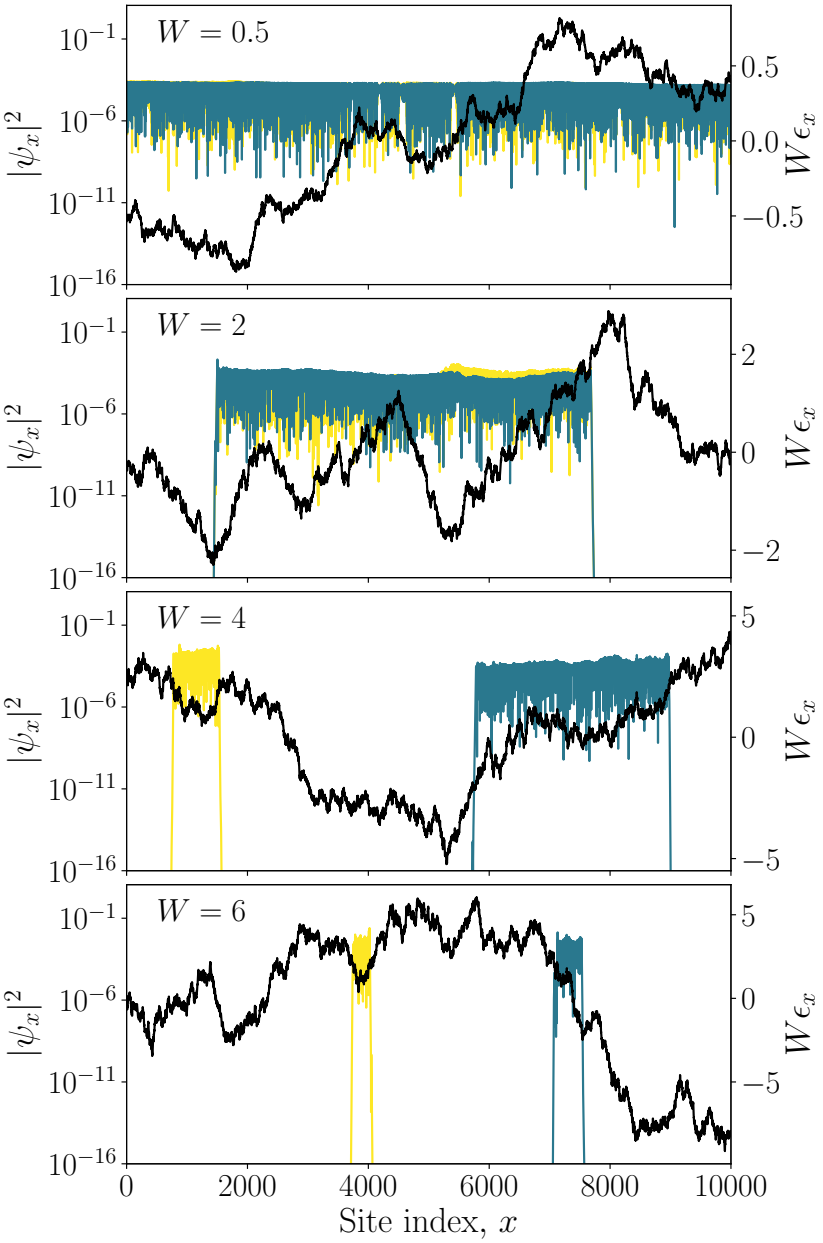


Figure 6.2: For $W = 0.5$ (delocalised phase), $W = 2$ (mixed region) and $W = 4, 6$ (multifractal phase) we plot two eigenstates (in blue and yellow) alongside the correlated potential in black. All eigenstates are tabletop-like, being approximately constant over some region of the lattice before vanishing. In the delocalised phase, the eigenstates saturate the phase, whereas in the multifractal regime they are sub-extensive. The system size $L = 10000$, and the eigenstates are extracted from the band centre $\omega = 0$ of $\mathcal{H}$ (Eq. 6.7).

Anderson system would be described by $[\Sigma]_{xy} = \delta_{x,y}$. For example, if we consider the correlations in the potential to decay with distance as

$$\Sigma(r) \equiv [\Sigma]_{x,x+r} = a^r \quad : \quad |a| < 1, \tag{6.3}$$

then trivial delocalisation corresponds to $a = 1$, and for constant $a \in [0, 1)$, Anderson localisation is expected[1]. Our focus here by contrast is on the case of *maximal* correlations mentioned in the introduction, for which we take Σ to depend only on r/L,

$$\Sigma(r) = f(r/L) \quad \text{where} \quad \lim_{y\to 0} f(y) = 1. \tag{6.4}$$

This functional form is motivated by the correlations in Fock space which are necessary to stabilise a many-body localised phase. In Ref. [29], the function f was shown for p-local Hamiltonians to be a p-th order polynomial in $r/\log N_{\mathcal{H}}$, where $N_{\mathcal{H}}$ is the Fock-space dimension. $N_{\mathcal{H}}$ scales exponentially with L, thereby recovering the dependence of $\Sigma(r)$ on r/L.

Eq. 6.4 may be realised with different functions $f(y)$, with the same qualitative behaviour arising in each case[2]. Here, we choose $\Sigma(r) = \exp(-\lambda r/L)$. However, we stress that the key criterion is that $\lim_{L\to\infty} \Sigma(r) = 1$ for all sub-extensive r, with only $r \propto L$ yielding $\Sigma(r) \neq 1$ in the thermodynamic limit. With this choice, $\max \Sigma(r) = 1$ and $\min \Sigma(r) \approx 1/e^{\lambda}$ *independent* of L. Fluctuations therefore occur only on the lengthscale of the system, giving rise to a scale invariance of the potential with respect to the system size L. This is illustrated in Fig. 6.3, in which example realisations of the potential are plotted for three different system sizes. Without a legend in place, one could not distinguish the largest system size from the smallest, as the profiles of the fluctuations are qualitatively similar.

We now highlight two ways in which the maximally correlated potential is radically different from its uncorrelated counterparts. To do so, first consider the

[1] This has been tested numerically, with exponential localisation clearly found for $a \in [0, 1)$. This is because a constant value of a encodes short-ranged correlations, meaning that sites a large distance r apart are effectively uncorrelated.

[2] For instance, we have tested $\Sigma(r) = (1 - 2(r/L))^2$ and $\Sigma(r) = 1 - cr/L$ (with $0 < c < 1$), with the qualitative results of this chapter unchanged.

case of an uncorrelated Anderson model, and imagine constructing a chain of length $2L$ by connecting two independent chains of length L by a single hopping term. An exponentially localised state initially localised in the middle of one of the chains will barely be affected by this coupling, as it is sensitive only to its local environment. As the process is repeated and the chain grows, the boundary effects which arise from the added hopping terms at the ends of the chain become less and less important.

An important consequence of this is that for sufficiently large system sizes, averaging over a single chain of length $2L$ is equivalent to averaging over two chains of length L. In other words, provided one averages over a sufficiently large single realisation, then any further averaging over disorder is unnecessary.

The maximally correlated model, however, is qualitatively different. As the correlations between site energies depend explicitly on the size of the system, doubling the length L of a chain entails changing all of the site energies. As $\langle \epsilon_x \epsilon_{x+r} \rangle = \exp(-\lambda r/L)$, two nearby sites will, as L is increased, become increasingly correlated with each other, eventually to the extent that they take exactly the same value. An exponentially localised state would naturally be sensitive to this change, and its localisation length would change as a result. A traditional notion of an exponentially localised state - in which the localisation length ξ is independent of system size - is therefore impossible.

Furthermore, averaging over two chains of length L is clearly not the same as averaging over a single chain of length $2L$, as the correlations between sites in the smaller chains are not the same as those in the larger. As a result of this, we cannot expect a single large realisation of the maximally-correlated chain to reproduce disorder-averaged quantities. This line of thinking will be returned to in the next section, where we consider the consequences of the maximal correlations for the electronic properties of the system.

We begin in the next section by discussing some central results relating to the statistical properties of the correlated site-energies, and find them to be very much in agreement with the qualitative discussion above. In particular, we will show that the strong correlations present between the site energies imply strong

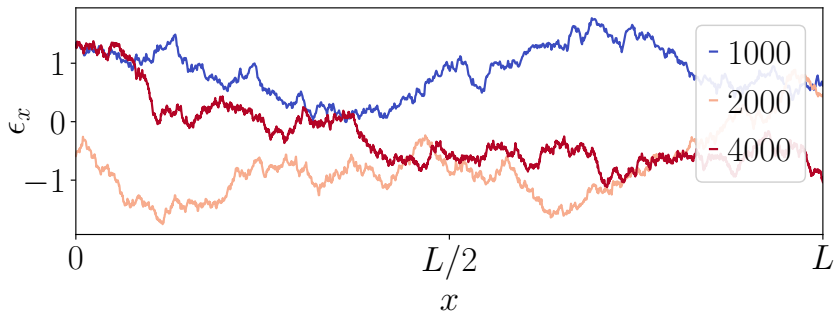


Figure 6.3: For systems of size $L = 1000$, 2000 and 4000, we plot a single disorder realisation chosen at random. As fluctuations occur on lengthscales proportional to L, the potential is self-similar with respect to L.

realisation-to-realisation fluctuations in the eigenvalue spectra. We will use this property of the model to explain the presence of the mixed region of localised and delocalised states, before analysing numerically the tabletop eigenstates.

6.2.1 Statistics of the maximally correlated chain

The site energies of the maximally correlated chain are distributed according to a multivariate Gaussian with $\Sigma_{x,y} = e^{-r/L}$, with $r = |x - y|$. In Appendix A, we derive results relating to the statistics of these site energies, of which we give a summary here.

Correlations

One may consider constructing the chain by enumerating the site energies one-by-one, beginning with site 1. With ϵ_1 drawn from a standard normal distribution, the conditional mean value of ϵ_x (with $x > 1$) is

$$\langle \epsilon_x | \epsilon_1 \rangle = \epsilon_1 \exp\left(-(x-1)/L\right). \tag{6.5}$$

For all finite x, $\langle \epsilon_x | \epsilon_1 \rangle \to \epsilon_1$ as $L \to \infty$, meaning that the sites take the same value as ϵ_1. The terminal site in the chain is also correlated with the first, with $\langle \epsilon_L | \epsilon_1 \rangle \approx \epsilon_1 / e$. As different realisations have different values of ϵ_1, the whole vector $\vec{\boldsymbol{\epsilon}}$ fluctuates from realisation-to-realisation.

More generally, we show in Appendix A that a realisation of site energies can be thought of as a correlated random walk: the conditional average of the next site

energy ϵ_x in a sequence $(\epsilon_1, \epsilon_2, \ldots, \epsilon_{x-1})$ depends only on the 'most recent' value ϵ_{x-1},

$$\epsilon_x|(\epsilon_1, \epsilon_2, \ldots, \epsilon_{x-1}) \sim \mathcal{N}_1(a\epsilon_{x-1}, 1-a^2). \tag{6.6}$$

This conditional distribution has mean value $\langle\epsilon_x\rangle \simeq (1-1/L)\epsilon_{x-1}$ and variance $\sigma^2 \simeq 2/L$ for large L, meaning that on sub-extensive lengthscales, the process is a *martingale* [126]: the conditional average of ϵ_x is equal to the previous value ϵ_{x-1}.

A consequence of the behaviour outlined in this section is that any finite-length segment of the chain will form a plateau in the thermodynamic limit, with all of the site energies in the segment taking essentially the same value. In Sec. 6.4.1, we will return to this fact to give a heuristic picture for the presence of tabletop states, which we can think of as being 'delocalised' over such plateaux.

Energy fluctuations

In Appendix A, we also demonstrate that the mean eigenvalue $\mathrm{Tr}H$ fluctuates from realisation-to-realisation as a consequence of the fluctuations in $\vec{\boldsymbol{\epsilon}}$. Specifically, we show that $\mathrm{Var}(\mathrm{Tr}H) \sim \mathcal{O}(W^2)$. We therefore re-centre the Hamiltonian as

$$\mathcal{H} = H - \mathrm{Tr}H. \tag{6.7}$$

This is equivalent to defining the band centre $\omega = 0$ of each realisation as its centre of gravity $\mathrm{Tr}H$. Using the re-centred Hamiltonian $\mathcal{H}$, and therefore referring all energies to the centre of gravity of each realisation, we work at the band centre from now on.

This re-centring process also arises in the context of many-body localisation, where the mean Fock-space site energy fluctuates with an extensive variance. There, the re-centring procedure is necessary to ensure a pristine distinction between many-body localised and extended states as a function of energy [104].

For our strongly-correlated case, however, fluctuations do not only occur in the first moment of the eigenvalue distribution (as is the case in MBL). The higher moments, too, fluctuate from realisation to realisation (see also Appendix A). Self-averaging of the eigenvalue spectrum is therefore not present. This is illustrated Fig. 6.4, where we plot the spectra of three realisations of both H and $\mathcal{H}$, alongside

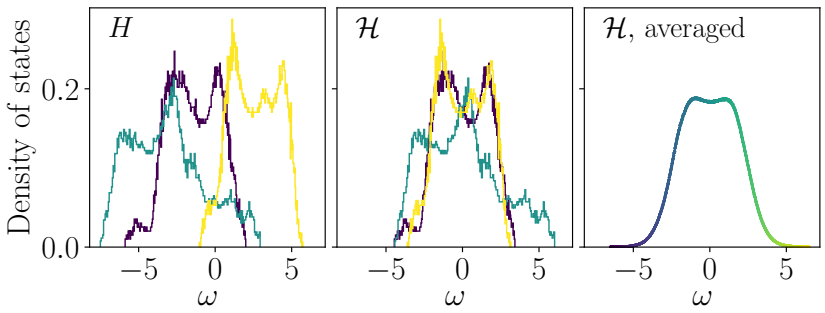


Figure 6.4: For a system of size $L = 5000$, we plot the spectra of three realisations of H (first panel) and of the recentred Hamiltonian $\mathcal{H}$ (second panel). In the third panel, we plot the disorder-averaged spectrum of $\mathcal{H}$, over 1000 disorder realisations. $W = 2$ throughout.

the disorder-averaged spectrum of $\mathcal{H}$. Though the system size ($L = 5000$) is large, strong fluctuations in both the first and higher moments of the spectra of H are visible, and the spectra of individual realisations do not reproduce the disorder-averaged spectrum.

6.3 Extended, multifractal and mixed phases

The eigenstates of maximally correlated chains are found to have an unusual structure, being approximately constant over a continuous segment of the lattice before abruptly vanishing, as illustrated in Fig. 6.2. We call these states 'tabletops'. The length ℓ of the tabletops is a natural measure of their spatial extent, akin to the localisation length of exponentially localised states. As the tabletops are always continuous, their lengths may be computed by counting the number of sites on which the state has amplitude greater than some tiny cut-off. As seen in Fig. 6.2, the vanishing of the tabletops at their endpoints is precipitous: from one site to the next, the wavefunction amplitudes go from being of order ℓ^{-1} to zero within machine precision. As such, results are insensitive to the precise value of the cut-off used, which here is taken to be 10^{-15}.

Turning now to Fig. 6.2, we begin with some qualitative observations that can be made by examining the eigenstates at different values of W. First, we find that for W less than a critical value W_L, all tabletops saturate the chain, with $\ell = L$. This is illustrated for $W = 0.5$. For $W > W_L$, but less than an upper critical value

W_U, at a given energy some disorder realisations host states with $\ell = L$, and some with $\ell < L$ (as illustrated for $W = 2$). However, for a given realisation these two types of eigenstate are found not to coexist at the same energy. Above W_U, all disorder realisations host states with $\ell < L$, as illustrated for $W = 4, 6$. Above W_L, the tabletop lengths ℓ are also found to decrease (on average) as W is increased.

Fig. 6.2 shows eigenstates only for a particular value of L. It is not the tabletop lengths *per se*, however, that distinguish extended states from multifractal states, but rather how they scale with system size. For instance, it is not possible to tell from Fig. 6.2 alone whether the tabletops for $W = 2$ are extended (with $\ell = aL$, where $0 < a < 1$), or multifractal. In the next section, we will analyse the full distributions of tabletop lengths for different values of the disorder strength W. This will reveal that for $W < W_L$, all eigenstates are extended with $\ell = L$, and that for $W > W_U$, all eigenstates are multifractal and are found to scale with system size as $\ell = cL^\alpha$, where $0 < \alpha < 1$. These latter states are *sub-extensive*: they have weight on a diverging number of sites as $L \to \infty$, but a vanishing fraction $\sim L^{\alpha-1}$ of the total number.

For $W_L < W < W_U$, we will demonstrate that the system is in the mixed regime: some realisations are in the multifractal phase and some in the extended phase. We characterise this regime by the fraction $g(W)$ of states that are extended: g smoothly interpolates between the purely extended phase (where $g = 1$) and the purely multifractal phase (where $g = 0$). Throughout the range of W studied, we also find no evidence for extended states with $\ell < L$.

6.3.1 Distribution of tabletop lengths

We denote the distribution of tabletop lengths ℓ over an ensemble of disorder realisations as $P_\ell(\ell)$. We split the contributions from extended and multifractal states by further defining

$$P_\ell(\ell) = g\delta(\ell - L) + f_L(\ell), \tag{6.8}$$

where g is the fraction of states which saturate the chain ($\ell = L$), and $f_L(\ell)$ is a smooth distribution formed of the multifractal states. We expect that $f_L(\ell)$

will depend generically on the system size L, as the multifractal states scale sub-extensively with system size. g, on the other hand, should admit a well-defined limit as L is increased, this limit being the fraction of realisations which host extended states in the thermodynamic limit.

It is important to be able to exclude the presence of extended states with $\ell = aL$, where $a < 1$. To this end, we will also plot distributions of $\tilde{\ell} = \ell/L$ and define an exponent $\alpha = \log \ell / \log L$, with corresponding distribution P_α. For an extended state satisfying $\ell = aL$, $\tilde{\ell} = a$, whereas for multifractal states with $\ell \sim L^\alpha$, $\tilde{\ell} \sim L^{\alpha-1} \to 0$ as $L \to \infty$. The exponents α are also useful in making this distinction. For an extended state with $\ell = aL$, $\alpha \to 1$ as $L \to \infty$, whereas multifractal states will lend the distribution weight at $0 < \alpha < 1$.

We begin in the delocalised phase $W < W_L$, with $W = 0.5$ used for illustrative purposes. As shown in Fig. 6.5(a), we indeed find that $P_\ell(\ell) = \delta(\ell - L)$ for L between 1250 and 20000. Likewise, $P_{\tilde{\ell}}(\tilde{\ell}) = \delta(\tilde{\ell} - 1)$, and $P_\alpha(\alpha) = \delta(\alpha - 1)$. The results are stark: over 20000 disorder realisations, states drawn from a small window around the band centre of the re-centred Hamiltonian $\mathcal{H}$ (Eq. 6.7) *all* fully saturate the chain, with $\ell = L$.

On increasing W, the system enters the mixed regime - here, we analyse results for $W = 2$ as a representative disorder strength. In Fig. 6.5(b) it can be seen that the distribution $P_\ell(\ell)$ acquires weight at sub-extensive ℓ, corresponding to the distribution $f_L(\ell)$ of multifractal states, whilst retaining weight at $\ell = L$. The persistence of extended states is also seen in Fig. 6.5(e), in which the distribution $P_{\tilde{\ell}}(\tilde{\ell})$ retains weight at $\tilde{\ell} = 1$. Fig. 6.5(e) also provides evidence that these incipient states are indeed multifractal (rather than extended states with $\ell = aL$, with $a < 1$): the weight of $P_{\tilde{\ell}}(\tilde{\ell})$ at small $\tilde{\ell}$ grows with increasing L, corresponding to the fact that $\tilde{\ell} \sim L^{\alpha-1}$ eventually vanishes as L is increased. In Fig. 6.5(h), we plot the distributions $P_\alpha(\alpha)$ for the same numerical data. Once again, the peak at $\alpha = 1$ corresponds to the presence of delocalised states, whereas the presence of multifractal states is indicated by the distribution converging (as L is increased) to

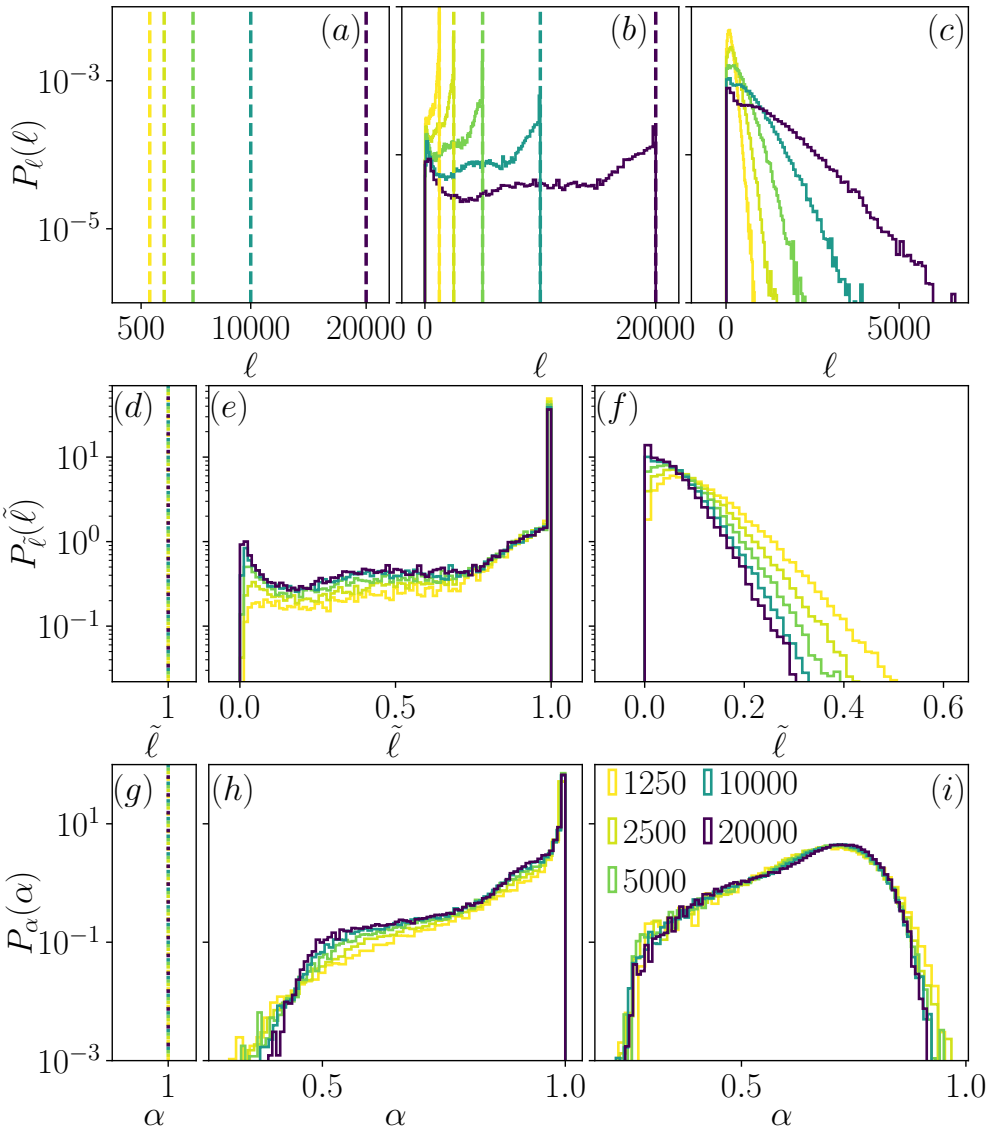


Figure 6.5: $(a) - (c)$: Distributions $P_\ell(\ell)$ for representative disorder strengths in the extended ($W = 0.5$), mixed ($W = 2$) and multifractal ($W = 8$) regimes respectively, for different system sizes L (indicated in panel (i)). $(d) - (f)$: corresponding distributions $P_{\tilde{\ell}}(\tilde{\ell})$ of $\tilde{\ell} = \ell/L$. $(g) - (i)$: corresponding distributions $P_\alpha(\alpha)$, where $\alpha = \log \ell / \log L$. Distributions are formed from states in a small window about the band centre of the Hamiltonian Eq. 6.7 for 20,000 disorder realisations.

have weight in the domain $0 < \alpha < 1$. If these states were instead extended, then the distribution P_α would converge to a peak at $\alpha = 1$ as L is increased.

Further increasing W pushes the system into the pure multifractal phase. In Fig. 6.5(c), we plot $P_\ell(\ell)$ for $W = 8$ and L between 1250 and 20000. We find that the distributions have no weight at $\ell = L$, corresponding to the fact that $g = 0$ in Eq. 6.8. In Fig. 6.5(f), the weight of $P_{\tilde{\ell}}(\tilde{\ell})$ for finite $\tilde{\ell}$ decreases as L

is increased, reflecting the fact that the distribution will eventually form a delta function at $\tilde{\ell} = 0$. That all states are indeed multifractal is further confirmed by the distribution $P_\alpha(\alpha)$ in Fig. 6.5(i), which is well-converged with L. The distribution has support strictly for $0 < \alpha < 1$; the lack of weight at $\alpha = 0$ and $\alpha = 1$ implies the absence of localised and extended states respectively.

With the presence of extended, mixed and pure multifractal regimes thus established, we present at this stage a physical interpretation of the results. Focussing on a single realisation, as W is increased we find that an extended-multifractal eigenstate phase transition takes place[3]. However, in Sec. 6.2.1, we established the fact that the density of states of the strongly-correlated model fluctuates strongly from realisation-to-realisation, even in the thermodynamic limit. Due to these strong fluctuations, different disorder realisations manifest this transition at different values of W. Loosely speaking, the 'more disordered' a realisation is, the smaller the value of W required to initiate this phase transition[4]. The mixed phase is therefore nothing more than the range of W values in which some disorder realisations are still in the extended phase, and some in the multifractal phase. In the disorder-averaged spectrum, therefore, a mixture of extended and multifractal states is present with no energy resolution between them.

In the next section, we continue our analysis of the maximally-correlated model by performing a scaling analysis of the mean and typical tabletop lengths as a function of the system size, L. These results will confirm the existence of an extended phase for $W < W_L$, as well as the presence of multifractal states for stronger disorder strengths.

Scaling of average tabletop lengths

We define scaling relations for the mean and typical tabletop lengths as

$$\ell_m \equiv \langle \ell \rangle = c_m L^{\alpha_m} \quad \text{and} \quad \ell_t \equiv \exp\langle \log \ell \rangle = c_t L^{\alpha_t}. \tag{6.9}$$

[3]As can be diagnosed, for example, by examining the tabletop lengths ℓ for a single realisation as a function of W.

[4]One way to quantify the relative amount of disorder in one realisation versus another is to compute the variance of the site energies of each realisation.

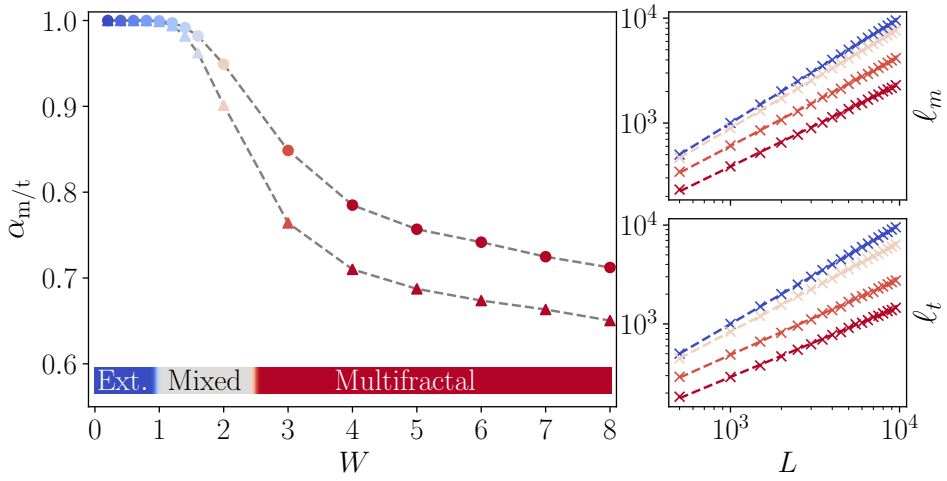


Figure 6.6: The exponents α_m (circles) and α_t (triangles) for the scaling of the mean and typical tabletop lengths (Eqns. 6.9) as functions of W. Data points in red correspond to the pure multifractal phase, and in blue to the pure extended phase. The mixed regime in-between is indicated by pale shading. Right: linear regression plots used to extract the exponents, for L between 500 and 10000, shown for $W = 0.5, 2, 3$ and 4 (from top to bottom). All data points are averaged over 5000 disorder realisations.

In Fig. 6.6 we plot the exponents $\alpha_{m/t}$ against W, alongside the regression plots used to extract them. The fits are in all cases excellent, confirming the validity of Eqns. 6.9. For $W < W_L$, $\alpha_{m/t} = 1$, as expected as all states are extended. As W is increased beyond W_L, $\alpha_{m/t}$ decrease from 1 as multifractal state emerge in the spectrum. On increasing W further into the pure multifractal phase, $\alpha_m > \alpha_t$ continue to decrease monotonically. The mixed and multifractal regimes cannot be distinguished by these exponents - as they are measures of the *average* tabletop lengths - but robust evidence for the presence of multifractal states is provided through the extraction of $0 < \alpha_{m/t} < 1$ for $W > W_L$. We note that as $L \to \infty$, $\langle\alpha\rangle$ (the mean of the distributions P_α, shown in Fig. 6.5) is given by α_t. This implies that in the pure multifractal regime (Fig. 6.5(i)), the distribution P_α converges as L is increased to have mean value $0 < \langle\alpha\rangle < 1$, excluding the possibility that these states are extended (with $\ell = aL$, where $a < 1$).

In the introduction, we explained that multifractal wavefunctions can be identified by the scaling of their moments with system size (Eq. 6.1). However, we have not yet established that the sub-extensive 'multifractal' tabletop states are indeed multifractal wavefunctions. It is to this that we turn in the next section,

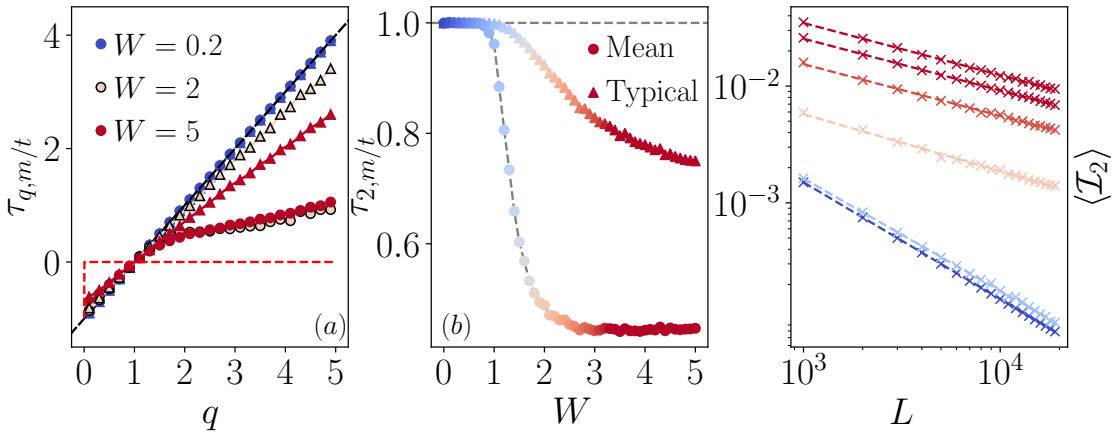


Figure 6.7: (a) Plots of the exponents $\tau_{q,m}$ (circles) and $\tau_{q,t}$ (triangles) against q (Eq. 6.10), for values of W in each regime. The black dashed line is $\tau_q = q-1$, corresponding to delocalised behaviour, and the red dashed line corresponds to localised behaviour. (b) Exponents $\tau_{2,m/t}$ against W. Right: representative regression plots of $\langle \mathcal{I}_2 \rangle$ against L, used to extract the exponents, for $W = 0, 1, 2, 3, 4, 5$ (bottom to top).

where we utilise the generalised Inverse Participation Ratios (IPRs) to probe the scaling of the wavefunction moments.

6.3.2 Generalised inverse participation ratios

The generalised Inverse Participation Ratios (IPRs), defined as $\mathcal{I}_q = \sum_x |\psi(x)|^{2q} \sim L^{-\tau_q}$, are a standard probe of eigenstate multifractality [5]. For an exponentially localised state, $\psi(x) \sim \exp(-|x - x_0|/\xi)$, where x_0 is the site of peak amplitude, and ξ the localisation length. This implies that $\mathcal{I}_q$ is independent of L, giving $\tau_q = 0$. By contrast, for a state fully delocalised over the chain, $\psi(x) \approx L^{-1/2}$, such that $\mathcal{I}_q \approx L^{1-q}$. For delocalised states, therefore, $\tau_q = q - 1$. Behaviour in-between these limits indicates eigenstate fractality, and multifractal eigenstates may have a non-linear q dependence [5]. A perfect tabletop distributed evenly over $\ell = L^\alpha$ sites would have $\psi(x) = \ell^{-1/2}$ such that $I_q = L^{-\alpha(q-1)}$. This implies that $\tau_q = \alpha(q-1)$, and hence any non-linearity (and therefore multifractality) must be attributed to finer structures in the tabletops.

We perform a scaling analysis by focussing on the mean and typical IPRs, which have scaling relations

$$\mathcal{I}_{q,m} \equiv \langle \mathcal{I}_q \rangle \sim L^{-\tau_{q,m}} \quad \text{and} \quad \mathcal{I}_{q,t} \equiv \exp\langle \log \mathcal{I}_q \rangle \sim L^{-\tau_{q,t}}. \tag{6.10}$$

In Fig. 6.7(a), we plot $\tau_{q,m/t}$ against q for values of W in each regime. For $W = 0.2$ (in the extended phase), we clearly see $\tau_{q,m/t} = q - 1$ as expected. For W in both the mixed ($W = 2$) and multifractal ($W = 5$) regimes, the presence of sub-extensive states is confirmed by $0 < \tau_{q,m/t} < q - 1$ for $q > 1$, with strong departure from nonlinearity seen most clearly for $\tau_{q,m}$, confirming the *multi*fractality of the states.

Fixing $q = 2$ (which is usually just referred to as 'the IPR'), we first plot in Fig. 6.7(b) the exponents $\tau_{2,m/t}$ against W. As expected, $\tau_{2,m/t} = 1$ for $W < W_L$, with both decreasing monotonically with W as the mixed phase is entered and sub-extensive states enter the spectrum. We include select regression plots used to extract the exponents, with excellent fits observed in all cases.

In the next section, we close our analysis of the static properties of the model by performing a transfer matrix calculation, which probes the conductance properties of the eigenstates in each regime.

6.3.3 The transfer matrix

A natural probe of the localisation properties of a finite-size system is the transmittance T of an incident wave through the chain [119–123]. To calculate T, we imagine the correlated chain to have sites labelled by $x = 1$ through to $x = L$. On either end, we attach semi-infinite clean (i.e., with zero site energy) tight-binding chains; these are the conducting 'leads'. We then send an incident Bloch wave through the left chain, with $\psi(x) = e^{ikx}$ for $x < 1$ and energy $E = -2\cos k$. The transmittance is computed by measuring the squared amplitude of this wave that makes it through the system and into the lead on the other side: $|\psi(L)|^2 = T|\psi(1)|^2$.

Realisations hosting extended eigenstates at energy E are expected to yield a finite value of $0 < T < 1$ in the thermodynamic limit. If localised states were present, then we would expect the transmittance to decay (on average), as $T \sim e^{-L/\xi_T}$, where ξ_T is an L-independent localisation length. Conventional multifractal states with polynomial tails give rise to a transmittance that decays anomalously, as $\xi_T \sim L^{\alpha_T}$, where $0 < \alpha_t < 1$ [181]. However, the multifractal tabletop states present in the maximally correlated model do not display this behaviour. As we will show,

they instead give rise to a transmittance that decays to zero with increasing L in the same manner as a localised state. This reflects the fact that the states have vanishing amplitude on all sites outside of the tabletop.

We compute the transmittance using a transfer matrix algorithm, in which the incident wave is propagated through the chain. In terms of the wavefunction amplitudes $\psi(x)$, the Hamiltonian Eq. 6.2 can be written

$$W\epsilon_x\psi(x) - \psi(x+1) - \psi(x-1) = E\psi(x), \tag{6.11}$$

which can be cast as the recursion relation

$$\begin{bmatrix}\psi(x+1)\\ \psi(x)\end{bmatrix} = \begin{bmatrix}W\epsilon_x - E & -1\\ 1 & 0\end{bmatrix}\begin{bmatrix}\psi(x)\\ \psi(x-1)\end{bmatrix}, \tag{6.12}$$

where E is the energy of the wave and ϵ_x the correlated potential on site x. Here, we use the re-centred Hamiltonian $\mathcal{H} = H - \mathrm{Tr}H$ with energy $E = 0$. In the left-hand panel of Fig 6.8, we plot the mean and typical transmittances $T^{m/t}$ as a function of W. The mean transmittance is found to decrease as W is increased, and naturally is equal to zero only when *all* realisations host multifractal states (and therefore do not transmit in the thermodynamic limit). On the other hand, the *typical* transmittance vanishes when even one realisation admits a zero transmittance[5]. The mixed regime can therefore be identified as the region in which $T^t = 0$, and $0 < T^m < 1$.

Fig. 6.8 also shows the distributions $P_T(T)$ of transmittances, computed over 5000 disorder realisations. In the extended phase ($W = 0.5$), a distribution of nonzero transmittances with mode 1 is found, as expected for conducting states. In the mixed regime ($W = 1.5$), a broad distribution of finite transmittances is seen, corresponding to conducting states, alongside a peak at $T = 0$, corresponding to multifractal states. For the pure multifractal phase ($W = 5$), only this peak at zero transmittance is seen.

[5]This is due to the definition of the typical transmittance, which is a geometric mean over disorder realisations. With $T_1, T_2, \ldots, T_N$ denoting N transmittances (computed from N different disorder realisations), the typical transmittance is defined as $T^t = \left(\prod_{j=1}^{N} T_j\right)^{1/N}$. T^t is therefore zero if any of the transmittances T_j are zero.

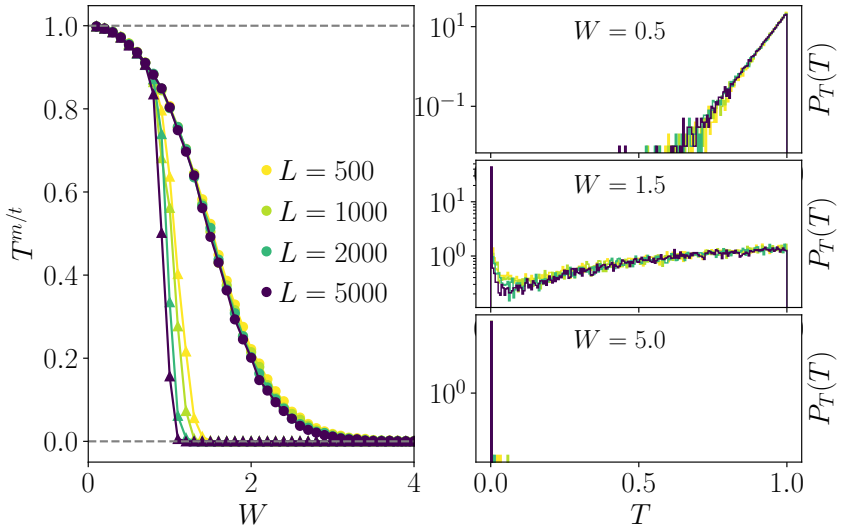


Figure 6.8: *Left*: A plot of the mean (circles) and typical (triangles) transmittance, $T^{m/t}$, as a function of W, for various system sizes L. Data are computed over 5000 realisations. *Right*: Distributions of transmittances $P_T(T)$ for the same system sizes, for $W = 0.5$, 1.5 and 5: in the delocalised, mixed and multifractal regimes respectively. Distributions are formed from 20000 disorder realisations.

The transfer matrix approach therefore distinguishes clearly the three regimes present in the localisation phase diagram of the model. Interestingly, however, the behaviour of the multifractal tabletop states was found to be different to that characteristic of 'conventional' multifractal states, such as those found at the critical points of localisation transitions [181]. In section 6.4, we investigate the imprint that these tabletop states have on the dynamics of the model.

6.4 Dynamics of the maximally correlated chain

In this section, we probe the dynamics of the maximally correlated chain in the pure multifractal regime. Whereas multifractal states are commonly associated with slow, sub-diffiusive transport [54, 124, 125], here we observe ballistic spreading of an initially localised wave packet, followed by saturation. This saturation occurs when the wavefront reaches the edges of the tabletop states, and is therefore found to occur on a timescale which scales nontrivially with system size (due to the sub-extensive scaling of the tabletop lengths with system size).

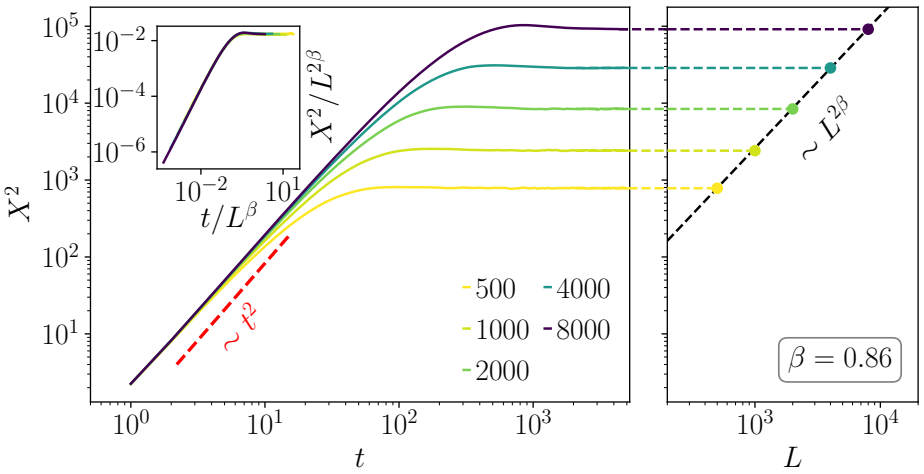


Figure 6.9: The spreading of an initially localised wavepacket in the multifractal regime ($W = 6$). *Left*: $X^2(t)$ (Eq. 6.13) plotted as a function of time for the initial state $\delta_{x,L/2}$ for different system sizes L. For small t, $X^2(t) \sim t^2$, as shown by the dashed red line. *Right*: Scaling of the saturation value as a function of L, fit to the form $X^2(t \to \infty) \sim L^{2\beta}$, with $\beta = 0.86$. *Inset*: Scale collapse of the data in the left-hand panel, demonstrating that $X^2(t) = L^{2\beta} g(t/L^\beta)$ with $g(y) \sim y^2$ for $y \ll 1$.

We consider the spreading of an initially localised wavepacket, characterised by the second moment of the wavefunction,

$$X^2(t) = \left\langle \sum_{x=1}^{L} (x - \langle x \rangle)^2 |\psi(x,t)|^2 \right\rangle, \tag{6.13}$$

with $\psi(x, t = 0) = \delta_{x,L/2}$ representing an initially completely localised wavepacket. The simplest expected behaviour for initial spreading of the wavepacket, followed by saturation, is

$$X^2(t) \sim \begin{cases} t^{2z} & ; \quad t \ll t_* \\ L^{2\beta} & ; \quad t \gg t_* \end{cases}, \tag{6.14}$$

such that t_*, the time at which the two regimes cross over, satisfies $t_* \sim L^{\beta/z}$. For a system with extended states, we would have $z, \beta = 1$, indicating ballistic transport until the wavepacket spans the entire chain. For localised states, $z, \beta = 0$ indicates the absence of transport altogether. Conventional multifractal states have $0 < z, \beta < 1$, indicating an initial sub-diffusive wavepacket spreading, followed by a sub-extensive saturation [53, 54, 124].

In Fig. 6.9 we show results for the wavepacket spreading (Eq. 6.13) for $W = 6$, in the pure multifractal phase. We find that the initial transport is ballistic, with

$z = 1$, but that the saturation value $X^2(t \to \infty) \sim L^{2\beta}$ with $\beta < 1$. The inset panel shows the scale-collapsed behaviour $X^2(t) = L^{2\beta} g(t/L^\beta)$ with $g(y) \sim y^2$ for $y \ll 1$, confirming the ballistic spreading and subextensive saturation of the wavepacket[6].

The results for the multifractal phase are in complete agreement with our picture of the tabletop states as constant over a length $\ell \sim L^\alpha$ $(0 < \alpha < 1)$, and zero elsewhere. Pursuing this idea, consider for simplicity a wavepacket initially localised in the centre of a tabletop of length ℓ, which we take to be fully extended on sites $-\ell/2 < x < \ell/2$. The wavepacket therefore spreads as a truncated Gaussian:

$$|\psi(x,t)|^2 = \Theta(\ell - 2|x|) \frac{e^{-x^2/t^2}}{t\sqrt{\pi}\ \mathrm{Erf}(\ell/2t)}, \tag{6.15}$$

where the velocity v has been absorbed into the units of time, and the step function $\Theta(\ell - 2|x|)$ imposes the fact that the wavepacket has zero weight outside of the tabletop state. The denominator $t\sqrt{\pi}\ \mathrm{Erf}(\ell/2t)$ is simply a normalisation factor. Computing $X^2(t)$ for this wavepacket gives

$$X^2_\ell(t) = \frac{1}{2} t^2 \left[1 - 2 \frac{e^{-\ell^2/4t^2} (\ell/2t)}{\sqrt{\pi}\ \mathrm{Erf}(\ell/2t)} \right]. \tag{6.16}$$

To compute $X^2(t) = \langle X^2_\ell(t) \rangle$, we must integrate over the probability distribution of the initial site residing in a tabletop of length ℓ, which we denote by $\Phi_\ell(\ell)$. This gives

$$X^2(t) = \frac{1}{2} t^2 \left[1 - \frac{2}{\sqrt{\pi}} \int \mathrm{d}\ell\ \Phi_\ell(\ell) \frac{\ell e^{-\ell^2/4t^2}}{2t\ \mathrm{Erf}(\ell/4t)} \right]. \tag{6.17}$$

For small t, a leading-order expansion of the integrand shows that $X^2(t) \sim t^2$, as expected. For very large t, on the other hand, $X^2(t) \sim \int \mathrm{d}\ell\ \Phi_\ell(\ell)\ \ell^2$ is independent of time and controlled entirely by Φ_ℓ and its non-trivial L-dependence. At the root of the anomalous exponent β, therefore, is the non-trivial scaling of the tabletop lengths with L.

Approximating these tabletop states as extended over a length ℓ and zero elsewhere is therefore a good approximation. In the next section, we provide a heuristic argument for why the maximally-correlated nature of the site energies could give rise to such states.

[6] In the mixed phase, results are an interpolation between those of the two phases as discussed above. Some realisations will host multifractal tabletop states (which overlap the central site), whereas others will host extended states that saturate the chain. As $X^2(t)$ is a disorder-averaged quantity, this implies that $0 < \beta < 1$.

6.4.1 A heuristic picture

We close with a simple heuristic argument for the presence of a multifractal regime, in which the tabletop states are approximately uniform over sub-extensive lengths. In Sec. 6.2.1, we mentioned that the sequence of site energies $\ldots, \epsilon_x, \epsilon_{x+1} \ldots$ is a martingale (proved in Appendix A): given ϵ_x, ϵ_{x+1} is Gaussian distributed with mean $e^{-1/L}\epsilon_x$ and variance $\simeq 2/L$. Sequences of site energies with sub-extensive lengths therefore have a high probability of being close in value. It is to this that we attribute the approximate uniformity of tabletops.

However, for a finite (but arbitrarily large) system the conditional distribution $P(\epsilon_{x+1}|\epsilon_x)$ is a Gaussian with unbounded support. With very low probability, therefore, a 'break' can occur in a sequence of site energies, where neighbouring sites have wildly different energies. We could attribute the breaks in the tabletops - where the tabletop vanishes rapidly to zero - to such rare regions. Since the sequence of site energies is a martingale, the probability of a break occurring at a particular site is independent of the sites prior to it. This is suggestive that the density of tabletop breaks is Poisson distributed, from which the wait time between events - the tabletop length - is exponentially distributed:

$$P_\ell(\ell) \sim e^{-\lambda \ell}, \tag{6.18}$$

where λ is the density of tabletop breaks. By nature of the strong correlations, λ decreases as L is increased. Eq. 6.18 is consistent with results for the multifractal regime. It can be seen from Fig. 6.5 (c) that the tails of the distributions $P_\ell(\ell)$ are approximately exponential, and furthermore that λ decreases as L is increased. However, we emphasise that this argument is heuristic - to obtain the precise multifractal exponents, for example, would require a theory to take into account fluctuations within the tabletops, which are naturally not captured by our simple approximation.

6.5 Discussion

In this chapter, we have investigated the eigenstate structure of a one-dimensional quantum chain (Eq. 6.2) with maximally-correlated disorder (Eq. 6.4), using primarily numerical techniques. We demonstrated that the model hosts a robust multifractal phase of sub-extensive eigenstates at strong disorder, while for weak disorder an extended phase is found. Each disorder realisation of the model hosts an eigenstate phase transition between these two phases. However, due to strong inter-sample fluctuations in the density of states, different realisations host this transition at different disorder strengths. The disorder-average phase diagram of the model therefore includes a mixed region between the two phases, in which some realisations host extended states and some multifractal.

The eigenstates of the maximally correlated chain are striking. To a good approximation, they are constant in magnitude over lengths $\ell \sim L^{\alpha}$ of the chain, and zero elsewhere - we therefore refer to them as 'tabletop' states. In the extended phase, $\alpha = 1$, and in fact all eigenstates span the entire chain. The sub-extensive multifractal states by contrast have $\alpha < 1$. These eigenstates are naturally characterised by the distributions of their lengths ℓ, as well as of the exponents α. Through analysis of the IPRs, the multifractal nature of the sub-extensive tabletops was made clear, and the three regions of the phase diagram were also distinguished through a transfer matrix calculation. In the multifractal phase, the unusual eigenstate structure leaves an imprint on the dynamics - an initially localised wavepacket spreads ballistically, but over timescales that scale as L^{β}, with $\beta < 1$. Beyond this timescale, the expansion saturates as the wavepackets hit the edges of the tabletops, with the saturation value scaling as $L^{2\beta}$.

We add that the phenomenology of the one-dimensional maximally-correlated system is vastly different from the same model considered on a Cayley tree with connectivity $K \geq 2$ [30]. There, a localisation transition (to conventional exponentially localised states) is present, and no multifractal phase is found. The

phenomenology is also very different to that in $1D$ Anderson systems with power-law (so-called "scale-free") disorder correlations, in which multifractality is also absent [182, 183].

7
Conclusion

In this thesis, we have explored the effects of strong correlations between the site energies of certain one-dimensional systems. As we have seen, these correlations can completely dominate the behaviour of the eigenstates, leading to a variety of quite unexpected behaviour. The infinite-range correlated quasiperiodic models, introduced in Chapter 3, host a wide variety of mobility edge structure: from none at all in the Aubry-André-Harper model [28], to a single mobility edge in the β model [21], to arbitrarily many in high-order mosaic models [22]. Mobility edges are not found at all in uncorrelated random systems in less than three dimensions [5]; in quasiperiodic chains, by contrast, their number and form seems to be amenable to engineering by carefully choosing the form of the potential.

Alongside quasiperiodic models, we devoted Chapter 6 to investigating a one-dimensional chain with maximally-correlated quenched random disorder. The localisation behaviour of this system was shown to be quite novel: in contrast to uncorrelated chains, delocalised states are present at weak disorder. At strong disorder, something quite unexpected happens: all eigenstates become sub-extensive and multifractal. Furthermore, the strong energy fluctuations in the model lead to a 'mixed' region separating these two phases, with the disorder-averaged spectrum consisting of both delocalised and multifractal states.

We now summarise the main results of this thesis, and offer several avenues for future research.

⁂

We began the thesis by introducing the necessary theoretical background in Chapter 2. The central object of study was the well-known probe of localisation: the local propagator. Used since Anderson's original work [4], the diagonal local propagator $G_{jj}(t) = -i\theta(t)\langle j|e^{-i\hat{H}t}|j\rangle$ is the probability amplitude that a particle initially placed on site $|j\rangle$ is still found there a time t later. If any of the eigenstates overlapping site $|j\rangle$ are localised, then $|G_{jj}(t)|^2$ will remain finite for all time. If, by contrast, all of the eigenstates are delocalised, then $|G_{jj}(t)|^2$ will decay to zero.

However, due to the lack of energy resolution afforded by the time-domain propagator, we focussed for the rest of the chapter on its Fourier transform, $G_{jj}(\omega)$. In particular, we singled out the associated *self energy* S_j, defined via $G_{jj}(\omega) = [\omega + i\eta - \epsilon_j - S_j]^{-1}$. As demonstrated in Sec. 2.2, the imaginary part $\Delta_j(\omega) = -\mathrm{Im}S_j(\omega)$ is a probabilistic order parameter for localisation. Physically, it corresponds to the rate of loss of probability amplitude from site j into overlapping eigenstates of energy ω, and hence is finite in the delocalised phase and vanishingly small (as $\Delta_j \propto \eta$) in the localised phase. A conjugate order parameter $y_j(\omega) \equiv \Delta_j(\omega)/\eta$ was also introduced, which is finite in the localised phase and divergent in the delocalised phase. These order parameters have been used with considerable success in both single and many-particle random systems [29, 34, 72, 73]. By accumulating statistics over disorder realisations (or phase factors, in the case of quasiperiodic models) and/or sites, distributions of Δ and y can be formed. Crucially, these distributions are heavy-tailed, and hence are parametrised by their typical values (geometric means) Δ_{typ} and y_{typ}, rather than their means.

A large part of the chapter was spent deriving the renormalised perturbation series (RPS) for the self energy. The RPS represents S_j as a sum of all non-intersecting paths that begin and end at site j, with the nodes of the paths

corresponding themselves to propagators (albeit with sites in the lattice deleted) [31–33]. This renormalisation procedure eliminates trivial divergences in the self energy, and allows approximate theories to be systematically developed by truncating the RPS at different orders. Crucially, the RPS takes on a simple form on Bethe lattices (a category that includes $1d$ chains). The chapter was then closed in Sec. 2.2.5 by explaining that it is the *end-site* self energy of a semi-infinite half chain that should be focussed on for $1d$ systems. This was first realised by Abou-Chacra, Anderson and Thouless [34]: the RPS may be used to relate the end-site self energy of a site j to that of site $j+1$ (and so on), and hence is ripe for the implementation of approximate theories. Not only that, but the end-site self energy may also be represented as a simple continued fraction (CF), in which form its convergence properties may be studied.

Before utilising these ideas and results in practise, we first introduced quasiperiodic models in Chapter 3. Characterised by periodic potentials which are incommensurate with an underlying lattice, quasiperiodic models host a wide variety of localisation phenomena already in one dimension. In particular, the models host many different types of *mobility edges*: loci of points in energy and parameter space that separate localised and delocalised states.

We began by introducing the celebrated Aubry-André-Harper (AAH) model in Sec. 3.1, which is a simple tight-binding chain with site energies drawn from a cosine wave with an irrational wavelength [28]. As the ratio V/J of the potential strength to the hopping strength increased to 2, the AAH model displays an energy-independent localisation transition. This is due to a self-duality between position and momentum bases in the model. This situation is fine-tuned, as a generic perturbation to the Hamiltonian will destroy the symmetry and lead to the presence of a *bona fide* energy-dependent mobility edge.

In Sec. 3.2, we introduced two post-AAH models, both of which are modifications to the simple cosine potential. The first, which we call the β model, is defined by [21]

$$\epsilon_j^{\beta} = \frac{\epsilon_j^{\mathrm{AAH}}}{1-\beta\epsilon_j^{\mathrm{AAH}}}, \tag{7.1}$$

where $-1 < \beta < 1$. This model hosts a single linear mobility edge, which can be rationalised by considering how this distortion skews the distribution of site energies in the chain. The second model, from a family of *mosaic models* [22], is defined by setting to zero every other site energy in an AAH chain. Despite its simple definition, this mosaic model displays two hyperbolic mobility edges which enclose a central band of delocalised states.

This set of three models was chosen both to reflect a wide range of localisation behaviour, but also because their mobility edges are known exactly. They therefore provide the ideal test set for the theoretical work in the subsequent two chapters.

The first main goal of this thesis was to create a theoretical framework to understand localisation in quasiperiodic models. We began in Chapter 4 by constructing a first-order self-consistent theory for the self energy. Despite its simplicity, the theory gave analytical access to the locations of mobility edges and spectral band edges, as well as the distributions of the self energy in the localised and delocalised phases. For the Aubry-André-Harper and mosaic models, the predicted mobility edges were the exact expressions; for the β model, the mobility edge was approximately captured, with the result becoming exact in the limit of small β.

In Sec. 4.2.1, we first demonstrated numerically the validity of the self energy as an order parameter for localisation, before deriving the mean-field equations in Sec. 4.3. Simple expressions for Δ_{typ} and y_{typ} were derived, which take as input the potentials of arbitrary models. An integral equation for the locations of mobility edges was also presented and analysed, as well as expressions for the full distributions $P_\Delta(\Delta)$ and $P_y(y)$ of Δ and y.

In Secs. 4.4 and 4.5 these results were then put to use on the three models introduced in Chapter 3. Somewhat surprisingly, excellent agreement was found between the results of the simple theory and numerical data obtained via exact diagonalisation. The localisation phase diagrams were in each case found to be in good qualitative agreement with the numerics, and the distributions $P_\Delta(\Delta)$ and $P_y(y)$ captured the important features of the exact distributions, including the ubiquitous Lévy tail $P_y(y) \sim y^{-3/2}$ for $y \gg 1$ in the localised phase.

Certain fine details, however, were missed by the first-order theory. For example, the bands of quasiperiodic models are characterised by the presence of fractal gaps; the first-order theory, by contrast, predicts smooth bands with no gaps. Atop the Lévy tails of the distributions $P_y(y)$, too, are present fine structures which were not captured by the theory. These details can be attributed to the infinite-ranged correlations manifestly present in quasiperiodic models, and we conjectured that going to higher order in the RPS might recover them.

Because of the success and simplicity of the first-order theory, we suggest here several avenues for future research. First, extending the theory to models defined on higher-dimensional Bethe lattices or with both first- and second-nearest-neighbour hoppings would be an interesting exercise. In both cases, the general framework of the renormalised perturbation series for the self energy holds, though with a substantially different structure. Self-consistent theories similar to the one developed in this chapter have been used successfully to understand many-body localisation in disordered models [29, 72, 73, 104]. Extending the process to many-body quasiperiodic models, whose correlations in real space will manifest as correlations between Fock space sites, still remains a challenge.

Prompted by the shortcomings of the leading-order theory, In Chapter 5 we extended our analysis to arbitrary orders in the RPS. The central idea was that the recursive nature of the self energy equations allow one to express S_0 in terms of any S_ℓ with $\ell > 0$. This results in the following beautiful continued fraction (CF) for S_0:

$$S_0(\omega) = \cfrac{J^2}{\omega + i\eta - V\epsilon_1 - \cfrac{J^2}{\omega + i\eta - V\epsilon_2 - \cfrac{J^2}{\ddots}}}. \tag{7.2}$$

We began in Sec. 5.2 by deriving this result, along with series expressions for Δ_0 and y_0. In particular, the series for y_0 was shown to take on a simple form in the localised phase, and is evaluated *directly* in the thermodynamic limit. In Sec. 5.3, we explored the connection between the convergence properties of the CF (and associated series representations) and the localisation properties of the eigenstates. In the localised phase, the series for y_0 converges rapidly to the exact result, with the

precise order of convergence depending on the localisation length of the states, which grows in proximity to the mobility edges. Where delocalised states are present, the framework itself breaks down and $y_0 \to \infty$ as the order of evaluation is increased. The convergence properties of the series for y_0 may therefore be used to map out localisation phase diagrams and the associated mobility edges. In the extended phase, the CF for Δ_0 does not rapidly converge to the exact result; rather, evaluating it at order ℓ gives the same result as the exact diagonalisation of a chain of length $L = \ell$.

In Sec. 5.4, we showed how the CF and series representations for the self energy can be used to create arbitrary-order self-consistent theories. After deriving the central mean-field equations, we made an important connection between the fate of the higher-order theories and the convergence of the CF. In the localised phase, the rapid convergence of the CF for the self energy likewise implies a rapid convergence of the self-consistent theories to the exact result. In the delocalised phase, such rapid convergence is of course absent, though the self-consistent and CF approaches converge to the same result, which is that obtained numerically from a finite chain of length $\ell = L$. In Sec. 5.5, we compare the distributions $P_\Delta(\Delta)$ and $P_y(y)$ as obtained from the bare CF, the higher-order theories, and numerical data. As expected, in the localised phase both the CF and self-consistent theories give distributions $P_y(y)$ which rapidly converge to the exact result, recovering the fine structure that was missed in the first-order distributions in chapter 4. In the delocalised phase, mutual convergence with increasing order ℓ was again seen, though high-order theories are required to give accurate results.

In Sec. 5.5.1, we demonstrated that by going to higher order in the RPS, and hence accounting for longer-ranged correlations in the potential, the bandgaps missed at first order are indeed recovered. Crucially, however, the qualitative predictions of the first-order theory are unchanged at higher order. A case for the robustness of the leading-order treatment was thus made.

Our results could prove useful for the future study of novel quasiperiodic models. What the first order theory lacks in quantitative accuracy, it makes up for in its simplicity, readily yielding approximate expressions for the locations of mobility

edges. Where exact results are desired in the localised phase, it is suggested that the CF for the self energy be used. In converging rapidly to the exact result, and in being evaluated directly in the thermodynamic limit, this method possesses significant advantages over the traditionally used exact diagonalisation. Though rapid convergence is not achieved in the delocalised phase, evaluating the CF for Δ_0 at order ℓ is more efficient than the exact diagonalisation of a chain of length $L = \ell$.

In going to higher orders in the CF, we revealed the anomalous scaling of Δ_{typ} with L at critical points/mobility edges, which is a qualitatively new result. Establishing a connection between this and the anomalous scaling of the generalised inverse participation ratios of the critical eigenstates would be an interesting avenue for future research. Formally, the residues at the poles of the *full* propagator $G_j(\omega)$ give the eigenstate amplitudes on site j, from which the IPRs may be constructed. However, the structure of the RPS for the full propagator is more complicated than that of the half-chain, and hence we leave this analysis for future research. Such an advance would aid understanding both of the critical points of the models considered here, and also models which are critical throughout, such as Fibonacci chains [26, 27].

⁂

In Chapter 6, we turned to the maximally correlated chain. We began in Sec. 6.1 by discussing the phenomenon of eigenstate multifractality, with particular attention paid to the fact that multifractal states are often *fine tuned*. They occur at select points in the parameter space of Hamiltonians, and hence may be destroyed by small perturbations. For example, multifractal states occur *at* the localisation transitions/mobility edges of quasiperiodic and Anderson models. The maximally correlated chain, by contrast, was introduced as a novel pathway to robust multifractality in a one-dimensional short-ranged system.

In Sec. 6.2, the model was defined as a $1d$ tight-binding chain with site energies drawn from a multivariate Gaussian distribution. The covariance matrix Σ was

chosen to depend only on the distance r between sites in the chain, as

$$\langle \epsilon_j \epsilon_{j+r} \rangle \equiv \Sigma_{j,j+r} \equiv \Sigma(r) = f(r/L), \tag{7.3}$$

where $\lim_{y\to 0} f(y) = 1$. This criterion ensures that any pair of sites separated by a finite or sub-extensive distance have a correlation of 1 in the thermodynamic limit, and hence take the same value. As the correlation between any two sites depends on the length of the chain, exponentially localised states cannot be present in the system.

In Sec. 6.2.1 (see also Appendix A), we derived key results pertaining to the statistics of the correlated site energies, with the specific choice of $\Sigma(r) = \exp(-r/L)$. Two significant results were shown: first, that the sequence of site energies can be thought of as a correlated random walk, and secondly that realisation-to-realisation fluctuations in the moments of the density of states (DoS) are present even in the thermodynamic limit. These fluctuations necessitate re-centring the Hamiltonian of each realisation as $H \to H - \mathrm{Tr}H$ before averaging over disorder. The fluctuations in the higher moments of the DoS also explain the presence of the mixed region. Each realisation hosts an extended-multifractal eigenstate phase transition at a certain critical value of the disorder strength. Due to the fluctuations, however, different realisations have different critical values, even in the thermodynamic limit. The mixed region is simply the range of disorder strengths for which some realisations are still in the extended phase, and some in the mixed phase.

Sec. 6.3 was devoted to a thorough numerical analysis of the system, providing support for the picture outlined above. Focussing on the eigenstates of the model, we made the observation that they are approximately flat over continuous segments of the chain, and zero elsewhere. We therefore dubbed the states *tabletop* states, with their lengths ℓ a natural probe of their participation on the lattice. These states are quite unusual; multifractality is usually associated with simultaneous rare amplitude peaks and long polynomial tails.

We began the analysis in Sec. 6.3.1 by looking at the distributions $P_\ell(\ell)$ of tabletop lengths. In the extended phase, every eigenstate satisfies $\ell = L$: the states saturate the chain. Multifractal states, by contrast, satisfy $\ell \sim L^\alpha$, with

$\alpha < 1$. By examining how the distributions scale with L, the three phases can be distinguished. In Sec. 6.3.2, we supplemented this analysis with calculations of the generalised inverse participation ratios (IPR), which revealed the multifractal nature of the sub-extensive states which appear at stronger disorder. A transfer matrix calculation was also performed (in Sec. 6.3.3), generating distributions of the transmittances T of incident waves through the system. As extended states are associated with finite transmission, and multifractal states vanishing transmission, the distributions $P_T(T)$ of transmittances cleanly distinguish the three phases.

In Sec. 6.4, we examined the imprint these anomalous multifractal states have on the dynamical properties of the system. Conventional multifractality is commonly associated with slow, sub-diffusive dynamics [53, 125, 179, 180]. In the multifractal phase present here, however, an initially localised wavepacket spreads ballistically until a saturation time is reached. This time scales nontrivially with system size, as a result of the scaling of the underlying tabletop states. A heuristic calculation was performed, for which we approximated the tabletop states as perfectly uniform over a length ℓ of the chain. This was shown to recover qualitatively correctly the dynamical behaviour of the system.

Lastly, we closed in Sec. 6.4.1 by presenting a heuristic picture for the presence of multifractal tabletop states in the model. At the root of the approximate uniform nature of the tabletops is the fact that any sub-extensive length of chain will, as L is made sufficiently large, become a plateau of constant site energies. At the same time, for any finite sized system there is a finite, though small, probability of there being a 'jump' in the potential between successive sites. The edges of the tabletop states, where the wavefunction vanishes, could be attributed to such rare jumps.

We here reiterate that the correlations discussed in Chapter 6 are inspired by the form of those present in the problem of many-body localisation (MBL), which may be cast as a tight-binding model in the Fock space (FS) of many-body states [72, 104]. The effective disorder in FS is maximally correlated [29, 30], and many-body localised eigenstates exhibit multifractality in the FS [105, 111, 132]. However, we note that the structure of FS is vastly different to the one-dimensional

system considered in this chapter: the local connectivity of a lattice site in FS is extensive, and the dimensionality of the space typically exponentially large in the number of particles. Indeed, this latter property could be considered as the origin of the maximal correlations [29]: given N random site energies (in real space), and $\sim \exp(N)$ FS sites, strong correlations between the sites are inevitable. Whether a concrete connection between these maximal correlations and the resultant multifractality in Fock space can be made, remains an open question.

Appendices

A

Statistics of the maximally-correlated chain

In this appendix, we derive results pertaining to the statistics of the site energies of the maximally-correlated chain, which was introduced in Chapter 6.

A.1 Multivariate Gaussian distribution of site energies

We write $\vec{\boldsymbol{\epsilon}} \sim \mathcal{N}_L(\vec{\boldsymbol{\mu}}, \Sigma)$ to denote that $\vec{\boldsymbol{\epsilon}} = (\epsilon_1, \epsilon_2, \ldots, \epsilon_L)^T$ is distributed according to a multivariate Gaussian distribution with mean $\vec{\boldsymbol{\mu}}$ and covariance matrix Σ. Letting $\vec{\boldsymbol{\mu}} = \vec{\mathbf{0}}$, the probability density function of $\vec{\boldsymbol{\epsilon}}$ is

$$f_\epsilon(\vec{\boldsymbol{\epsilon}}) = \left(\frac{1}{2\pi}\right)^{L/2} \frac{1}{\sqrt{|\Sigma|}} \exp\left\{-\frac{1}{2}\vec{\boldsymbol{\epsilon}}^T \Sigma^{-1} \vec{\boldsymbol{\epsilon}}\right\}. \tag{A.1}$$

$|\Sigma| = \det\Sigma$, and we have used the fact that $\langle\vec{\boldsymbol{\epsilon}}\rangle = \vec{\mathbf{0}}$, where $\langle\ldots\rangle = \int \mathrm{d}\vec{\boldsymbol{\epsilon}} \ldots f_\epsilon(\vec{\boldsymbol{\epsilon}})$. Consider for simplicity $L = 5$, for which Σ and its inverse are given by

$$\Sigma = \begin{pmatrix} 1 & a & a^2 & a^3 & a^4 \\ a & 1 & a & a^2 & a^3 \\ a^2 & a & 1 & a & a^2 \\ a^3 & a^2 & a & 1 & a \\ a^4 & a^3 & a^2 & a & 1 \end{pmatrix} \quad ; \quad \Sigma^{-1} = \frac{1}{1-a^2} \begin{pmatrix} 1 & -a & 0 & 0 & 0 \\ -a & 1+a^2 & -a & 0 & 0 \\ 0 & -a & 1+a^2 & -a & 0 \\ 0 & 0 & -a & 1+a^2 & -a \\ 0 & 0 & 0 & -a & 1 \end{pmatrix}. \tag{A.2}$$

The tridiagonal structure of Σ^{-1} holds for arbitrary L, and $|\Sigma| = (1-a^2)^{L-1}$. We first derive the conditional and marginal distributions of sections of the chain. To

this end, partition the chain into sections a and b, as

$$\vec{\boldsymbol{\epsilon}} = \begin{pmatrix} \vec{\boldsymbol{\epsilon}}_a \\ \vec{\boldsymbol{\epsilon}}_b \end{pmatrix} \quad \text{where} \quad \vec{\boldsymbol{\epsilon}}_a = \begin{pmatrix} \epsilon_1 \\ \vdots \\ \epsilon_m \end{pmatrix} \quad \text{and} \quad \vec{\boldsymbol{\epsilon}}_b = \begin{pmatrix} \epsilon_{m+1} \\ \vdots \\ \epsilon_L \end{pmatrix}. \tag{A.3}$$

The covariance matrix is partitioned similarly as

$$\Sigma = \begin{pmatrix} \Sigma_{aa} & \Sigma_{ab} \\ \Sigma_{ba} & \Sigma_{bb} \end{pmatrix}. \tag{A.4}$$

Now, as $\vec{\boldsymbol{\epsilon}} \sim \mathcal{N}_L(\vec{\mathbf{0}}, \Sigma)$, the marginal distribution of $\vec{\boldsymbol{\epsilon}}_a$ is also a Gaussian distribution,

$$\vec{\boldsymbol{\epsilon}}_a \sim N_m(\vec{\mathbf{0}}, \Sigma_{aa}). \tag{A.5}$$

This shows that any finite-length (or sub-extensive) contiguous section of the chain will, in the thermodynamic limit, form a plateau, as all elements of Σ_{aa} become equal to one. It also implies that the marginal distribution of a single site energy is a standard normal distribution. Now, consider the conditional distribution of $\vec{\boldsymbol{\epsilon}}_b$ given $\vec{\boldsymbol{\epsilon}}_a$, which is given by

$$\vec{\boldsymbol{\epsilon}}_b | \vec{\boldsymbol{\epsilon}}_a \sim N_{L-m}(\tilde{\mu}_b,\ \tilde{\Sigma}_b), \tag{A.6}$$

where

$$\tilde{\mu}_b = \Sigma_{ba}\Sigma_{aa}^{-1}\vec{\boldsymbol{\epsilon}}_a \quad \text{and} \quad \tilde{\Sigma}_b = \Sigma_{bb} - \Sigma_{ba}\Sigma_{aa}^{-1}\Sigma_{ab}. \tag{A.7}$$

Using this result, we can write down the conditional distribution for the sites $\epsilon_2, \epsilon_3, \ldots \epsilon_L$ upon specifying the energy of the root site ϵ_1. The mean $\tilde{\mu}_b$ is given by

$$\tilde{\mu}_b = \Sigma_{b1}\epsilon_1 = \epsilon_1(a, a^2, \ldots, a^{L-1}), \tag{A.8}$$

and for the $L = 5$ system above, the covariance matrix $\tilde{\Sigma}_b$ is given by

$$\tilde{\Sigma}_b = \begin{pmatrix} 1-a^2 & a(1-a^2) & a^2(1-a^2) & a^3(1-a^2) \\ a(1-a^2) & 1-a^4 & a(1-a^4) & a^2(1-a^4) \\ a^2(1-a^2) & a(1-a^4) & 1-a^6 & a(1-a^6) \\ a^3(1-a^2) & a^2(1-a^4) & a(1-a^6) & 1-a^8 \end{pmatrix}. \tag{A.9}$$

With $|\tilde{\Sigma}_{bb}| = (1-a^2)^{L-1}$, we arrive at

$$\tilde{\Sigma}_b^{-1} = \frac{1}{1-a^2}\begin{pmatrix} 1+a^2 & -a & 0 & 0 \\ -a & 1+a^2 & -a & 0 \\ 0 & -a & 1+a^2 & -a \\ 0 & 0 & -a & 1 \end{pmatrix}, \tag{A.10}$$

which is simply Σ^{-1} with the first row and column deleted. This result holds for all L.

Focus now on a single site x in the chain, having specified the value of ϵ_1. The mean value of ϵ_x is given by $\langle \epsilon_x | \epsilon_1 \rangle = \epsilon_1 a^{x-1}$. For a constant value of $0 < a < 1$, this mean value would decay to zero as x is increased (reflecting short-ranged correlations). For $a = \exp(-\lambda/L)$, however,

$$\langle \epsilon_x | \epsilon_1 \rangle = \epsilon_1 \exp(-(x-1)\lambda/L) \xrightarrow{L\to\infty} \epsilon_1, \tag{A.11}$$

for all finite x. The terminal site of the chain has $\mu_L \approx \epsilon_1/e^{\lambda}$; together, these results show that we expect significant realisation-to-realisation fluctuations in the set of site energies.

A.2 Pair distributions and correlated random walks

From the marginal distribution of sites 1 and 2, which is denoted $f(\epsilon_1, \epsilon_2) \sim \mathcal{N}_2\left(\vec{\mathbf{0}}, \Sigma_2\right)$, where $\Sigma_2 = \begin{pmatrix} 1 & a \\ a & 1 \end{pmatrix}$, we can obtain the conditional distribution of $\epsilon_2|\epsilon_1 \sim \mathcal{N}_1(a\epsilon_1, 1-a^2)$,

$$f(\epsilon_2|\epsilon_1) = \frac{1}{\sqrt{2\pi(1-a^2)}} \exp\left\{-\frac{1}{2}\frac{(\epsilon_2 - a\epsilon_1)^2}{1-a^2}\right\}. \tag{A.12}$$

Now, this pair structure holds in general, with $\epsilon_x|(\epsilon_1, \epsilon_2, \ldots, \epsilon_{x-1}) \sim \mathcal{N}_1(a\epsilon_{x-1}, 1-a^2)$. In other words, the conditional distribution for a given site in the chain depends only on the site to its left. We first sketch a proof of this result, before fully explaining its consequences.

Splitting the chain $(\epsilon_1, \epsilon_2, \ldots, \epsilon_L)^T$ into partitions $\vec{\boldsymbol{\epsilon}}_a = (\epsilon_1, \ldots, \epsilon_{L-1})^T$, and $\epsilon_b = \epsilon_L$, we have that $\epsilon_b|\vec{\boldsymbol{\epsilon}}_a \sim \mathcal{N}_1(\tilde{\mu}_b, \tilde{\Sigma}_b)$, where

$$\tilde{\mu}_b = \Sigma_{ba}\Sigma_{aa}^{-1}\epsilon_a, \quad \tilde{\Sigma}_b = 1 - \Sigma_{ba}\Sigma_{aa}^{-1}\Sigma_{ab}. \tag{A.13}$$

To compute $\Sigma_{ba}\Sigma_{aa}^{-1}$, we note that $\Sigma_{ba} = (a^{L-1}, a^{L-2}, \ldots, a)$, and Σ_{aa}^{-1} is given by a matrix of dimension $L-1$ exactly as in Eq. A.2. The obvious structure in the equations gives

$$\Sigma_{ba}\Sigma_{aa}^{-1} = (0, 0, \ldots, a), \tag{A.14}$$

such that the stated result follows: $\epsilon_L|(\epsilon_1, \epsilon_2, \ldots) \sim \mathcal{N}_1(a\epsilon_{L-1}, 1-a^2)$. The reason that this is so important is that the whole distribution of $\vec{\boldsymbol{\epsilon}}$ can be written as

$$f(\vec{\boldsymbol{\epsilon}}) = f(\epsilon_1)f(\epsilon_2|\epsilon_1)f(\epsilon_3|\epsilon_1,\epsilon_2)\ldots f(\epsilon_L|\epsilon_1,\ldots,\epsilon_{L-1}) \tag{A.15}$$

$$= f(\epsilon_1)f(\epsilon_2|\epsilon_1)f(\epsilon_3|\epsilon_2)\ldots f(\epsilon_L|\epsilon_{L-1}) \tag{A.16}$$

$$= f(\epsilon_1)\prod_{l=2}^{L} f(\epsilon_l|\epsilon_{l-1}). \tag{A.17}$$

The conditional distribution $f(\epsilon_x|\epsilon_{x-1})$ has standard deviation $\sigma = \sqrt{1-a^2} \simeq \sqrt{2/L}$ for large L, and expectation value $\langle\epsilon_x|\epsilon_{x-1}\rangle = a\epsilon_{x-1} \simeq (1-L^{-1})\epsilon_{x-1}$. In the thermodynamic limit, $a = \exp(-1/L) \to 1$ such that the two sites take the same value. A given realisation of site energies, therefore, can be thought of as a correlated random walk. On sub-extensive lengthscales, the process is a *martingale* [126]: the conditional average of the next site energy ϵ_x in a sequence $(\epsilon_1, \epsilon_2, \ldots, \epsilon_{x-1})$ is equal to the most recent value ϵ_{x-1}.

As a last result, we may integrate out site energies between sites separated by a distance greater than one. For example, we may perform the contraction $f(\epsilon_3|\epsilon_1) = \int \mathrm{d}\epsilon_2 \; f(\epsilon_3|\epsilon_2)f(\epsilon_2|\epsilon_1)$ to give

$$f(\epsilon_3|\epsilon_1) \sim \mathcal{N}_1(a^2\epsilon_1, 1-a^4). \tag{A.18}$$

Integrating out $r-1$ sites gives

$$f(\epsilon_{x+r}|\epsilon_x) \sim \mathcal{N}_1(a^r\epsilon_x, 1-a^{2r}). \tag{A.19}$$

A.3 Distribution of average eigenvalue

The mean eigenvalue of the Hamiltonian Eq. 6.2 is $\mathrm{Tr}H = L^{-1}\sum_n \langle\psi_n|H|\psi_n\rangle = L^{-1}\sum_n E_n$. Changing to the basis of sites $\{|x\rangle\}$, we can write this as $\mathrm{Tr}H = L^{-1}\sum_x \langle x|H|x\rangle = L^{-1}W\sum_x \epsilon_x$. Defining

$$S_1 = W^{-1}\mathrm{Tr}H = \frac{1}{L}\sum_x \epsilon_x, \tag{A.20}$$

it is clear that $\langle S_1 \rangle = 0$, and furthermore that S_1, as a sum of Gaussian-distributed variables, is itself Gaussian distributed. The second moment is given by

$$L^2 \langle S_1^2 \rangle = \sum_{xy} \langle \epsilon_x \epsilon_y \rangle = L + \sum_{x \neq y} C_{xy} \tag{A.21}$$

$$= L + 2 \sum_{r=1}^{L-1} (L - r) a^r. \tag{A.22}$$

This is because there are $L - r$ pairs of spins separated by distance r. We have

$$\sum_{r=1}^{L-1} (L - r) a^r = \frac{a[L(1-a) + a^L - 1]}{(1-a)^2}. \tag{A.23}$$

For $a = \exp(-\lambda/L)$ the variance of the mean site energy is therefore

$$\langle S_1^2 \rangle = L + \frac{2a[L(1-a) + a^L - 1]}{(1-a)^2} \tag{A.24}$$

$$= \frac{2}{\lambda^2} \left[\lambda - 1 + e^{-\lambda} \right] + \mathcal{O}(L^{-1}) \overset{\lambda=1}{=} \frac{2}{e} + \mathcal{O}(L^{-1}). \tag{A.25}$$

To state this result in words, for the maximally correlated problem, the mean site energy is Gaussian distributed with zero mean and an $\mathcal{O}(1)$ variance. By contrast, an Anderson problem (for which $a = 0$) has variance $\langle S_1^2 \rangle \sim \mathcal{O}(L^{-1})$ which vanishes in the thermodynamic limit[1]. This is also true for quasiperiodic models. For instance, for the Aubry-André-Harper model (see Sec. 3.3) $S_1 = L^{-1} \sum_i \cos(\tilde{\kappa} i + \phi)$, where $\tilde{\kappa} \equiv 2\pi\kappa$, giving

$$\langle S_1^2 \rangle = \frac{1}{2\pi L^2} \sum_{l,m} \int_0^{2\pi} \mathrm{d}\phi \; \cos(\tilde{\kappa} l + \phi) \cos(\tilde{\kappa} m + \phi) = \frac{1}{2L^2} \frac{\sin^2(\tilde{\kappa} L/2)}{\sin^2(\tilde{\kappa}/2)}, \tag{A.26}$$

which vanishes in the thermodynamic limit.

The strong fluctuations in the mean eigenvalue of the maximally-correlated chain, which do not disappear as the system is made larger, necessitate a re-centring of the Hamiltonian,

$$\mathcal{H} = H - \mathrm{Tr} H. \tag{A.27}$$

See Sec. 6.2.1 for further discussion.

[1] $\langle S_1^2 \rangle \sim \mathcal{O}(L^{-1})$ also vanishes for a fixed $a < 1$.

A.4 Fluctuations in higher moments of the spectrum

In this section, we prove that the second moment of the eigenvalue spectrum fluctuates from realisation-to-realisation. We denote the variance of the spectrum of a single disorder realisation of the re-centred Hamiltonian Eq. A.27 by $\mathcal{X} \equiv \mathrm{Tr}\mathcal{H}^2$, given by

$$\mathcal{X} = \frac{W^2}{L}\sum_x \epsilon_x^2 - \frac{W^2}{L^2}\sum_{x,y}\epsilon_x\epsilon_y + 2t^2. \tag{A.28}$$

The disorder average of $\mathcal{X}$ therefore follows as

$$\langle\mathcal{X}\rangle = W^2(1-\langle S_1^2\rangle) + 2t^2. \tag{A.29}$$

This is the variance of the disorder-averaged spectrum of $\mathcal{H}$ (Eq. 6.7). To prove the lack of self-averaging in the eigenspectrum of the model, therefore, we need only show that $\mathcal{X}$ fluctuates from realisation to realisation. This would imply that a single large realisation would not generate a spectrum with variance given by Eq. A.29. To this end, we compute the variance $\mathrm{var}(\mathcal{X}) = \langle\mathcal{X}^2\rangle - \langle\mathcal{X}\rangle^2$. The first term is

$$\begin{aligned}\langle\mathcal{X}^2\rangle &= \left\langle\left(\frac{W^2}{L}\sum_i\epsilon_i^2 + 2t^2 - \frac{W^2}{L^2}\sum_{ij}\epsilon_i\epsilon_j\right)\left(\frac{W^2}{L}\sum_i\epsilon_i^2 + 2t^2 - \frac{W^2}{L^2}\sum_{ij}\epsilon_i\epsilon_j\right)\right\rangle \\ &= \frac{W^4}{L^2}\underbrace{\sum_{ij}\langle\epsilon_i^2\epsilon_j^2\rangle}_{A} + \frac{4t^2W^2}{L}\underbrace{\sum_i\langle\epsilon_i^2\rangle}_{B} - \frac{2W^4}{L^3}\underbrace{\sum_{ijk}\langle\epsilon_i^2\epsilon_j\epsilon_k\rangle}_{C} - \frac{4t^2W^2}{L^2}\underbrace{\sum_{ij}\langle\epsilon_i\epsilon_j\rangle}_{D} \\ &\quad + 4t^4 + \frac{W^4}{L^4}\underbrace{\sum_{ijkl}\langle\epsilon_i\epsilon_j\epsilon_k\epsilon_l\rangle}_{E}.\end{aligned} \tag{A.30}$$

The two trivial terms of Eq. A.30 are

$$B = L \quad ; \quad D = L^2\langle S_1^2\rangle. \tag{A.31}$$

For the other terms, we shall use Wick's probability theorem [184], beginning with A:

$$A = \sum_{ij}\langle\epsilon_i^2\rangle\langle\epsilon_j^2\rangle + 2\langle\epsilon_i\epsilon_j\rangle^2. \tag{A.32}$$

Now, note that the second term in the sum is exactly $2\langle S_1^2\rangle$ for $\lambda = 2$, hence for large L,

$$A = L^2\left[2 + e^{-2}\right]. \tag{A.33}$$

Next,

$$E = \sum_{ijkl}\langle\epsilon_i\epsilon_j\epsilon_k\epsilon_l\rangle = \sum_{ijkl}\langle\epsilon_i\epsilon_j\rangle\langle\epsilon_k\epsilon_l\rangle + \langle\epsilon_i\epsilon_k\rangle\langle\epsilon_j\epsilon_l\rangle + \langle\epsilon_i\epsilon_l\rangle\langle\epsilon_j\epsilon_k\rangle \tag{A.34}$$

$$= 3\sum_{ijkl}\langle\epsilon_i\epsilon_j\rangle\langle\epsilon_k\epsilon_l\rangle \tag{A.35}$$

$$= 3\left(\sum_{ij}\langle\epsilon_i\epsilon_j\rangle\right)^2 = 3L^4\langle S_1^2\rangle^2. \tag{A.36}$$

Lastly,

$$C = \sum_{ijk}\langle\epsilon_i^2\epsilon_j\epsilon_k\rangle = \sum_{ijk}\langle\epsilon_i^2\rangle\langle\epsilon_j\epsilon_k\rangle + 2\langle\epsilon_i\epsilon_j\rangle\langle\epsilon_i\epsilon_k\rangle \tag{A.37}$$

$$= L^3\langle S_i^2\rangle + 2\underbrace{\sum_{ijk}\langle\epsilon_i\epsilon_j\rangle\langle\epsilon_i\epsilon_k\rangle}_{\mathcal{S}}. \tag{A.38}$$

To compute $\mathcal{S}$, consider the partial sum

$$p_i = \sum_j\langle\epsilon_i\epsilon_j\rangle = \sum_{j=1}^{L} a^{|i-j|} = \sum_{j=1}^{i} a^{i-j} + \sum_{j=i+1}^{L} a^{j-i} \tag{A.39}$$

$$= \frac{a^i + a^{L-i+1} - a - 1}{a-1}. \tag{A.40}$$

Now, $\mathcal{S} = \sum_i (p_i)^2$, which evaluates to

$$\begin{aligned}\mathcal{S}(a-1)^3(a+1) = &-2(L+2)a^{L+1} - 8a^{L+2} + 2(L-2)a^{L+3} + 2a^{2L+2} + a^4L \\ &+ 2a^3(L+2) + 6a^2 - 2a(L-2) - L,\end{aligned} \tag{A.41}$$

which gives, for large L,

$$\mathcal{S} = (10e^{-1} - e^{-2} - 3)L^3 + \mathcal{O}(L). \tag{A.42}$$

Overall,

$$\langle\mathcal{X}^2\rangle = W^4[2 + e^{-2}] + 4t^2W^2 - 2W^4\langle S_1^2\rangle - 4\frac{W^4}{L^3}S - 4t^2W^2\langle S_1^2\rangle + 4t^4 + 3W^4\langle S_1^2\rangle^2. \tag{A.43}$$

Having computed all of the terms of $\langle \mathcal{X}^2 \rangle$, we turn to $\langle \mathcal{X} \rangle^2$,

$$\langle \mathcal{X} \rangle^2 = \left[W^2(1 - \langle S_1^2 \rangle) + 2t^2 \right]^2 \tag{A.44}$$

$$= W^4(1 + \langle S_1^2 \rangle^2 - 2\langle S_1^2 \rangle) + 4t^2 W^2(1 - \langle S_1^2 \rangle) + 4t^4. \tag{A.45}$$

Hence

$$\langle \mathcal{X}^2 \rangle - \langle \mathcal{X} \rangle^2 = W^4[1 + e^{-2}] + 2W^4 \langle S_1^2 \rangle^2 - \frac{4W^4}{L^3}\mathcal{S} \tag{A.46}$$

$$= W^4[13 + 13e^{-2} - 40e^{-1}], \tag{A.47}$$

in the thermodynamic limit. Overall, therefore, $\mathrm{var(X)} \sim \mathcal{O}\left(W^4\right)$. In words, this result states that the variance of the eigenspectrum of the maximally-correlated model fluctuates from realisation-to-realisation, even in the thermodynamic limit. For further discussion, see Sec. 6.2.1.

References

[1] A. Duthie, S. Roy, and D. E. Logan, "Self-consistent theory of mobility edges in quasiperiodic chains", Phys. Rev. B **103**, L060201 (2021).

[2] A. Duthie, S. Roy, and D. E. Logan, "Localization in quasiperiodic chains: a theory based on convergence of local propagators", Phys. Rev. B **104**, 064201 (2021).

[3] A. Duthie, S. Roy, and D. E. Logan, "Anomalous multifractality in quantum chains with strongly correlated disorder", Phys. Rev. B **106**, L020201 (2022).

[4] P. W. Anderson, "Absence of diffusion in certain random lattices", Phys. Rev. **109**, 1492–1505 (1958).

[5] F. Evers and A. D. Mirlin, "Anderson transitions", Rev. Mod. Phys. **80**, 1355–1417 (2008).

[6] D. A. Abanin, E. Altman, I. Bloch, and M. Serbyn, "Colloquium: many-body localization, thermalization, and entanglement", Rev. Mod. Phys. **91**, 021001 (2019).

[7] R. Nandkishore and D. A. Huse, "Many-body localization and thermalization in quantum statistical mechanics", Annu. Rev. Condens. Matter Phys. **6**, 15 (2015).

[8] F. Alet and N. Laflorencie, "Many-body localization: an introduction and selected topics", Comptes Rendus Physique **19**, 498–525 (2018).

[9] R. Weaver, "Anderson localization of ultrasound", Wave Motion **12**, 129–142 (1990).

[10] H. Hu, A. Strybulevych, J. H. Page, S. E. Skipetrov, and B. A. van Tiggelen, "Localization of ultrasound in a three-dimensional elastic network", Nature Physics **4**, 945–948 (2008).

[11] M. Segev, Y. Silberberg, and D. N. Christodoulides, "Anderson localization of light", Nature Photonics **7**, 197–204 (2013).

[12] C. Dembowski, H.-D. Gräf, R. Hofferbert, H. Rehfeld, A. Richter, and T. Weiland, "Anderson localization in a string of microwave cavities", Phys. Rev. E **60**, 3942–3948 (1999).

[13] A. Lagendijk, B. v. Tiggelen, and D. S. Wiersma, "Fifty years of Anderson localization", Physics Today **62**, 24–29 (2009).

[14] R. E. Prange, D. R. Grempel, and S. Fishman, "Wave functions at a mobility edge: an example of a singular continuous spectrum", Phys. Rev. B **28**, 7370–7372 (1983).

[15] S. Das Sarma, S. He, and X. C. Xie, "Mobility edge in a model one-dimensional potential", Phys. Rev. Lett. **61**, 2144–2147 (1988).

[16] S. Das Sarma, S. He, and X. C. Xie, "Localization, mobility edges, and metal-insulator transition in a class of one-dimensional slowly varying deterministic potentials", Phys. Rev. B **41**, 5544–5565 (1990).

[17]D. J. Boers, B. Goedeke, D. Hinrichs, and M. Holthaus, "Mobility edges in bichromatic optical lattices", Phys. Rev. A **75**, 063404 (2007).

[18]J. Biddle, B. Wang, D. J. Priour, and S. Das Sarma, "Localization in one-dimensional incommensurate lattices beyond the Aubry-André model", Phys. Rev. A **80**, 021603 (2009).

[19]J. Biddle and S. Das Sarma, "Predicted mobility edges in one-dimensional incommensurate optical lattices: an exactly solvable model of Anderson localization", Phys. Rev. Lett. **104**, 070601 (2010).

[20]J. Biddle, D. J. Priour, B. Wang, and S. Das Sarma, "Localization in one-dimensional lattices with non-nearest-neighbor hopping: generalized Anderson and Aubry-André models", Phys. Rev. B **83**, 075105 (2011).

[21]S. Ganeshan, J. H. Pixley, and S. Das Sarma, "Nearest neighbor tight binding models with an exact mobility edge in one dimension", Phys. Rev. Lett. **114**, 146601 (2015).

[22]Y. Wang, X. Xia, L. Zhang, H. Yao, S. Chen, J. You, Q. Zhou, and X.-J. Liu, "One-dimensional quasiperiodic mosaic lattice with exact mobility edges", Phys. Rev. Lett. **125**, 196604 (2020).

[23]S. Gopalakrishnan, "Self-dual quasiperiodic systems with power-law hopping", Phys. Rev. B **96**, 054202 (2017).

[24]C. Monthus, "Multifractality in the generalized Aubry-André quasiperiodic localization model with power-law hoppings or power-law Fourier coefficients", Fractals **27**, 1950007 (2019).

[25]X. Li, X. Li, and S. Das Sarma, "Mobility edges in one-dimensional bichromatic incommensurate potentials", Phys. Rev. B **96**, 085119 (2017).

[26]M. Kohmoto, L. P. Kadanoff, and C. Tang, "Localization problem in one dimension: mapping and escape", Phys. Rev. Lett. **50**, 1870–1872 (1983).

[27]S. Ostlund, R. Pandit, D. Rand, H. J. Schellnhuber, and E. D. Siggia, "One-dimensional Schrödinger equation with an almost periodic potential", Phys. Rev. Lett. **50**, 1873–1876 (1983).

[28]S. Aubry and G. André, "Analyticity breaking and Anderson localization in incommensurate lattices", Ann. Israel Phys. Soc **3**, 18 (1980).

[29]S. Roy and D. E. Logan, "Fock-space correlations and the origins of many-body localization", Phys. Rev. B **101**, 134202 (2020).

[30]S. Roy and D. E. Logan, "Localization on certain graphs with strongly correlated disorder", Phys. Rev. Lett. **125**, 250402 (2020).

[31]E. Feenberg, "A note on perturbation theory", Phys. Rev. **74**, 206 (1948).

[32]K. M. Watson, "Multiple scattering by quantum-mechanical systems", Phys. Rev. **105**, 1388 (1957).

[33]E. N. Economou, *Green's functions in quantum physics* (Springer, Berlin, 2006).

[34]R. Abou-Chacra, P. W. Anderson, and D. J. Thouless, "A self-consistent theory of localization", Journal of Physics C: Solid State Physics **6**, 1734 (1973).

[35]P. A. Lee and T. V. Ramakrishnan, "Disordered electronic systems", Rev. Mod. Phys. **57**, 287–337 (1985).

[36]P. W. Anderson, "Local moments and localized states", Nobel Lecture (1977).

[37]N. F. Mott and W. D. Twose, "The theory of impurity conduction", Advances in Physics **10**, 107–163 (1961).

[38]H. Kunz and B. Souillard, "Sur le spectre des opérateurs aux différences finies aléatoires", Communications in Mathematical Physics **78**, 201–246 (1980).

[39]E. Abrahams, P. W. Anderson, D. C. Licciardello, and T. V. Ramakrishnan, "Scaling theory of localization: absence of quantum diffusion in two dimensions", Phys. Rev. Lett. **42**, 673–676 (1979).

[40]N. Mott, "Electrons in disordered structures", Advances in Physics **16**, 49–144 (1967).

[41]J. M. Ziman, "Localization of electrons in ordered and disordered systems II. bound bands", Journal of Physics C: Solid State Physics **2**, 1230–1247 (1969).

[42]D. J. Thouless, "Anderson's theory of localized states", **3**, 1559–1566 (1970).

[43]K. E. Khor and P. V. Smith, "Derivation of the band tailing in the Anderson model", Journal of Physics C: Solid State Physics **4**, 2041–2051 (1971).

[44]J. T. Edwards and D. J. Thouless, "Numerical studies of localization in disordered systems", Journal of Physics C: Solid State Physics **5**, 807–820 (1972).

[45]E. N. Economou and M. H. Cohen, "Existence of mobility edges in Anderson's model for random lattices", Phys. Rev. B **5**, 2931–2948 (1972).

[46]B Kramer and A MacKinnon, "Localization: theory and experiment", Reports on Progress in Physics **56**, 1469–1564 (1993).

[47]M. Schreiber and H. Grussbach, "Multifractal wave functions at the Anderson transition", Phys. Rev. Lett. **67**, 607–610 (1991).

[48]F. Milde, R. A. Römer, and M. Schreiber, "Multifractal analysis of the metal-insulator transition in anisotropic systems", Phys. Rev. B **55**, 9463–9469 (1997).

[49]A. D. Mirlin, Y. V. Fyodorov, A. Mildenberger, and F. Evers, "Exact relations between multifractal exponents at the Anderson transition", Phys. Rev. Lett. **97**, 046803 (2006).

[50]A. Rodriguez, L. J. Vasquez, and R. A. Römer, "Multifractal analysis with the probability density function at the three-dimensional Anderson transition", Phys. Rev. Lett. **102**, 106406 (2009).

[51]M. Janssen, "Multifractal analysis of broadly-distributed observables at criticality", International Journal of Modern Physics B **08**, 943–984 (1994).

[52]B. Huckestein, "Scaling theory of the integer quantum Hall effect", Rev. Mod. Phys. **67**, 357–396 (1995).

[53]S. Roy, I. M. Khaymovich, A. Das, and R. Moessner, "Multifractality without fine-tuning in a Floquet quasiperiodic chain", SciPost Phys. **4**, 25 (2018).

[54]C. Monthus, "Multifractality of eigenstates in the delocalized non-ergodic phase of some random matrix models: Wigner–Weisskopf approach", **50**, 295101 (2017).

[55]P. G. Harper, "Single band motion of conduction electrons in a uniform magnetic field", Proceedings of the Physical Society. Section A **68**, 874–878 (1955).

[56]K. Drese and M. Holthaus, "Exploring a metal-insulator transition with ultracold atoms in standing light waves?", Phys. Rev. Lett. **78**, 2932–2935 (1997).

[57]H. P. Lüschen, S. Scherg, T. Kohlert, M. Schreiber, P. Bordia, X. Li, S. Das Sarma, and I. Bloch, "Single-particle mobility edge in a one-dimensional quasiperiodic optical lattice", Phys. Rev. Lett. **120**, 160404 (2018).

[58]T. Kohlert, S. Scherg, X. Li, H. P. Lüschen, S. Das Sarma, I. Bloch, and M. Aidelsburger, "Observation of many-body localization in a one-dimensional system with a single-particle mobility edge", Phys. Rev. Lett. **122**, 170403 (2019).

[59]F. A. An, K. Padavić, E. J. Meier, S. Hegde, S. Ganeshan, J. Pixley, S. Vishveshwara, and B. Gadway, "Interactions and mobility edges: observing the generalized Aubry-André model", Physical Review Letters **126**, 040603 (2021).

[60]L. Sanchez-Palencia and M. Lewenstein, "Disordered quantum gases under control", Nature Physics **6**, 87–95 (2010).

[61]Y. Lahini, A. Avidan, F. Pozzi, M. Sorel, R. Morandotti, D. N. Christodoulides, and Y. Silberberg, "Anderson localization and nonlinearity in one-dimensional disordered photonic lattices", Phys. Rev. Lett. **100**, 013906 (2008).

[62]D. H. White, T. A. Haase, D. J. Brown, M. D. Hoogerland, M. S. Najafabadi, J. L. Helm, C. Gies, D. Schumayer, and D. A. W. Hutchinson, "Observation of two-dimensional Anderson localisation of ultracold atoms", Nature Communications **11**, 4942 (2020).

[63]G. Roati, C. D'Errico, L. Fallani, M. Fattori, C. Fort, M. Zaccanti, G. Modugno, M. Modugno, and M. Inguscio, "Anderson localization of a non-interacting Bose–Einstein condensate", Nature **453**, 895–898 (2008).

[64]L. Fallani, J. E. Lye, V. Guarrera, C. Fort, and M. Inguscio, "Ultracold atoms in a disordered crystal of light: towards a Bose glass", Phys. Rev. Lett. **98**, 130404 (2007).

[65]S. Iyer, V. Oganesyan, G. Refael, and D. A. Huse, "Many-body localization in a quasiperiodic system", Phys. Rev. B **87**, 134202 (2013).

[66]"Detecting a many-body mobility edge with quantum quenches", SciPost Phys. **1**, 010 (2016).

[67]E. Altman, "Many-body localization and quantum thermalization", Nature Physics **14**, 979–983 (2018).

[68]T. Xiao, D. Xie, Z. Dong, T. Chen, W. Yi, and B. Yan, "Observation of topological phase with critical localization in a quasi-periodic lattice", Science Bulletin **66**, 2175–2180 (2021).

[69]D. E. Logan and P. G. Wolynes, "Quantum localization and energy flow in many-dimensional Fermi resonant systems", The Journal of Chemical Physics **93**, 4994–5012 (1990).

[70]B. L. Altshuler, Y. Gefen, A. Kamenev, and L. S. Levitov, "Quasiparticle lifetime in a finite system: a nonperturbative approach", Phys. Rev. Lett. **78**, 2803–2806 (1997).

[71]C. Monthus and T. Garel, "Many-body localization transition in a lattice model of interacting Fermions: statistics of renormalized hoppings in configuration space", Phys. Rev. B **81**, 134202 (2010).

[72]D. E. Logan and S. Welsh, "Many-body localization in Fock space: a local perspective", Phys. Rev. B **99**, 045131 (2019).

[73]S. Roy and D. E. Logan, "Self-consistent theory of many-body localisation in a quantum spin chain with long-range interactions", SciPost Phys. **7**, 42 (2019).

[74]F. Pietracaprina, V. Ros, and A. Scardicchio, "Forward approximation as a mean-field approximation for the Anderson and many-body localization transitions", Phys. Rev. B **93**, 054201 (2016).

[75]N. Macé, F. Alet, and N. Laflorencie, "Multifractal scalings across the many-body localization transition", Phys. Rev. Lett. **123**, 180601 (2019).

[76]F. Pietracaprina and N. Laflorencie, "Hilbert-space fragmentation, multifractality, and many-body localization", Annals of Physics **435**, Special Issue on Localisation 2020, 168502 (2021).

[77]S. Roy, D. E. Logan, and J. T. Chalker, "Exact solution of a percolation analog for the many-body localization transition", Phys. Rev. B **99**, 220201 (2019).

[78]S. Roy, J. T. Chalker, and D. E. Logan, "Percolation in Fock space as a proxy for many-body localization", Phys. Rev. B **99**, 104206 (2019).

[79]S. Ghosh, A. Acharya, S. Sahu, and S. Mukerjee, "Many-body localization due to correlated disorder in Fock space", Phys. Rev. B **99**, 165131 (2019).

[80]S. Balasubramanian, Y. Liao, and V. Galitski, "Many-body localization landscape", Phys. Rev. B **101**, 014201 (2020).

[81]G. De Tomasi, D. Hetterich, P. Sala, and F. Pollmann, "Dynamics of strongly interacting systems: from Fock-space fragmentation to many-body localization", Phys. Rev. B **100**, 214313 (2019).

[82]N. F. Mott, "Conduction in non-crystalline materials", The Philosophical Magazine: A Journal of Theoretical Experimental and Applied Physics **19**, 835–852 (1969).

[83]N. Apsley and H. P. Hughes, "Temperature-and field-dependence of hopping conduction in disordered systems", The Philosophical Magazine: A Journal of Theoretical Experimental and Applied Physics **30**, 963–972 (1974).

[84]R. M. Hill, "Variable-range hopping", physica status solidi (a) **34**, 601–613 (1976).

[85]W. N. Shafarman and T. G. Castner, "Critical behavior of Mott variable-range hopping in Si:As near the metal-insulator transition", Phys. Rev. B **33**, 3570–3572 (1986).

[86]R. Rosenbaum, "Crossover from Mott to Efros-Shklovskii variable-range-hopping conductivity in In_xO_y films", Phys. Rev. B **44**, 3599–3603 (1991).

[87]L. Fleishman and P. W. Anderson, "Interactions and the Anderson transition", Phys. Rev. B **21**, 2366–2377 (1980).

[88]B. Altshuler and A. Aronov, "Chapter 1 - electron–electron interaction in disordered conductors", in *Electron–electron interactions in disordered systems*, Vol. 10, edited by A. Efros and M. Pollak, Modern Problems in Condensed Matter Sciences (Elsevier, 1985), pp. 1–153.

[89]A. Finkelshtein, "Effect of Coulomb interaction on the properties of disordered metals", Zhurnal Eksperimentalnoi I Tereticheskoi Fiziki **84**, 168–189 (1983).

[90]T. Giamarchi and H. J. Schulz, "Anderson localization and interactions in one-dimensional metals", Phys. Rev. B **37**, 325–340 (1988).

[91]D. Abanin, J. Bardarson, G. De Tomasi, S. Gopalakrishnan, V. Khemani, S. Parameswaran, F. Pollmann, A. Potter, M. Serbyn, and R. Vasseur, "Distinguishing localization from chaos: challenges in finite-size systems", Annals of Physics **427**, 168415 (2021).

[92]E. Altman and R. Vosk, "Universal dynamics and renormalization in many-body-localized systems", Annu. Rev. Condens. Matter Phys. **6**, 383 (2015).

[93]J. M. Deutsch, "Eigenstate thermalization hypothesis", Rep. Prog. Phys. **81**, 082001 (2018).

[94]L. Foini and J. Kurchan, "Eigenstate thermalization hypothesis and out of time order correlators", Phys. Rev. E **99**, 042139 (2019).

[95]J. Z. Imbrie, V. Ros, and A. Scardicchio, "Local integrals of motion in many-body localized systems", Annalen der Physik **529**, 1600278.

[96]A. Chandran, I. H. Kim, G. Vidal, and D. A. Abanin, "Constructing local integrals of motion in the many-body localized phase", Phys. Rev. B **91**, 085425 (2015).

[97]V. Ros, M. Müller, and A. Scardicchio, "Integrals of motion in the many-body localized phase", Nuclear Physics B **891**, 420–465 (2015).

[98]L. Rademaker and M. Ortuño, "Explicit local integrals of motion for the many-body localized state", Phys. Rev. Lett. **116**, 010404 (2016).

[99]S. D. Geraedts, R. N. Bhatt, and R. Nandkishore, "Emergent local integrals of motion without a complete set of localized eigenstates", Phys. Rev. B **95**, 064204 (2017).

[100]M. Mierzejewski, M. Kozarzewski, and P. Prelovšek, "Counting local integrals of motion in disordered spinless-Fermion and Hubbard chains", Phys. Rev. B **97**, 064204 (2018).

[101]M. Mierzejewski and L. Vidmar, "Quantitative impact of integrals of motion on the eigenstate thermalization hypothesis", Phys. Rev. Lett. **124**, 040603 (2020).

[102]H. Singh, B. Ware, R. Vasseur, and S. Gopalakrishnan, "Local integrals of motion and the quasiperiodic many-body localization transition", Phys. Rev. B **103**, L220201 (2021).

[103]J. Z. Imbrie, "On many-body localization for quantum spin chains", J. Stat. Phys. **163**, 998 (2016).

[104]S. Welsh and D. E. Logan, "Simple probability distributions on a Fock-space lattice", J. Phys.: Condens. Matter **30**, 405601 (2018).

[105]A. De Luca and A. Scardicchio, "Ergodicity breaking in a model showing many-body localization", Europhys. Lett. **101**, 37003 (2013).

[106]M. Serbyn, Z. Papić, and D. A. Abanin, "Criterion for many-body localization-delocalization phase transition", Phys. Rev. X **5**, 041047 (2015).

[107]C. L. Baldwin, C. R. Laumann, A. Pal, and A. Scardicchio, "The many-body localized phase of the quantum random energy model", Phys. Rev. B **93**, 024202 (2016).

[108]S. Nag and A. Garg, "Many-body localization in the presence of long-range interactions and long-range hopping", Phys. Rev. B **99**, 224203 (2019).

[109]G. Biroli and M. Tarzia, "Anomalous dynamics on the ergodic side of the many-body localization transition and the glassy phase of directed polymers in random media", Phys. Rev. B **102**, 064211 (2020).

[110]M. Tarzia, "Many-body localization transition in Hilbert space", Phys. Rev. B **102**, 014208 (2020).

[111]G. De Tomasi, I. M. Khaymovich, F. Pollmann, and S. Warzel, "Rare thermal bubbles at the many-body localization transition from the Fock space point of view", Phys. Rev. B **104**, 024202 (2021).

[112]M. Hopjan and F. Heidrich-Meisner, "Many-body localization from a one-particle perspective in the disordered one-dimensional Bose-Hubbard model", Phys. Rev. A **101**, 063617 (2020).

[113]K. S. Tikhonov and A. D. Mirlin, "Eigenstate correlations around the many-body localization transition", Phys. Rev. B **103**, 064204 (2021).

[114]M. Stephens and J. Skinner, "Anderson localization with short-range correlated diagonal disorder", Journal of Luminescence **60-61**, 449–450 (1994).

[115]F. A. B. F. de Moura and M. L. Lyra, "Delocalization in the 1d Anderson model with long-range correlated disorder", Phys. Rev. Lett. **81**, 3735–3738 (1998).

[116]F. M. Izrailev and A. A. Krokhin, "Localization and the mobility edge in one-dimensional potentials with correlated disorder", Phys. Rev. Lett. **82**, 4062–4065 (1999).

[117]H. Shima, T. Nomura, and T. Nakayama, "Localization-delocalization transition in one-dimensional electron systems with long-range correlated disorder", Phys. Rev. B **70**, 075116 (2004).

[118]T. Kaya, "Localization-delocalization transition in chains with long-range correlated disorder", The European Physical Journal B **55**, 49–56 (2007).

[119]J. L. Pichard and G Sarma, "Finite size scaling approach to Anderson localisation", Journal of Physics C: Solid State Physics **14**, L127–L132 (1981).

[120]M. A. Lemieux, P. Breton, and A.-M. S. Tremblay, "Unified approach to numerical transfer matrix methods for disordered systems : applications to mixed crystals and to elasticity percolation", Journal de Physique Lettres **46**, 1–7 (1985).

[121]K. A. Muttalib, J. L. Pichard, and A. D. Stone, "Random-matrix theory and universal statistics for disordered quantum conductors", Phys. Rev. Lett. **59**, 2475–2478 (1987).

[122]J. Pendry, "Symmetry and transport of waves in one-dimensional disordered systems", Advances in Physics **43**, 461–542 (1994).

[123]P. Mello, P Pereyra, and N Kumar, "Macroscopic approach to multichannel disordered conductors", Annals of Physics **181**, 290–317 (1988).

[124]G. De Tomasi, S. Roy, and S. Bera, "Generalized dyson model: nature of the zero mode and its implication in dynamics", Phys. Rev. B **94**, 144202 (2016).

[125]I. M. Khaymovich and V. E. Kravtsov, "Dynamical phases in a "multifractal" Rosenzweig-Porter model", SciPost Phys. **11**, 45 (2021).

[126]D. Williams, *Probability with martingales* (Cambridge University Press, 1991).

[127]D. J. Thouless, "Electrons in disordered systems and the theory of localization", Physics Reports **13**, 93–142 (1974).

[128]D. C. Licciardello and E. N. Economou, "Study of localization in Anderson's model for random lattices", Phys. Rev. B **11**, 3697–3717 (1975).

[129]D. E. Logan and P. G. Wolynes, "Anderson localization in topologically disordered systems", Phys. Rev. B **31**, 2437–2450 (1985).

[130]D. E. Logan and P. G. Wolynes, "Dephasing and Anderson localization in topologically disordered systems", Phys. Rev. B **36**, 4135–4147 (1987).

[131]C. M. Soukoulis and E. N. Economou, "Localization in one-dimensional lattices in the presence of incommensurate potentials", Phys. Rev. Lett. **48**, 1043–1046 (1982).

[132]S. Roy and D. E. Logan, "Fock-space anatomy of eigenstates across the many-body localization transition", Phys. Rev. B **104**, 174201 (2021).

[133]D. E. Logan, "Quantum mechanics in condensed matter", Theory and Modelling in Chemical Sciences, Oxford University (2018).

[134]A. L. Fetter and J. D. Walecka, *Quantum theory of many-particle systems* (Dover Publications, 2003).

[135]A. Weiße and H. Fehske, "Exact diagonalization techniques", in *Computational many-particle physics*, edited by H. Fehske, R. Schneider, and A. Weiße (Springer Berlin Heidelberg, Berlin, Heidelberg, 2008), pp. 529–544.

[136]A. Scardicchio and T. Thiery, *Perturbation theory approaches to Anderson and many-body localization: some lecture notes*, 2017.

[137]H. A. Bethe and W. L. Bragg, "Statistical theory of superlattices", Proceedings of the Royal Society of London. Series A - Mathematical and Physical Sciences **150**, 552–575 (1935).

[138]A. D. Mirlin and Y. V. Fyodorov, "Localization transition in the Anderson model on the Bethe lattice: spontaneous symmetry breaking and correlation functions", Nuclear Physics B **366**, 507–532 (1991).

[139]A. Klein, "Extended states in the Anderson model on the Bethe lattice", Advances in Mathematics **133**, 163–184 (1998).

[140]A. De Luca, B. L. Altshuler, V. E. Kravtsov, and A. Scardicchio, "Anderson localization on the Bethe lattice: nonergodicity of extended states", Phys. Rev. Lett. **113**, 046806 (2014).

[141]G. Parisi, S. Pascazio, F. Pietracaprina, V. Ros, and A. Scardicchio, "Anderson transition on the Bethe lattice: an approach with real energies", Journal of Physics A: Mathematical and Theoretical **53**, 014003 (2019).

[142]B. Altshuler and V. Prigodin, "Distribution of local density of states and NMR line shape in a one-dimensional disordered conductor", Sov. Phys. JETP **68**, 198 (1989).

[143]J Bellissard and B Simon, "Cantor spectrum for the almost Mathieu equation", Journal of Functional Analysis **48**, 408–419 (1982).

[144]J. Bellissard, R. Lima, and D. Testard, "A metal-insulator transition for the almost Mathieu model", Communications in Mathematical Physics **88**, 207–234 (1983).

[145]F. Delyon, "Absence of localisation in the almost Mathieu equation", Journal of Physics A **20** (1987).

[146]V. Chulaevsky and F. Delyon, "Purely absolutely continuous spectrum for almost Mathieu operators", Journal of Statistical Physics **55**, 1279–1284 (1989).

[147]J. Avron, P. H. M. v. Mouche, and B. Simon, "On the measure of the spectrum for the almost Mathieu operator", Communications in Mathematical Physics **132**, 103–118 (1990).

[148]Y. Last, "Zero measure spectrum for the almost Mathieu operator", Communications in Mathematical Physics **164**, 421–432 (1994).

[149]S. Y. Jitomirskaya, "Metal-insulator transition for the almost mathieu operator", Annals of Mathematics **150**, 1159–1175 (1999).

[150]Y. Last, "A relation between a.c. spectrum of ergodic Jacobi matrices and the spectra of periodic approximants", Communications in Mathematical Physics **151**, 183–192 (1993).

[151]D. R. Hofstadter, "Energy levels and wave functions of bloch electrons in rational and irrational magnetic fields", Phys. Rev. B **14**, 2239–2249 (1976).

[152]J. Sokoloff, "Unusual band structure, wave functions and electrical conductance in crystals with incommensurate periodic potentials", Physics Reports **126**, 189–244 (1985).

[153]D. J. Thouless, "Bandwidths for a quasiperiodic tight-binding model", Phys. Rev. B **28**, 4272–4276 (1983).

[154]M. L. Sun, G. Wang, N. B. Li, and T. Nakayama, "Localization-delocalization transition in self-dual quasi-periodic lattices", EPL (Europhysics Letters) **110**, 57003 (2015).

[155]Y. Wang, X. Xia, Y. Wang, Z. Zheng, and X.-J. Liu, "Duality between two generalized Aubry-André models with exact mobility edges", Phys. Rev. B **103**, 174205 (2021).

[156]E. Sorets and T. Spencer, "Positive Lyapunov exponents for Schrödinger operators with quasi-periodic potentials", Communications in Mathematical Physics **142**, 543–566 (1991).

[157]J. D. Bodyfelt, D. Leykam, C. Danieli, X. Yu, and S. Flach, "Flatbands under correlated perturbations", Phys. Rev. Lett. **113**, 236403 (2014).

[158]C. Danieli, J. D. Bodyfelt, and S. Flach, "Flat-band engineering of mobility edges", Phys. Rev. B **91**, 235134 (2015).

[159]M. Rossignolo and L. Dell'Anna, "Localization transitions and mobility edges in coupled Aubry-André chains", Phys. Rev. B **99**, 054211 (2019).

[160]S. Kullback and R. A. Leibler, "On information and sufficiency", The Annals of Mathematical Statistics **22**, 79–86 (1951).

[161]J. D. Miller and B. Derridda, "Weak-disorder expansion for the Anderson model on a tree", Journal of Statistical Physics **75**, 357–388 (1994).

[162]C. Monthus and T. Garel, "Anderson transition on the Cayley tree as a traveling wave critical point for various probability distributions", Journal of Physics A: Mathematical and Theoretical **42**, 075002 (2009).

[163]I. García-Mata, O. Giraud, B. Georgeot, J. Martin, R. Dubertrand, and G. Lemarié, "Scaling theory of the Anderson transition in random graphs: ergodicity and universality", Phys. Rev. Lett. **118**, 166801 (2017).

[164]V. Kravtsov, I. Khaymovich, E Cuevas, and M Amini, "A random matrix model with localization and ergodic transitions", New Journal of Physics **17**, 122002 (2015).

[165]G. De Tomasi, S. Bera, A. Scardicchio, and I. M. Khaymovich, "Subdiffusion in the Anderson model on the random regular graph", Phys. Rev. B **101**, 100201 (2020).

[166]F. Wegner, "Inverse participation ratio in 2+ϵ dimensions", Zeitschrift für Physik B Condensed Matter **36**, 209–214 (1980).

[167]J. Bauer, T.-M. Chang, and J. L. Skinner, "Correlation length and inverse-participation-ratio exponents and multifractal structure for Anderson localization", Phys. Rev. B **42**, 8121–8124 (1990).

[168]J. T. Chalker, V. E. Kravtsov, and I. V. Lerner, "Spectral rigidity and eigenfunction correlations at the Anderson transition", JETP Letters **64**, 386–392 (1996).

[169]A. D. Mirlin and F. Evers, "Multifractality and critical fluctuations at the Anderson transition", Phys. Rev. B **62**, 7920–7933 (2000).

[170]F. Evers and A. D. Mirlin, "Fluctuations of the inverse participation ratio at the Anderson transition", Phys. Rev. Lett. **84**, 3690–3693 (2000).

[171]E. Cuevas, M. Ortuño, V. Gasparian, and A. Pérez-Garrido, "Fluctuations of the correlation dimension at metal-insulator transitions", Phys. Rev. Lett. **88**, 016401 (2001).

[172]J. Chalker, "Scaling and correlations at a mobility edge in two dimensions", Journal of Physics C: Solid State Physics **21**, L119 (1988).

[173]J. T. Chalker, "Scaling and eigenfunction correlations near a mobility edge", Physica A: Statistical Mechanics and its Applications **167**, 253–258 (1990).

[174]J. T. Chalker and P. D. Coddington, "Percolation, quantum tunnelling and the integer Hall effect", Journal of Physics C: Solid State Physics **21**, 2665 (1988).

[175]F. Evers, A. Mildenberger, and A. D. Mirlin, "Multifractality of wave functions at the quantum Hall transition revisited", Phys. Rev. B **64**, 241303 (2001).

[176]C. Monthus and T. Garel, "The Anderson localization transition with long-ranged hoppings: analysis of the strong multifractality regime in terms of weighted Lévy sums", Journal of Statistical Mechanics: Theory and Experiment **2010**, P09015 (2010).

[177]B. L. Altshuler, E. Cuevas, L. B. Ioffe, and V. E. Kravtsov, "Nonergodic phases in strongly disordered random regular graphs", Phys. Rev. Lett. **117**, 156601 (2016).

[178]B. Altshuler, L. Ioffe, and V. Kravtsov, "Multifractal states in self-consistent theory of localization: analytical solution", arXiv:1610.00758 (2016).

[179]R. Ketzmerick, K. Kruse, S. Kraut, and T. Geisel, "What determines the spreading of a wave packet?", Phys. Rev. Lett. **79**, 1959–1963 (1997).

[180]T. Ohtsuki and T. Kawarabayashi, "Anomalous diffusion at the Anderson transitions", Journal of the Physical Society of Japan **66**, 314–317 (1997).

[181]P. K. Thakur, C Basu, A Mookerjee, and A. K. Sen, "A multifractal analysis for electronic transmittance in inhomogeneous potentials", Journal of Physics: Condensed Matter **4**, 6095–6107 (1992).

[182]F. M. Izrailev and A. A. Krokhin, "Localization and the mobility edge in one-dimensional potentials with correlated disorder", Phys. Rev. Lett. **82**, 4062–4065 (1999).

[183]A. Croy, P. Cain, and M. Schreiber, "Anderson localization in 1D systems with correlated disorder", The European Physical Journal B **82**, 107 (2011).

[184]G. C. Wick, "The evaluation of the collision matrix", Phys. Rev. **80**, 268–272 (1950).